Serum Potassium Concentration Monitoring by ECG Time Warping Analysis on the T wave

By

Flavio Palmieri

Thesis submitted in fulfillment of the requirements
for the degree of Doctor by the Universitat Politècnica de Catalunya
in the Biomedical Engineering programme

Directors:

Dr. Pablo Laguna Lasaosa[1,2]

Dr. Pedro Gomis Roman[3,2]

[1] Biomedical Signal Interpretation and Computational Simulation (BSICoS), Aragón Institute for Engineering Research (I3A), IIS Aragón, University of Zaragoza, Zaragoza, Spain.

[2] CIBER en Bioingeniería, Biomateriales y Nanomedicina (CIBER-BBN), Spain.

[3] Centre de Recerca en Enginyeria Biomèdica, Universitat Politècnica de Catalunya, Barcelona, Spain.

Barcelona, May 2022

Serum Potassium Concentration Monitoring by ECG Time Warping Analysis on the T wave

This doctoral thesis was developed within the joint Ph.D. program in biomedical engineering at Universitat Politècnica de Catalunya (Barcelona, Spain) and University of Zaragoza (Zaragoza, Spain) in the framework of *Doctorats Industrials* program co-financed by Laboratorios Rubió S.A. (Castellbisbal, Spain) and Agència de Gestió d'Ajuts Universitaris i de Recerca, Generalitat de Catalunya (Spain).
This thesis was also supported by Centro de Investigación Biomédica en Red de Bioingeniería, Biomateriales y Nanomedicina, CIBER-BBN ref: "**DE**tection of [$\mathbf{K}^+$] c**O**ncentration **AL**terations from the **E**CG (DEKOALE)" through Instituto de Salud Carlos III, and by both projects PID2019-104881RB-I00 and PID2019-105674RB-I00 funded by Spanish Ministry of Science and Innovation (MICINN) and FEDER, by *Gobierno de Aragón* (Spain) Reference Group BSICoS (T39-20R and project LMP94-21) co-funded by FEDER 2014-2020 "*Building Europe from Aragón*" and by European Research Council (ERC) through project ERC-StG 638284.

This thesis was performed in partnership with the Nephrology ward from Hospital Clínico Universitario Lozano Blesa (Zaragoza, Spain) and in collaboration with Dr J. Ramírez from the William Harvey Research Institute, Queen Mary University of London (London, UK).

Computations and simulations of this thesis were performed using the ICTS "NANBIOSIS", by means of the High Performance Computing Unit of the CIBER-BBN at Aragón Institute for Engineering Research (I3A) (Spain).

Date of current version: Monday 11th April, 2022

Abstract

End-stage renal disease (ESRD) patients demonstrate high rates of cardiovascular mortality and morbidity; and increased incidence of sudden cardiac death (SCD) with declining kidney functioning as a consequence of blood potassium ($[K^+]$) homeostasis impairment, which is restored by hemodialysis (HD) therapy. The clinically established method for the diagnosis of electrolyte concentration imbalance is blood tests, an invasive and costly procedure that limits continuous monitoring of ESRD patients. A non-invasive ambulatory index able to quantify changes in $[K^+]$ levels would be an important advance for both in-hospital and out-hospital continuous monitoring.
The electrocardiogram (ECG) could meet this need being a well-established non-invasive diagnostic tool that reflects the electrical activity of the heart. In particular, the T wave (TW) reflects the spatio-temporal repolarization of the ventricle, and its analysis has been used to measure the vulnerability of a patient to ventricular arrhythmias. This fact is of particular interest because TWs are frequently altered in ESRD patients undergoing HD.
Therefore, the aim of this dissertation is to investigate and to propose ECG-derived markers able to monitor changes in $[K^+]$ levels in ESRD patients undergoing HD. For that purpose, the clinical information stored in the morphology of the TWs are assessed by the *time warping analysis*, a technique that allows for the comparison and quantification of two different TW shapes in both amplitude and time domains.

In chapter 1, the physiological framework describing the functioning of the kidneys and the heart, as well as the characteristics of the biosignals analyzed throughout the thesis, is provided. Also, the pathophysiology of ESRD, with its diagnosis and treatment strategies are discussed. Then, an extensive review of previously proposed ECG-based markers, which were found to be correlated with $[K^+]$, is presented. The chapter concludes with an overview of the relationship between ESRD and heart activity and how it affects the ECG waveforms.

The description of the TW time warping analysis and the application of TW time warping derived markers in monitoring $[K^+]$ by analysing twenty-nine 48h ECG-Holter records from ESRD patients undergoing HD is presented in chapter 2. In addition, the derivation of a heart-rate (HR) corrected marker is also presented and investigate. Finally, the ability in tracking $[K^+]$ variations ($\Delta[K^+]$) of the proposed markers are compared with respect to two already proposed and well-established TW-based indexes related with $\Delta[K^+]$: the width of the TW (T_w) and the TW slope-to-amplitude ratio ($T_{S/A}$). All the markers are evaluated in a single lead approach as well as after having applied Principal Component Analysis (PCA), a lead space reduction (LSR) technique that emphasises the TW energy content on the independent leads, over the first transformed lead. Results demonstrate that PCA-based time warping markers have a higher correlation with $\Delta[K^+]$ than the single lead approach and both T_w and $T_{S/A}$, suggesting that they could be potentially useful for non-invasive monitoring of ESRD patients undergoing HD in hospital and in an ambulatory setting.

Although the promising results reported in chapter 2, PCA approach may not be the best strategy for emphasizing clinically relevant information related to $\Delta[K^+]$. Indeed, the maximum-variance criterion of PCA may be problematic when there is a low signal-to-noise ratio (SNR) or in the presence of body position changes (BPC). Therefore the possibility to use Periodic Component Analysis (πCA), a LSR technique maximising the beat-to-beat TW periodicity content on the independent leads, rather than PCA is explored in chapter 3. The aim is to compare the performance of the two LSR techniques in generating a transformed ECG lead from which TW time warping morphology markers can be reliably derived to non-invasively monitor $\Delta[K^+]$. Results reveal that the performance of πCA-based markers in following $\Delta[K^+]$ during HD was superior to that from PCA-based markers. Moreover, πCA-based markers showed improved robustness against BPC and noise. According to these findings, πCA outperform PCA in terms

of monitoring in ESRD patients as well as of robustness against BPC and low SNR, showing the highest stability for continuous post-HD monitoring.

Chapter 4 focuses on the application of linear, quadratic, and cubic fitting models to quantify $\Delta[K^+]$ from the πCA-based time warping markers. The accuracy of the regression models is evaluated by correlation and estimation error between the actual and the corresponding model-estimated $\Delta[K^+]$ values. Results support the use of polynomial models, in particular quadratic ones, as $\Delta[K^+]$ sensors in ESRD patients, having the smallest estimation error with respect to the linear one.

Time warping analysis is sensitive to TW boundary delineation errors, which may occur in case of automatic location of TW onset and end points in ECG signals. When that happens, the prognostic power of the proposed markers can be drastically reduced despite their strong correlation with $\Delta[K^+]$. Therefore, in chapter 5 a weighting stage is proposed in the computation of time warping markers. In particular, two weighting functions (WF)s are tested and their corresponding results are compared with respect to the control case, when no weighting is applied, in order to evaluate their performance in simulated scenarios and in real cases (i.e. for $[K^+]$ monitoring and SCD risk stratification). On the one hand, no improvements in $[K^+]$ monitoring are found probably due to the considerable potassium-induced TW morphological changes that may have masked any possible side effect of TW boundary delineation errors. On the other hand, both simulation tests and SCD risk stratification analysis show that the proposed WFs can enhance the TW time warping analysis robustness against TW delineation errors. Then, the employment of a weighting stage can improve the clinical reliability of time warping derived indexes in SCD risk stratification.

In conclusion, ECG-derived markers based on the TW time warping analysis have been investigated in this thesis in an attempt to develop a new method for $\Delta[K^+]$ estimation in ESRD patients undergoing HD therapy. Unlike the previously proposed markers, these exploit the overall TW morphology and their capacity for $\Delta[K^+]$ tracking and quantification through polynomial regression models has been proved. Finally, a weighting stage to minimise the undesired effects of TW delineation errors on the computation of time warping markers has been tested, resulting in noticeable improvement of the SCD risk stratification power of the TW time warping based markers.

Keywords: End Stage Renal Disease; Noninvasive Potassium Monitoring; Personalised Medicine; Electrocardiogram; T wave Processing; Time Warping Analysis; Principal Component Analysis; Periodic component analysis; Sudden Cardiac Death; Risk Prediction.

Resumen y conclusiones

Los pacientes con enfermedad renal en etapa terminal (ESRD) muestran altas tasas de mortalidad cardiovascular; y aumento de la incidencia de muerte cardíaca súbita (SCD) con deterioro del funcionamiento renal como consecuencia del deterioro de la homeostasis del potasio en sangre ($[K^+]$), que se restablece mediante la terapia de hemodiálisis (HD). El método clínicamente establecido para el diagnóstico del desequilibrio de concentración de electrolitos son los análisis de sangre, un procedimiento invasivo y costoso que limita la monitorización continua de los pacientes con ESRD. Un índice ambulatorio no invasivo capaz de cuantificar los cambios en los niveles de $[K^+]$ sería un avance importante para la monitorización continua tanto intrahospitalaria como extrahospitalaria.
El electrocardiograma (ECG) podría satisfacer esta necesidad al ser una herramienta de diagnóstico no invasiva bien establecida que refleja la actividad eléctrica del corazón. En particular, la onda T (TW) refleja la repolarización espacio-temporal del ventrículo, y su análisis se ha utilizado para medir la vulnerabilidad de un paciente a las arritmias ventriculares. Este hecho es de particular interés porque los TW se alteran con frecuencia en pacientes con ESRD sometidos a HD.
Por tanto, el objetivo de esta tesis es investigar y proponer marcadores derivados del ECG capaces de monitorizar los cambios en los niveles de $[K^+]$ en pacientes con ESRD sometidos a HD. Para ello, la información clínica almacenada en la morfología de los TW se evalúa mediante el *análisis de time warping*, una técnica que permite la comparación y la cuantificación de las diferencias entre dos formas de TW en los dominios de amplitud y tiempo.

En el capítulo 1, se proporciona el marco fisiológico que describe el funcionamiento de los riñones y el corazón, así como las características de las señales analizadas a lo largo de la tesis. Además, se discute la fisiopatología de la ESRD, con su diagnóstico y estrategias de tratamiento. A continuación, se presenta una revisión exhaustiva de los marcadores basados en ECG propuestos previamente, que se encontraron correlacionados con $[K^+]$. El capítulo concluye con una descripción general de la relación entre la ESRD y la actividad cardíaca y cómo afecta la forma de onda del ECG.

En el capítulo 2 se presenta la metodología del time warping y su aplicación para derivar marcadores para la monitorización de $[K^+]$ mediante el análisis de veintinueve Holter de 48 h de pacientes con ESRD sometidos a HD. Además, se presenta e investiga la derivación de un marcador corregido por la frecuencia cardiaca (HR). Finalmente, la capacidad de rastrear los cambios $[K^+]$ ($\Delta[K^+]$) de los marcadores propuestos se compara con dos ya propuestos y bien establecidos índices basados en la TW y relacionados con $\Delta[K^+]$: el ancho de la TW (en inglés TW width, T_w) y la relación pendiente-amplitud de la TW (TW slope-to-amplitude ratio, $T_{S/A}$). Todos los marcadores se evalúan en las derivaciones independintes, así como después de haber aplicado el análisis de componentes principales (PCA), una técnica de reducción del espacio de derivaciones (LSR) que enfatiza el contenido de energía de TW en las derivaciones independientes, sobre la primera derivación transformada. Los resultados demuestran que los marcadores time warping obtenido por PCA tienen una correlación más alta con $\Delta[K^+]$ resepcto a los mismos calculados en las derivaciones independientes así como respecto a T_w y $T_{S/A}$. Esto sugiere que los marcadores time warping obtenido con PCA podrían ser útil para la monitorización no invasiva de pacientes con ESRD sometidos a HD en el hospital y en un entorno de atención ambulatoria.

Aunque los resultados presentados en el capítulo 2 son prometedores, el uso de PCA puede no ser la mejor estrategia para enfatizar la información clínicamente relevante relacionada con $\Delta[K^+]$. De hecho, el criterio de varianza máxima en que se basa la PCA podría ser problemático cuando hay una baja relación señal/ruido (SNR) o en presencia de cambios de posición corporal (BPC). Por lo tanto, en el capítulo 3 se explora la posibilidad de utilizar análisis de componentes periódicos (πCA), una técnica LSR que maximiza el contenido de major periodicidad de la TW latido a latido en las derivaciones independientes, en lugar

de PCA. El objetivo es comparar el rendimiento de las dos técnicas en la generación de una derivación de ECG transformada a partir de la cual se pueden derivar de manera confiable marcadores time warping para monitorear $\Delta[K^+]$ de forma no invasiva. Los resultados revelan que el rendimiento, en el seguimiento de $\Delta[K^+]$ durante la HD, de los marcadores basados en πCA fue superior al de los marcadores calculados con PCA. Además, los marcadores basados en πCA mostraron una robustez mejorada contra BPC y ruido. De acuerdo con estos hallazgos, πCA supera a la PCA en términos de monitoreo en pacientes con ESRD, así como en robustez contra BPC y SNR baja, mostrando la mayor estabilidad para el monitoreo continuo post-HD.

El capítulo 4 se centra en la aplicación de modelos de ajuste lineales, cuadráticos y cúbicos para cuantificar $\Delta[K^+]$ a partir de los marcadores time warping obtenidos con πCA. La precisión de los modelos de regresión se evalúa mediante la correlación y el error de estimación entre los valores $\Delta[K^+]$ reales y los correspondientes estimados por el modelo. Los resultados apoyan el uso de modelos polinomiales, en particular cuadráticos, como sensores $\Delta[K^+]$ en pacientes con ESRD, teniendo el menor error de estimación con respecto al lineal.

El análisis time warping es sensible a los errores de delineación de los límites de la TW, una posible consecuencia de la delineación automática de los puntos de inicio y fin de la TW en el ECG. Cuando eso sucede, la potencia pronóstica de los marcadores propuestos puede reducirse drásticamente a pesar de su fuerte correlación con $\Delta[K^+]$. Por lo tanto, en el capítulo 5 se propone una etapa de ponderación en el cálculo de marcadores time warping. En particular, se prueban dos funciones de ponderación (WF)s y se comparan sus resultados con respecto al caso de control, cuando no se aplica ponderación, para evaluar sus desempeño en escenarios simulados y en casos reales (es decir, para el seguimiento de $[K^+]$ y estratificación del riesgo de SCD). Por un lado, no se encuentran mejoras en el monitoreo de $[K^+]$ probablemente debido a los considerables cambios morfológicos de la TW inducidos por $[K^+]$ que pueden haber enmascarado cualquier posible efecto secundario de los errores de delineación de la TW. Por otro lado, tanto las pruebas de simulación como el análisis de estratificación del riesgo de SCD muestran que los WFs propuestos pueden mejorar la robustez del análisis time warping contra los errores de delineación de las TW. Entonces, el empleo de una etapa de ponderación puede aumentar la confiabilidad clínica de los índices derivados del análisis time warping en la estratificación del riesgo de SCD.

En conclusión, en esta tesis se han investigado marcadores derivados de ECG basados en el análisis time warping de la TW en un intento de desarrollar un nuevo método para la estimación de $\Delta[K^+]$ en pacientes con ESRD sometidos a terapia de HD. A diferencia de los marcadores propuestos anteriormente, estos explotan la morfología general de la TW y se ha demostrado su capacidad de seguimiento y cuantificación $\Delta[K^+]$ a través de modelos de regresión polinomial . Finalmente, se ha probado una etapa de ponderación para minimizar los efectos no deseados de los errores de delineación de la TW en el cálculo de marcadores time warping, lo que resulta en una mejora notable del poder de estratificación del riesgo de SCD.

Palabras clave: Enfermedad renal en etapa terminal; Monitorizacióon no invasivo de potasio; Medicina personalizada; Electrocardiograma; Procesamiento de ondas T; Análisis time warping; Análisis de componentes principales; Análisis de componentes periódico; Muerte cardíaca súbita; Predicción de riesgos.

Contents

List of Figures

List of Tables

Acronyms

πCA Periodic component analysis
AFB Acetate-free biofiltration
AKI Acute kidney injury
AP Action potential
AUC Area under the curve
AVN Atrioventricular node
BPC Body position changes
bw Baseline wander noise
CD Cardiac death
CE Cardiac event
CHF Chronic heart failure
CI Confidence interval
CKD Chronic kidney disease
CNN Convolutional neural network
CV Cardiovascular
CVD Cardiovascular disease
dB decibel
DM Diabetes mellitus
ECG Electrocardiogram
em Electrode motion artefacts noise
ESRD End stage renal disease
HAR Hazard ratio
HD Hemodialysis
HF Heart failure
HR Heart rate
HRV Heart rate variability
IQR Interquartile range
LSR Lead space reduction
ma Muscle activity noise
MSC Morphology combination score
MUSIC MUerte Súbita en Insuficiencia Cardiaca
MWTW Mean warped T wave
NN Neural network
NSTDB Noise Stress Test Database
PC Principal component(s)
PCA Principal component analysis
PFD Pump failure death
ROC Receiver operating characteristic
SAN Sinoatrial node
SCD Sudden cardiac death
SL Single lead
SNR Signal-to-noise ratio
SRSF Square-root slope function
std Standard deviation
TL Transformed lead
TMR T-wave morphology restitution
TW T wave
WF Weighting function
WT Wavelet transform

CHAPTER 1

Introduction

1.1 Motivation of the thesis

Maintenance of blood potassium concentration ($[K^+]$) homeostasis is important for many physiologic processes, such as cardiac electrical conduction [1, 2]. Impairment of $[K^+]$, also called *dyskalemia* (i.e. $[K^+]$ outside its normal range: 3.5 – 5.0 mmol/L), can be caused by comorbidities such as chronic kidney disease (CKD), heart failure (HF), cardiovascular disease (CVD) and diabetes mellitus (DM) [3, 4]. Hemodialysis (HD) treatment, a procedure performed by means of external body equipment, is one of the possible forms of renal replacement therapy [5] commonly employed to restore $[K^+]$ balance in the event of dyskalemia [6].

During the past years, several studies confirmed the association between alterations in plasma electrolyte concentrations, such as potassium, and an increase in mortality risk [7–11]. Therefore, a rapid non-invasive diagnostic tool for early detection of dyskalemia would be a desirable. Such a device not only would improve and optimise the strategies of treatment, but also could enhance patient outcomes in emergency settings. In addition, academic and clinical investigations may also benefit from a non-invasive, rapid, and cost-efficient tool for diagnosis of $[K^+]$ imbalance.

Currently, all the routine medical tests to assess $[K^+]$ require blood analyses, an invasive and costly procedure that limits a continuous follow-up [12]. Conversely, the electrocardiogram (ECG) is a non-invasive, easily accessible, and inexpensive diagnostic tool that reflects the electrical activity of the heart and it is commonly employed in clinical practice [13, 14] and well established in other diagnostic domains, such as home monitoring by Holter ECG measurements [15–17]. Previous studies highlighted the strong relationship between plasma electrolytes (like potassium) and genesis of cardiomyocyte action potentials (APs) which lead to ECG sequence changes [18, 19]. Hence, ECG analysis would help for real-time plasma

electrolyte concentration assessment likewise in retrospective studies. For this purpose, researches are mostly conducted on patients undergoing HD therapy since they experience high $[K^+]$ oscillation [20] and suffer from a 14-fold increased risk of dying from sudden cardiac death (SCD) compared to patients with CVD without known $[K^+]$ impairment [21]. In other words, investigating patients undergoing HD is of great interest because they are at high risk for SCD as well as the relative ease with which ECG signals and complementary electrolyte concentrations information can be collected.

Various ECG indices have been proposed to monitor and to predict electrolyte variation in patients under HD treatment that could be used in clinical practice to trigger an alarm for clinicians and, thus, prevent patients from possible life-threatening clinical complications. The majority of these indexes are based on the analysis of some ECG features such as QT interval or the T wave (TW). On the one hand, the effects of HD on QT interval, and its corrected version QTc, are still controversial [22]. On the other hand, it is well known that TWs are frequently altered in HD patients [23]. However, the TW-based markers that have been proposed so far rely on specific local features of the TW.

Therefore, a methodological advanced method to estimate $[K^+]$ variations in patients undergoing HD therapy, based on the analysis of the whole morphology of the TW, is proposed in this thesis. This method would allow a more reliable $[K^+]$ estimation, thus facilitating the decision-making process of clinicians which in turn, may improve the quality of life of these patients. The clinical value of the proposed method is then assessed in both simulated and clinical databases.

1.2 The kidneys

The renal system consists of the kidney, ureters, and the urethra. The overall function of the system filters approximately 180 liters of fluid a day from renal blood flow which allows for toxins, metabolic waste products, and excess ion to be excreted while keeping essential substances in the blood [24].

In humans, there are two kidneys located high in the abdominal cavity, one on each side of the spine which lie in a retroperitoneal position at a slightly oblique angle. The asymmetry within the abdominal cavity, caused by the position of the liver, typically results in the right kidney being slightly lower and smaller than the left, and being placed slightly more to the middle than the left kidney [24, 25].

1.2.1 Structure and main functions of kidneys

Each kidney is covered by three layers made out of fat or connective tissue, called the kidney capsule (or renal capsule). These layers give the kidney extra stability, protect it from injury from the outside, and attach it to the surrounding tissue [26]. The kidney is made up of two main parts as depicted in Figure 1.1. The outermost layer is called the renal cortex, it contains about 1.2 million renal corpuscles and is where urine is produced. The renal medulla is found inside the kidney and houses blood vessels and winding renal tubules through which the urine flows. The urine then reaches the renal pelvis, runs through the ureter and, finally, it is stored in the urinary bladder before it is disposed of by urination [26].

The kidney regulates plasma osmolarity by modulating the amount of water, solutes, and electrolytes in the blood [27]. It ensures long term acid-base balance [28] and also produces erythropoietin which stimulates the production of red blood cell [29]. It also produces renin for blood pressure regulation [30,31] and carries out the conversion of vitamin D to its active form [24,32].

1.2.2 Renal failure

The term renal failure denotes inability of the kidneys to perform excretory function leading to retention of nitrogenous waste products from the blood [33]. Kidney failure can be divided into two categories: acute kidney injury (AKI) and chronic kidney disease (CKD).

Acute kidney injury is defined as an acute or subacute damage and/or a loss of kidney function for a duration of between 7 and 90 days after exposure to an AKI-initiating event, and a recovery within 48 h is typically associated with the rapid reversal of AKI[34]. AKI is characterized by an acute decrease in renal function that can be multi-factorial in its origin and is associated with complex patho-physiological mechanisms [35, 36]. In the short term, AKI is associated with an increased length of hospital stay,

health care costs, and in-hospital mortality, and its impact extends into the long term, with AKI being associated with increased risks of adverse cardiovascular CV events, progression to CKD, and long-term mortality [37].

Chronic kidney disease affects between 8% and 16% of the population worldwide and is often unrecognised by patients and clinicians [38–41]. CKD is defined by a glomerular filtration rate of less than 60 mL/min/1.73 m^2, albuminuria of at least 30 mg per 24 hours or any other indicators of kidney damage persisting for more than 3 months [42]. The causes of CKD vary globally, and the most common primary diseases causing CKD and ultimately end-stage renal disease (ESRD) are: type 2 DM (30% to 50%), type 1 DM (3.9%), hypertension (27.2%), primary glomerulonephritis (8.2%), chronic tubulointerstitial nephritis (3.6%), hereditary or cystic diseases (3.1%), and plasma cell dyscrasias or neoplasm (2.1%) [41, 43]. ESRD is defined as irreversible decline in a person's own kidney function, which is severe enough to be fatal in the absence of HD or transplantation [44, 45].

1.2.3 Hemodialysis

Hemodialysis, also spelt haemodialysis, or simply dialysis, is a process of artificially purifying the blood of a person whose kidneys are not working normally. HD is one of three renal replacement therapies being the other two: kidney transplant and peritoneal dialysis [46, 47] - both of them not covered in this thesis. Routine HD is conducted in a dialysis outpatient facility, either a purpose built room in a hospital or a dedicated, stand-alone clinic.

In HD therapy, the wastes and excess water are removed by using an external filter called a dialyzer (Figure 1.2), which contains a semipermeable membrane. The separation of wastes is done by creating a counter-current flow gradient, where blood flow is in one direction and the fluid of the dialyzer is in the opposite direction. Thus, the basic principle involved in HD is the movement or diffusion of solute particles across a semipermeable membrane (diffusion). Metabolic waste products, such as urea and creatinine, diffuse down the concentration gradient from the circulation into the dialysate (sodium bicarbonate, sodium chloride, acid concentrate, and deionized water) [48]. During their diffusion into the dialysate, the size of particles, in turn, determines the rate of diffusion across the membrane. The larger the size of the solute particle, the slower is the rate of diffusion across the membrane [48].

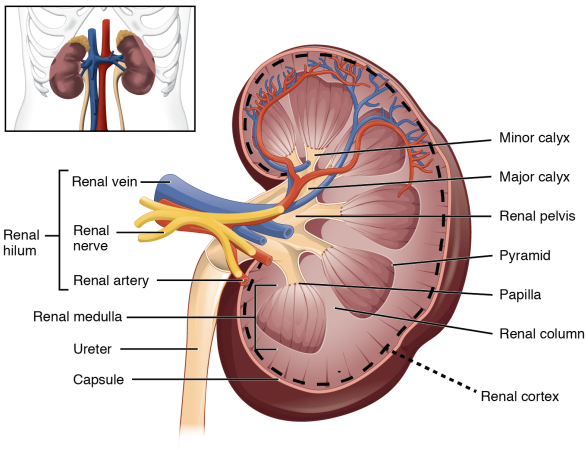

Figure 1.1: Internal anatomy of the left kidney. A frontal section through the kidney reveals an outer region called the renal cortex and an inner region called the renal medulla. In the medulla, 5-8 renal pyramids are separated by connective tissue renal columns. Each pyramid creates urine and terminates into a renal papilla. Each renal papilla drains into a collecting pool called a minor calyx; several minor calyces connect to form a major calyx; all major calyces connect to the single renal pelvis which connects to the ureter. Figure adapted from [49].

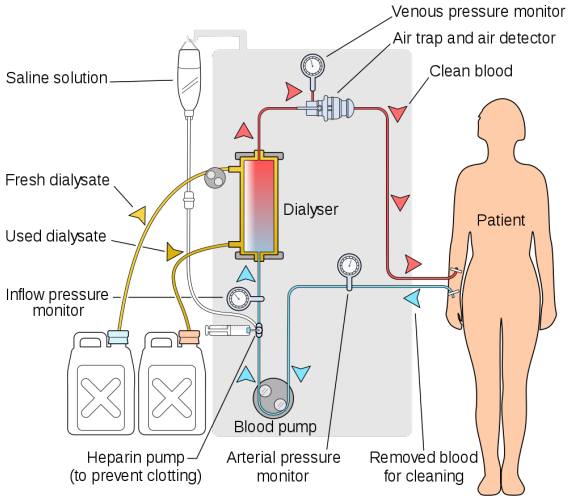

Figure 1.2: Schematic representation of a HD machine connected to a patient. Blood from an artery is pumped into a dialyzer and flows through a semipermeable membrane which allow the exchange of urea and waste materials between blood and fresh dialysate, moving in counter-current flow direction, by diffusion. After that, dialysate fluid is returned back, while purified blood is forced in a venous pressure monitoring and air traps system before being reintroduced into the patient's bloodstream. Figure adapted from [50].

1.3 The heart

The heart is a muscular organ situated in the center of the chest behind the sternum [51]. It consists of four chambers: the two upper chambers are called the right and left atria, and the two lower chambers are called the right and left ventricles [52]. The right atrium and ventricle together are often called the right heart, and the left atrium and left ventricle together functionally form the left hear. The synchronised contraction of these four chambers forces the blood into further circulation across the body.

During each cardiac cycle (heart beat), the atria contract in diastole to fill the ventricles, which, then, contract during systole to supply blood to the lungs and the systemic circulation. The wall of the heart is called the *myocardium* and is primarily composed of muscle cells (*myocytes*) that produce mechanical force during contraction of the heart [53]. Contraction of the atria and ventricles is triggered by a wave of electrical excitation (*depolarization*) spreading through the myocardium of these chambers. The depolarization wave reflects movement of charge across the myocyte membranes, which results in an electrical current spreading through the heart. Following systole, cardiac muscle returns to a resting state and this is associated with reversal of the movement of charge across the myocyte membranes. This second wave of electrical activity is termed cardiac *repolarization* [54].

1.3.1 Electrical activity of the heart

An electrical conduction system regulates the pumping of the heart and timing of contraction of various chambers. Heart muscle contracts in response to the electrical stimulus received. The sinoatrial node SAN (Figure 1.3) is the main pacemaker of the heart [55], is situated at the junction of the superior vena cava and the right atrium. It rhythmically generates an electrical discharge which is carried to through the left atrium. In a normal heart, the only route by which the depolarizing wave can enter the ventricular conducting system is the atrioventricular node (AVN). The AVN receives the electrical signal and conducts it to the bundle of His with some delay [56]. This delay allows the emptying of the atria into the ventricles before the ventricles contract in response to the electrical signal. The bundle of His divides into the right and left bundles that successively branch into thousands of small branches called Purkinje fibers. The His-Purkinje tree serves to rapidly conduct the electrical signal to all parts of both ventricles to produce a near-simultaneous contraction of all parts of both ventricles, producing a uniform and coordinated squeeze [54, 57]. In the walls of the ventricles, depolarization spreads from the terminal fibers of the conducting system outwards from the inner layer (*endocardium*) towards the outer surface of the heart (*epicardium*), and also back along the ventricular wall to the atrioventricular groove [58].

1.3.2 Phases of the cardiac action potential

Similar to skeletal muscle, the resting membrane potential (voltage when the cell is not electrically excited) of ventricular cells, is around -85 to -90 millivolts (mV). In other words, the inside of the cell membrane is more negative than the outside. The main ions found outside the cell at rest are sodium (Na^+), chloride (Cl^-) and calcium (Ca^{2+}), whereas inside the cell it is mainly potassium (K^+) [59]. These four ions are primarily involved in the genesis and propagation of the cardiac action potentials (AP) and thus the contraction and subsequent relaxation of the heart. AP consists of 5 phases, numerated from 0 to 4 [57, 60] as depicted in Figure 1.4.

- **Phase 4:** In the ventricular myocyte, phase 4 occurs when the cell is at rest, in a period known as diastole. The resting membrane potential results from the flux of ions having flowed into the cell (e.g. Na^+) and the ions having flowed out of the cell (e.g. K^+ and Cl^-) being perfectly balanced.
- **Phase 0** corresponds to the depolarization phase where an initial fast upstroke results due to the opening of the fast inward Na^+ channels. This opening causes a rapid increase in the membrane conductance to Na^+ and thus a rapid influx of Na^+ ions into the cell, i.e. a Na^+ current. The ability of the cell to open the fast Na^+ channels during phase 0 is related to the membrane potential at the moment of excitation. If the membrane potential is at its baseline, all the fast Na^+ channels are closed, and excitation will open them all, causing a large influx of Na^+ ions. If, however, the membrane potential is less negative, some of the fast Na^+ channels will be in an inactivated state

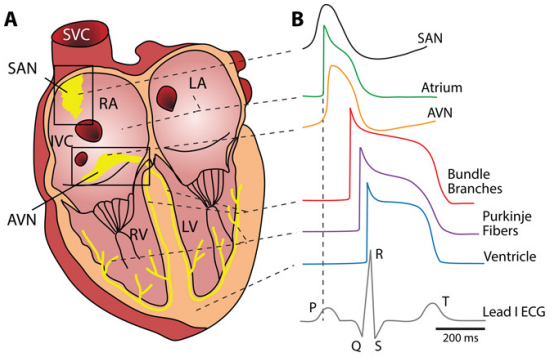

Figure 1.3: Electrical conducting system of the heart. A) Schematic of different regions of the human heart and the corresponding B) AP waveforms (below is a representative lead I ECG). Figure adapted from [61]. SVC: superior vena cava, SAN: sinoatrial node, RA: right atrium, LA: left atrium, IVC: interventricular septum, AVN: atrioventricular node, RV: right ventricle, LV: left ventricle

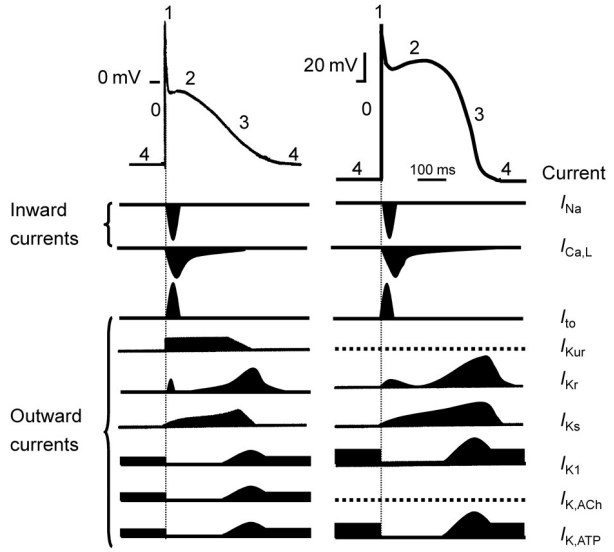

Figure 1.4: Inward, depolarising and outward, repolarizing currents that underlie the atrial (on the left) and ventricular (on the right) action potential. Inward currents: I_{Na} sodium current; $I_{Ca,L}$ L-type calcium current; I_{to} transient outward current; I_{Kur} ultra rapidly activating delayed rectifier current; I_{Kr} and I_{Ks} rapidly and slowly activating delayed rectifier current; I_{K1} inward rectifier current; $I_{K,ACh}$ acetylcholine-activated potassium current. Note that I_{Kur} is present in atria only. Phase 0, rapid depolarization; phase 1, rapid early repolarisation phase; phase 2, slow repolarization phase ('plateau' phase); phase 3, rapid late repolarization phase; phase 4, resting membrane potential. Figure adapted from [19].

insensitive to opening, thus causing a lesser response to excitation of the cell membrane and a lower maximum potential. For this reason, if the resting membrane potential becomes too positive, the cell may not be excitable and conduction through the heart may be delayed.

- **Phase 1:** represents an initial and brief repolarization and occurs with the inactivation of the fast Na^+ channels. The transient net outward current causing the small downward deflection of the AP is mainly due to the movement of potassium (K^+) ions, carried by the transient outward potassium current I_{to1}. Particularly the transient outward potassium current I_{to1} contributes to the "notch" of some ventricular myocyte AP.

- **Phase 2:**, also called "plateau" phase of the cardiac AP, is sustained by a balance between inward movement of calcium Ca^{2+} through L-type calcium channels and outward movement of K^+ through the slow delayed rectifier potassium channels, I_{Ks}. This plateau phase prolongs the AP durations and distinguishes cardiac AP from the much shorter AP found in nerves and skeletal muscle.

- **Phase 3:**, the "rapid repolarization" phase, the L-type Ca^{2+} channels close, while the slow delayed rectifier (I_{Ks}) K^+ channels are still open. This ensures a net outward current, corresponding to a negative change in membrane potential, thus allowing more types of K^+ channels to open. These are primarily the rapid delayed rectifier K^+ channels (I_{Kr}) and the inwardly rectifying K^+ current, I_{K1}. This net outward, positive current (equal to loss of positive charge from the cell) causes the cell to repolarize. The delayed rectifier K^+ channels close when the membrane potential is restored to about -80 to -85 mV, while I_{K1} remains conducting throughout phase 4, contributing to set the resting membrane potential.

In the heart, the wave of depolarization current originates in the SA node under normal conditions and reaches the ventricular myocardium via the conduction system. Anatomically the ventricular depolarization travels from apex to base and from endocardium to epicardium while the wave of repolarization moves in the opposite direction from epicardium to endocardium. Thus the AP duration is not the same across

the walls of the heart, with myocytes near the epicardium depolarizing last and repolarizing first. This repolarization time differences, or dispersion of repolarization, not only exist between cells of different chambers of the heart (i.e. atria, ventricles, nodal tissue) [62, 63], but also between myocytes of different regions within the ventricular wall, e.g. epicardium versus endocardium [64–70], or apex versus base [69, 71–78]. Dispersion of repolarization is due to an intrinsic difference in the activity of the various ion channels which can strongly influence the arrhythmia vulnerability [79].

1.4 The electrocardiogram

An electrocardiogram (ECG; in German, the electrokardiogram, EKG) is a measure of how the electrical activity of the heart changes over time as APs propagate throughout the heart during each cardiac cycle. However, this is not a direct measure of the cellular depolarization and repolarization with the heart, but rather the relative, cumulative magnitude of populations of cells eliciting changes in their membrane potentials at a given point in time [80]. Indeed, ECG signal shows electrical differences across the heart when depolarization and repolarization of these atrial and ventricular cells occur.

In the clinical practice, a number of lead configurations are used with standardized electrode positions [57], including the standard 12-lead ECG and the 3-lead orthogonal configuration. If these leads are appropriately placed, the ECG recording can provide information about disease processes affecting different anatomical regions of the organ and can allow the detection of changes in the pattern of spread of electrical forces through the heart in disease. The selection of a particular lead system is guided by the type of clinical information desired and other practical considerations. For example, a few electrodes are usually used when only heart rhythm information is required, while ten electrodes (12-lead configuration) is preferred when wave's morphology needs to be analysed [53].

1.4.1 The lead system

The standard 12-lead ECG

Since the flow of depolarization and repolarization through the myocardium is a three dimensional process, it is important to realize that each of the leads of the ECG recording system examines the movement of the electrical waves through the heart in one plane only. In fact, based on the plane in which electrical events in the heart are analysed, the 12 leads of the ECG can be divided into two groups of six. The six *frontal* leads examine the flow of depolarization and repolarization through the heart in the vertical, or frontal, plane (Figure 1.5 (left)), while a second group of six leads, the *chest* leads, also referred to as the *precordial* leads, V1 to V6, examine these electrical events in the horizontal or transverse plane [53] (Figure 1.5 (right)).

The frontal leads can be further divided in two groups of three, the *standard limb* leads, leads I, II and III, and the *augmented vector* leads, aVR, aVL and aVF. By taking a representative frontal section through the chest, the perspective of each of these leads on cardiac electrical events can be understood. To remember the position of all 6 of the frontal leads relative to the heart, lead I is used as the reference point. Lead I looks directly at the heart from the patients left hand side and defines zero degrees. Lead II looks at the heart at an angle 60° further clockwise from lead I, while lead III is positioned a further 60° clockwise from lead II. aVL looks at the heart from the left (L is for left), but at 30° anticlockwise from lead I. aVR looks at the right side of the heart (R is for right), and, just like aVL, it is 30° above the horizontal relative to lead I. As aVL and aVR are set at 30° off the horizontal plane, they can be thought as the left and right Wings or "vings" of the ECG. aVF looks straight up at the inferior surface of the heart and is, therefore, at 90° clockwise from lead I, and can be thought of as looking straight up at the heart from the feet (F is for feet) [53].

The six chest leads, V1 to V6, are placed on the surface of the chest wall in an arc, from V1 in the 4th right intercostal space to the right of the sternum, to lead V2 in the fourth left intercostal space to the left of the sternum, and then at roughly equal intervals, to lead V6 in the fifth left intercostal space in the mid-axillary line. If we take a representative transverse section through the chest, it can be appreciated that, with the heart in anatomical position, the atria lie posterior to the ventricles and the right ventricle lies somewhat anterior to the left in this plane. Leads V1 and V2, therefore, face the surface of the right

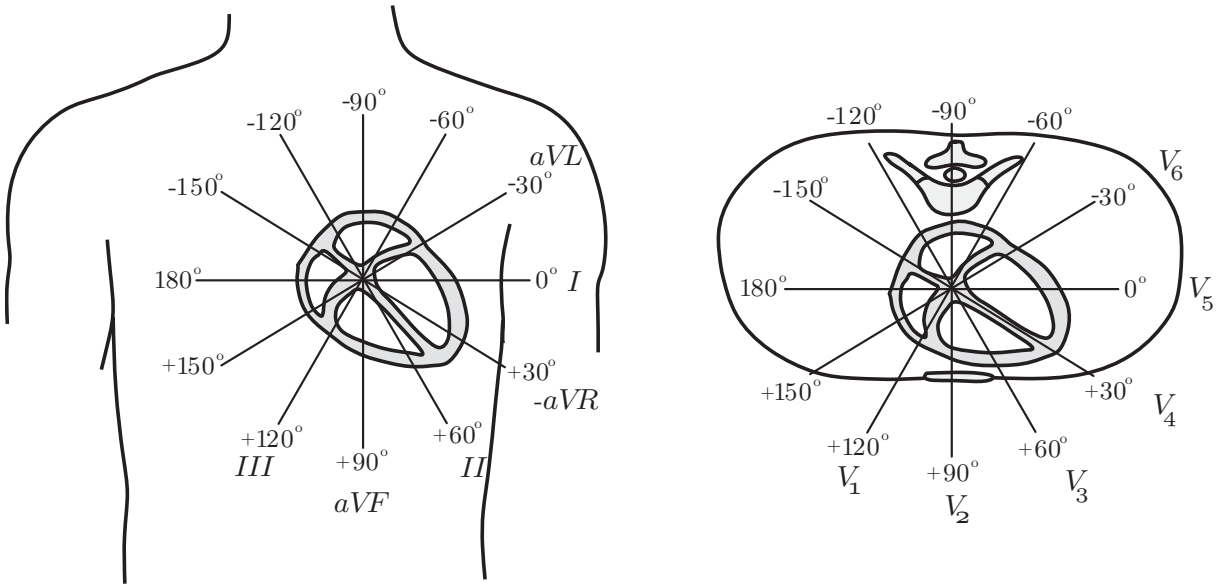

Figure 1.5: The six frontal (left) and horizontal (right) plane leads provide a three-dimensional representation of cardiac electrical activity. Figure adapted from [53].

ventricle. However, note they also face the much larger muscle mass of the interventricular septum. Then, these leads are strongly influenced by electrical events in this structure and V1 and V2 are, therefore, often referred to as the septal leads. V3 and V4 face the anterior wall of the left ventricle, while V5 and V6 face the lateral wall of the left ventricle [53].

Only eight from these twelve acquired leads are independent. Then, it would be sufficient, as an example, to only consider the six precordial leads and two augmented vector leads to represent all the information from the twelve standard leads [53].

Orthogonal Leads

The orthogonal lead system reflects the electrical activity of the heart in the right-left axis (lead X), the head-to-feet axis (lead Y) and the front-back axis (lead Z) [81]. This system, in addition to the ECG information acquired from each individual lead, provides with additional information through the visualization of a three-dimensional loop together with the projection onto the XY-, XZ- and YZ- planes (Figure 1.6). Since a loop is traced out by the tip of the vector that describes the dominant direction of the electrical wavefront during the cardiac cycle, this recording is referred to as a *vectorcardiogram* [82].

The most widely used orthogonal lead system, known as the Frank lead system after its inventor [83], is obtained as linear combinations of seven electrodes positioned on the chest, back, neck, and left foot. The resulting leads X, Y and Z view the heart from the left side, from below, and from the front [53].

1.4.2 ECG patterns

When an ECG is recorded, a reading of voltage vs time is produced, which is normally displayed as millivolts (mV) and seconds. A typical lead II ECG waveform is shown in Figure 1.7. It shows a series of peaks and waves that corresponds to ventricular or atrial depolarization and repolarization, with each segment of the signal representing a different event associated with the cardiac cycle.

ECG waveforms

The baseline of an ECG tracing is called the *isoelectric line* and denotes resting membrane potentials. Deflections from this point are lettered in alphabetical order, and following each, the tracing normally returns to the isoelectric point [84]. All of the leads on the ECG recording system are set up in such a way

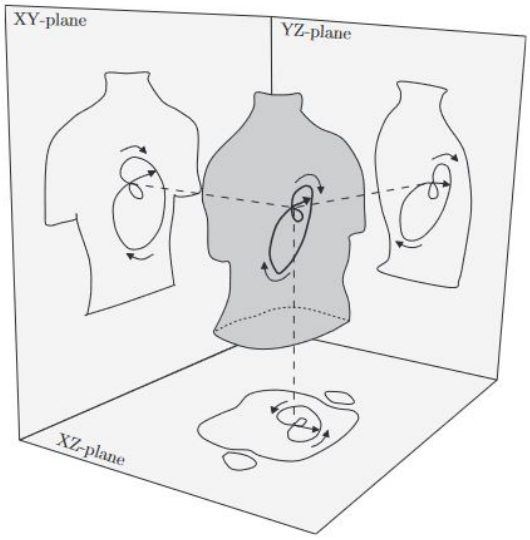

Figure 1.6: A vectorcardiographic loop and its projection onto the three orthogonal planes. The two arrows outside each loop indicate the direction in which the loop evolves. Figure adapted from [53].

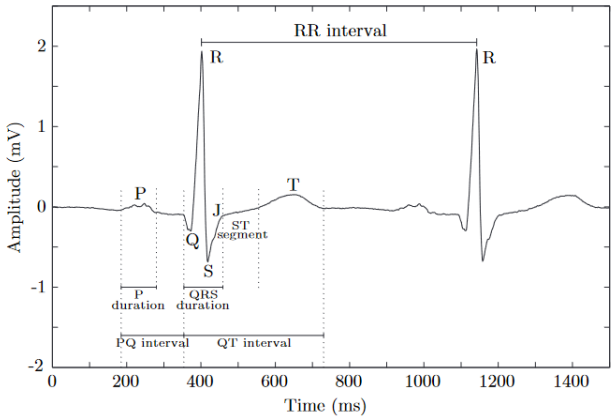

Figure 1.7: Example of ECG of two cardiac cycles with definition of main waves and most relevant time intervals. Figure adapted from [53].

that depolarizing current moving towards a lead produces a positive deflection on the ECG signal above the isoelectric line, while depolarizing current moving away from the lead produces a negative deflection below the isoelectric line. In contrast, repolarizing current has the opposite polarity to depolarizing current. Therefore, repolarizing current moving towards a lead produces a negative deflection on the signal, while repolarizing current moving away from the lead produces a positive deflection [53].

As explained in section 1.3.2, the cardiac cycle begins with the firing of the SAN in the right atrium. This firing is not detected by the surface ECG because the SAN is not composed of an adequately large quantity of cells to create an electrical potential with a high enough amplitude to be recorded with distal electrodes (signal amplitude is lost as it dissipates through the conductive medium). The atria then depolarize, giving rise to the *P wave*. This represents the coordinated depolarization of the right and left atria and the onset of atrial contraction. The P wave duration is less than 120 ms [53]. As the P wave ends, the atria are completely depolarized and are beginning contraction.

The ECG signal then returns to baseline, and an AP (not large enough to be detected) spread to the atrioventricular node and bundle of His where it triggers the ventricular depolarisation. Thus, the right and left ventricles begin to depolarize, resulting in what is called the *QRS complex*, representing the beginning of ventricular contraction, which is around 70-110 ms in duration. Typically, the first negative deflection is the Q wave, the large positive deflection is the R wave, and if there is a negative deflection after the R wave, it is called the S wave. The exact shape of the QRS complex depends on the placement of electrodes from which the signals are recorded [53].
Simultaneous with the QRS complex, atrial contraction has ended, and the atria are repolarizing. However, the effect of this global atrial repolarization is sufficiently masked by the much larger amount of tissue involved in ventricular depolarization and is thus not normally detected in the ECG.

When ventricular depolarization is complete, there is a brief period when no current is flowing and the recording returns to the isoelectric line. This period ends with the onset of ventricular repolarization. The deflection produced on the ECG by ventricular repolarization is again dominated by the signal from the left ventricle. As the repolarizing wave is moving away from the chest, it produces a positive deflection. This deflection is termed *T wave* (TW). Note that the TW has a very different morphology to the QRS complex. Cardiac repolarization spreads relatively slowly through the myocardial muscle mass, outside the conducting system. Hence, the TW is considerably longer in duration and, therefore, broader on the ECG signal than the QRS complex. In non-diseased hearts, the polarity of the QRS complex and the TW tend to be concordant [53].

ECG intervals and segments

Of clinical importance in the ECG waveform are several notable parameters (regions), which include the *RR interval*, the *PQ interval*, the *ST segment*, and the *QT interval*. The RR interval represents the length of a ventricular cardiac cycle, measured between two successive R waves, and serves as an indicator of ventricular rate. It is a fundamental rhythm quantity in any type of ECG interpretation and is used to characterise different arrhythmia as well as to study the heart rate variability [53]. The PQ interval is measured from the beginning of the P wave to the beginning of the QRS complex and is basically a measure of the time it takes for AP to travel from atrial excitation and through the atria. The ST segment is the period of time when the ventricles are completely depolarized and contracting and is measured from the S wave (the J point) to the beginning of the TW Figure 1.7. The QT interval is measured from the beginning of the QRS complex to the end of the TW; this is the time segment from when the ventricles begin their depolarization to the time when they have repolarized to their resting potentials [80].

1.4.3 Dyskalemia and ECG changes

As previously mentioned in section 1.3.2, potassium is the predominant intracellular ion and is the major determinant of the myocardial resting membrane potential. ESRD patients can experience hypo ($[K^+] \leq 3.5$ mmol/L) [85] or hyperkalemia ($[K^+] \geq 5.0$ mmol/L) [86], both of them can cause changes in the ECG.

The earliest ECG change associated with hypokalemia is a decrease in the TW amplitude [87]. As $[K^+]$ declines further, ST-segment depression and TW inversions are seen, while the PR interval can be prolonged along with an increase in the amplitude of the P wave [87]. When the U wave, which is described as a positive deflection after the TW often best seen in the mid-precordial leads (e. g. V2 and V3), exceeds the TW amplitude the $[K^+] < 3$ mmol/L [88]. In severe hypokalemia, T- and U-wave fusion with giant U waves masking the smaller preceding TW [87,88]. A pseudo-prolonged QT interval may be seen, which is actually the QU interval with an absent TW [89].

Typical ECG findings in hyperkalemia progress from tall and narrow ("peaked" or "tented") TW ($[K^+]$ from 5.0 to 6.5 mmol/L), loss of P waves ($[K^+]$ from 6.5 to 7.5 mmol/L), to widening of the QRS complex ($[K^+]$ from 7 to 8 mmol/L) culminating in cardiac arrhythmias, "sine wave" pattern, and asystole ($[K^+]$ from 8 to 10 mmol/L) [90,91].

1.5 Review of the state of the art

Over the past decades, several publications successfully investigated and reported the intrinsic connection between electrolyte imbalances and the variations on the ECG signal [88, 92–98]. Typical changes caused by both hypo- and hyperkalemia were reported for each waveform in the ECG as described in section 1.4.3. However, in addition to these single beat aspects, rhythmical features such as the heart rate variability (HRV) parameters were studied as well.
Therefore, this section aims to provide a focused analysis and discussion of recent researches concerning the incidence of ECG feature changes in clinical studies and the approaches for capturing those features apart from the common temporal and morphological ones.

1.5.1 Associations between serum electrolyte concentrations and changes in cardiac electrophysiology

Several studies have discussed the incidence of electrolyte change-induced ECG abnormalities and the idea of using the ECG as a monitoring tool to prevent adverse outcomes.

In a recent meta-analysis [99], linear regression analyses examining associations between electrolyte concentrations (mmol/l of calcium, potassium, sodium, and magnesium), and electrocardiographic intervals: RR, QT, QRS, PR and JT (this later defined as the difference between QT and QRS and PR intervals) were performed over a large cohort study (153014 individuals). The study identified physiologically

relevant associations between electrolytes and those electrocardiographic intervals. In particular, they found that potassium concentration variations mainly influenced QRS interval.

Apart from those interval changes, there are typical morphological features described in the literature, especially in the case of potassium variation as mentioned in in section 1.4.3.Another approach is to analyse the time series of beats yielding to rhythmical features.

ECG features related to cardiac rhythm

Reduced HRV has been shown to be associated with adverse CV outcomes and mortality in HD patients [100, 101], and HD itself may enhance HRV [102, 103]. With this assumption, Chen *et al.* [104] proposed a parameter, based on the linear changes in HRV before and after HD, as a possible CV mortality risk stratification method in HD patients. Some alterations have been also found in several non-linear HRV indexes in HD patients [105] which led to the proposal of both methods: the *recurrence plot analysis* [106], capturing HRV changes also in ambulatory ECGs, and the *Poincaré plot* [107], able to evaluate the magnitude of variations in the HRV. The connection between HRV and a change of plasma electrolyte concentrations was also reported by El-Sherif and Turitto [88] and all these studies seem to highlights the relationship of the rhythmical features change between pre- and post-HD.

However, the potential additional benefit, obtained by using HRV-related descriptors, to the problem of electrolyte concentration estimation in clinical practice is still to be validated [108].

QT interval changes and electrolyte concentration variations

Prolonged QT intervals, as collective measures of ventricular depolarization and repolarization, as been consistently associated with adverse outcomes such as SCD [109–111]. Moreover, QT interval prolongation is common among those patients undergoing HD treatment and represents a potential common pathway leading to arrhythmias and potentially SCD [112]. Many studies have been carried out to understand the connection between electrolyte concentration changes, SCD occurrence, and changes of the QT interval.

A recent retrospectively research [113] proved that QT adjusted for heart rate (QTc) interval in patients with CKD at 1 year after HD initiation was longer than in the control subjects and was further prolonged over several years of HD treatment. Later, it was demonstrated that different combinations of K^+ and Ca^{2+} concentrations in the dialysate lead to different modifications of the QT interval duration [114, 115].

Genovesi *et al.* [102] as well as Kim *et al.* [116] found that the prolongation of the QTc was related to the changed electrolyte concentration variations (including potassium) and associated with SCD and total mortality in a case series of patients undergoing HD. In addition, QTc dispersion increases during HD treatment as a consequence of the potassium removal rate during HD sessions [117].

Therefore, QT, QTc, and QT dispersion seem to be closely related to electrolyte concentration changes and rate of change and and can be influenced in HD patients also by the dialysate potassium concentration. Nevertheless, no studies directly reconstructed potassium concentrations from the changes in the QT interval has been performed [108].

Influence of the HD on the P wave

Many studies have confirmed that the incidence of atrial and ventricular arrhythmias is higher during HD [118–120], being the mortality primarily connected with thromboembolic consequences [121, 122]. In patients with paroxysmal atrial fibrillation during sinus rhythm, the intra- and interatrial conduction time of the sinus impulse lengthens, and the duration of the P wave measured on the ECG is increased [123–127]. Furthermore, HD may lengthen P wave duration and dispersion [128]. Therefore, several studies investigated the effects of HD on P wave duration and dispersion, two features that characterize atrial arrhythmogenicity and are measured by a surface ECG.

However, results are still controversial. On the one hand, Chen *et al.* [129] and Páll *et al.* [122] concluded that HD can affect both P wave duration and P wave dispersion as well as P wave dispersion corrected by heart rate. On the other hand, no difference was noted in P wave amplitude by Montague *et al.* [130], although authors specified that the small sample size of the P waves examined could have limited the precision of the assessment in this regard.

1.5.2 Blood potassium concentration estimation from the ECG

This paragraph presents the most relevant attempts to estimate blood potassium concentration from the ECG by means of manual or semi-automatic potassium estimation approaches.

T wave morphology changes based methods

Electrocardiographic effects of potassium have been well known for many years [88]. In particular, narrow-based, peaked TWs are the earliest effects of the hyperkalemia on the ECG, as reported in a recent study by An *et al.* [131]. In physiological conditions, they can be described by their symmetry, skewness, slope and amplitude but in pathological conditions, the shape of the TW may change [132]. Therefore, measurements of those parameters could identify the onset of specific diseases. In the literature, it is reported that tall and narrow symmetrical TWs may indicate hyperkalemia [86], while flat TWs may indicate hypokalemia [133].
Following these consideration, different TW morphology descriptors based approaches have been previously reported to be correlated with $[K^+]$ and tested for blood electrolyte concentration reconstruction.

One of the first attempt to estimate blood potassium level from the ECG was made by Frohnert *et al.* [134] which proposed a set of equations based on the TW amplitude and TW maximum time manually extracted. However, no performance evaluation was performed and the models were built with all the available data, i.e., no independent validation was carried out [108].

Recently, Dillon *et al.* [135] assessed the following features: TW down slope, TW amplitude, the center of gravity of the TW and of the last fourth of the TW, and the ratio between the TW and R peak amplitude for blood potassium concentration estimation. Among all of them, the TW down slope, was the parameter showing the highest dependence on the plasma potassium concentration, followed by the two center of gravity features. Following that study, Velagapudi *et al.* conducted a research trying to diagnose hyperkalemic patients by using the TW slope, TW width and QRS duration to build a regression model for potassium concentration estimation [136]. They found that ECG-based models incorporating those parameters can improve detection of hyperkalemia by surface ECG.

Finally, Regolisti *et al.* [137] investigated 28 categorical and continuous clinical variables as a candidate for the construction of potassium predictive models among which are: peaked TW, TW maximum amplitude, TW/R wave maximum amplitude ratio, age and loop diuretics. The selection algorithm based on Bayesian information criterion identified TW amplitude and use of loop diuretics as the best subset of variables predicting blood potassium. Nonetheless, the authors reported that the model accuracy was poor in both full and test sample as well as in predicting hyperkalemia in both full and test sample – area under the curve (AUC) at receiver operating characteristic (ROC) curve analysis 0.74 and AUC 0.72, respectively. However, one needs to bear in mind that this study was performed over patients with acute kidney injury which, in contrast to ESRD, develops suddenly from an acute renal insult and, most importantly, is reversible [138].

Manual and U wave - ST segment based approaches

Wrenn *et al.* [139] investigated whether physicians can predict hyperkalemia form the ECG. Two physicians blinded not only to the specific clinical diagnosis of the 220 patients involved (87 patients had hyperkalemia, and 133 did not) in the study and to their blood potassium measurement but also to each other's interpretation, retrospectively analysed ECGs of patients at high risk for hyperkalemia. The physicians predicted the presence or absence of hyperkalemia as well as the severity of hyperkalemia on a nominal scale (mild, moderate, or severe) and sensitivity, specificity, and positive and negative predictive values (PPV/NPV) were computed. The results (best result for each parameter separately) were a sensitivity of 0.43, a PPV of 0.65, a specificity of 0.86, and a NPV of 0.69. This study confirmed the specificity of the ECG for hyperkalemia.

Johansson and Larsson [140] identified the sum of ST depression and U wave amplitude in II and V3 as the most relevant features in a cohort of 22 hypokalemic patients. They also performed a correction by subtraction of values during normokalemia of the respective patient to account for inter-patient variability. However, results showed that accurate prediction of mild hypokalemia (2.7–3.4 mmol/l) was not possible with that proposed approach.

1.5.3 Automatic, neural network and deep-learning techniques

There are two main techniques that can be used for automatic classification and quantification (regression) of electrolyte disorders: classical approach where lead selection, ECG feature selection, and model fitting are performed separately and deep learning techniques in which all the above mentioned steps are inherently integrated. In both cases, manual feature extraction is not required.

Automatic techniques

One of the most extensive evaluation of automatic estimation of potassium concentration values was performed by Corsi and Severi *et al.* [141–144]. They investigated the ratio between the TW downslope and amplitude, features, these, which were calculated from the two most significant PCA eigenleads of the 12-lead ECG using a template of the TW computed on two-minute window [108]. Then, after building a general model, patient-specific bias correction was introduced using the first and last measurement of the first session of a specific patient [141]. Finally, regression models were computed by using polynomials of first order [142] and second order [141, 143, 144] to assess the correlation between the TW descriptor and serum $[K^+]$. Results obtained from this approach were promising, being mean error of the estimated potassium concentration of -0.09 ± 0.59 mM and and a mean absolute error of 0.46 ± 0.39 mM [141]. However, the authors stated that one of the main limitations of their proposed estimator was the presence of a residual dependence of the error on the actual serum $[K^+]$ which could lead to underestimation of severe hyperkalemic conditions [141]. Therefore, as a future work, they proposed make use of others ECG-derived parameters known to be influenced by high $[K^+]$ levels (such as QRS duration or P-wave duration) to attenuate this issue [141].

To create a personalised strategy for blood potassium estimation, Attia *et al.* [145] proposed a linear regression model based on the TW down-slope normalised by the square root of TW amplitude. To accomplish this, for each session, only data from the single lateral precordial lead (i.e. one of V3 through V6) with the greatest amplitude TW was used. Kalman filter was also implemented to attenuate abrupt feature changes that cannot be related to a potassium variation. Each patient specific linear model with the chosen feature was built in the first HD session and applied to the other sessions yielding a mean absolute error of estimation of 0.36 ± 0.34 mmol/L in their database consisting of of 26 patients. With these findings, the authors suggested that, using a single lead of high-resolution ECG data may be suitable for remotely monitoring potassium in dialysis patients. This idea was investigated in a later study where they used a handheld smartphone equipped with commercially available electrodes affixed to it to acquire single-lead ECG signals, transmitting these signals to a remote server, and then processing the signals to estimate potassium levels in a prospective cohort of 21 dialysis patients [146]. In this case, the mean absolute error between the estimated potassium and blood potassium 0.38 ± 0.32 mmol/L, which is in the range of the performance of the approach using a standard 12-lead ECG.

Krogager *et al.* [147] investigated the relationship between blood potassium level and a recent proposed TW morphology markers named morphology combination score (MSC) [148–150], which was calculated based on TW asymmetry, flatness and notching using the following formula: $MCS = Asymmetry + Notch + 1.6Flatness$ [151]. The study confirmed the existence of an association between deviations in potassium concentrations and changes in TW amplitude. Moreover, the authors found a correlation between MSC and potassium, in agreement with the findings by Dillon *et al.* [135], although the repolarization parameters considered in this latter study and those included in the MSC formula are not identical.

Rodrigues *et al.* [152, 153] investigated the possibility of capturing potassium fluctuations over the long interdialytic interval using a single-lead ECG. They evaluated patient-specific TW morphology changes in the ECG using both: a model-based descriptor developed to account for overall morphology changes (θ_δ), and the descriptor proposed by Corsi *et al.* [141], over 15 hemodialysis patients with pre-existent cardiac diseases during the long interdialytic interval. Interestingly, they found θ_δ to be less affected by motion-induced noise and thus preferable for ambulatory monitoring. However, the authors acknowledged that the small number of patients included in the study could restrict the generalization of their findings. Moreover, the presence of concomitant electrolyte (calcium and bicarbonate) imbalances were not considered in the study, an aspect this, that the authors proposed to further investigate in future works.

In an attempt to characterize changes in ECG markers measuring duration, amplitude and morphology of the TW during HD in ESRD patients, Bukhari *et al.* [154] assessed the relationship between these changes $[K^+]$ and $[Ca^{2+}]$ and HR variations. Additionally, a set of human transmural ventricular fibers were simulated to unravel potential underpinnings of the high inter-individual differences in TW responses observed in the patients as a consequence of electrolyte and HR variations. The authors found high inter-patient variability in the pattern of such relationships for all analysed TW markers. This variability, accentuated during the first hours of HD, was reproduced in the simulations and shown to be influenced by differences in transmural heterogeneity. Whereas this study proved that changes in serum $[K^+]$ and $[Ca^{2+}]$ and HR strongly affect TW markers, particularly those quantifying morphological variability, the authors recognised that the reduced sample size and available number of blood samples could have biased the results obtained din this analysis. As a future work, the authors proposed including simulations in bi-ventricular models embedded in patient-specific torso models, from which more realistic ECGs can be computed.

Neural network approaches

Wu *et al.* [155] developed a two-stage artificial neural network (NN) to classify the disorder of electrolyte from 20 normal and 20 moderate hyperkalemic (5.4 - 7.4 mmol/L) individuals. A total of 17 features were selected, including TW amplitude and duration from V1 to V6 leads, P wave amplitude and duration, QRS duration, PR interval, averaged RR interval from lead II served as the inputs of artificial NN. Accuracy of 65.5%, a sensitivity of 60%, and a specificity of 65% in a patient cohort with 30 normokalemic and 30 hyperkalemic patients. However, no information regarding the validation technique is provided, and so over-fitting cannot be excluded [108].

Tzeng *et al.* [156] proposed a serial two-staged classifier implanted with K-means algorithm to screen hyperkalemia based on feature parameters extracted from 12-lead ECG from 56 normal individuals and 41 hyperkalemia patients (serum potassium level >5.3 mmol/L). Two TW volume features obtained from limb and chest leads were fed to the first stage and PR interval and QT interval and QRS complex width to the second. The classifier showed the sensitivity of 85% (95% CI=77% to 97%) and the specificity of 79% (95% CI=55% to 97%) in classifying the samples proving the ability to diagnose patients with hyperkalemia from very mild to severe degrees but no information regarding cross-validation to prevent over-fitting was given [108].

Deep-learning methods

Deep learning is a type of artificial intelligence able to identify and extract the best features itself [157] and then perform classification or regression for a given task. Deep learning uses representation methods to identify meaningful patterns from complex digital files and found applications in medicine to identify lesions in mammograms or retinal images [158, 159]. Over the last years several studies have been conducted to test the hypothesis that this technique can be applied for screen for hyperkalemia.

Recently, Galloway *et al.* [160] tested a deep-learning model, trained over a total of 1576581 ECG signals, either two (leads I and II) or four (leads I, II, V3, and V5) leads, from a multi-centre study in order to detect serum potassium levels. The model was then validated by means of retrospective data from 61965 patients at stage 3 or greater CKD. They found that using only two leads ECG, their deep-learning model was able to detect hyperkalemia in patients with renal disease with an AUC of 0.853 to 0.883 concluding that the application of artificial intelligence to the ECG may improve the screening for hyperkalemia. Nevertheless, a prospective study is required to analyse the performance of the proposed method by using ECG inputs in the home setting and, most importantly, to determine whether the model improves hyperkalemia detection, care and outcomes, as the authors stated.

Later, Lin *et al.* [161] develop a deep-learning model, named ECG12Net, to detect dyskalemias based on 864 meta-features from 66321 ECG records with corresponding $[K^+]$ within one hour before or after the signal acquisition. After training the model, they tested its performance against six clinicians, three emergency physicians and three cardiologists, which analysed 300 ECGs of different $[K^+]$. The proposed ECG12Net outperformed the clinicians with AUC for detecting hypokalemia and hyperkalemia of 0.926 and 0.958, respectively, Moreover, in detecting hypokalemia and hyperkalemia, the sensitivities were 96.7% and 83.3%, respectively, and the specificities were 93.3% and 97.8%, respectively. However, the authors

stated that the ECG12Net showed decreased sensitivity in detecting mild-to-moderate hypokalemia, which accounts for the majority of dyskalemias, leading to low weighted averages of the sensitivities

Despite the interesting results, deep-learning is often criticised for the non-transparency (also known as "black box") since the huge number of layers and features and the reason why a particular feature was extracted might not be interpretable for humans [157, 162]. Furthermore, deep learning can only be effective when large annotated datasets are available [161] then limiting its clinical application.

1.6 Objective and outline of the thesis

The main objective of this thesis is to develop a new approach to estimate $[K^+]$ variations in CKD patients undergoing HD, based on the analysis of the overall TW morphology. The content of the thesis is organised as follows:

- **Chapter 1:** The present chapter begins explaining the motivation of this thesis. Then, the kidneys functions, CKD and the mechanism of HD are introduced. Later, the chapter focuses on the electrical activity of healthy hearts and of hearts from ESRD patients highlighting the influence of $[K^+]$ on the ECG waveforms. Next, ECG-derived markers recently proposed in the literature for $[K^+]$ monitoring in ESRD patients are presented and discussed. Finally, the objective of this thesis is described.

- **Chapter 2:** In this chapter, the TW time warping analysis is presented. Then, the ability of time warping TW morphology changes markers in time (d_w) and amplitude (d_a), as well as their non-linear components (d_w^{NL} and d_a^{NL}), and the heart rate corrected counterpart ($d_{w,c}$), to monitor $[K^+]$ variations ($\Delta[K^+]$) in ESRD patients undergoing HD are investigated. In particular, their performance are compared with respect to two previously proposed $[K^+]$-related markers: width of the TW and TW slope-to-amplitude ratio. All markers are computed from standard 12-lead ECG as well as from principal component analysis (PCA)-based first transformed lead. The chapter ends presenting the results of this initial study and discussing the advantage of investigating the whole TW morphology for $\Delta[K^+]$ monitoring.

  The research described in this chapter generated the following publications:

  1. **F. Palmieri**, P. Gomis, J. E. Ruiz, B. Bergasa, D. Ferreira, A. Martín-Yebra, H. A. Bukhari, J. P. Martínez, E. Pueyo, J. Ramírez and P. Laguna. "Monitoring Blood Potassium Concentration in Hemodyalisis Patients by T-wave Morphology Dynamics Quantification" *Scientific Reports*, 2021; vol. 11, Art. no. 3883, doi: 10.1038/s41598-021-82935-5.
  2. **F. Palmieri**, P. Gomis, D. Ferreira, J. E. Ruiz, B. Bergasa, A. Martín-Yebra, H. A. Bukhari, E. Pueyo, J. P. Martínez, J. Ramírez and P. Laguna. "T-Wave Morphology Changes as Surrogate for Blood Potassium Concentration in Hemodialysis Patients." *2019 Computing in Cardiology (CinC)*, Singapore, 2019, pp. 1-4, doi: 10.23919/CinC49843.2019.9005904.
  3. **F. Palmieri**, P. Gomis, D. Ferreira, J. E. Ruiz, B. Bergasa, A. Martín-Yebra, H. A. Bukhari, E. Pueyo, J. P. Martínez, J. Ramírez and P. Laguna. "Estudio de los Cambios en la Morfología de las Ondas T como Sustituto de la Concentración de Potasio en Sangre en Pacientes de Hemodiálisis". *Actas del XXXVII Congreso Anual de la Sociedad Española de Ingeniería Biomédica*, Santander, Spain, 2019, pp. 291-294, ISBN 978-84-09-16707-4.

  Also, this work was awarded with the following prizes:

  1. *Rosanna Degani Young Investigator Award for the best written and oral presentation* "T-Wave Morphology Changes as Surrogate for Blood Potassium Concentration in Hemodialysis Patients." *2019 Computing in Cardiology (CinC)*, Singapore, 2019 - Semifinalist.
  2. *Mortara mobility fellowship* "T-Wave Morphology Changes as Surrogate for Blood Potassium Concentration in Hemodialysis Patients." *2019 Computing in Cardiology (CinC)*, Singapore, 2019 - Winner.

3. *ESC-CinC Clinical Needs Translational Award* "T-Wave Morphology Changes as Surrogate for Blood Potassium Concentration in Hemodialysis Patients." *2019 Computing in Cardiology (CinC)*, Singapore, 2019 - Winner.
4. *José Maria Ferrero Award for Ph.D. students* "Estudio de los Cambios en la Morfología de las Ondas T como Sustituto de la Concentración de Potasio en Sangre en Pacientes de Hemodiálisis". *Actas del XXXVII Congreso Anual de la Sociedad Española de Ingeniería Biomédica*, Santander, Spain, 2019 - Finalist.

- **Chapter 3:** PCA uses a maximum-variance criterion to separate signal and noise into orthogonal subspaces, which may not be the best strategy for emphasising clinical relevant information [163] such as $[K^+]$-driven TW morphology changes and, in turn, the potential clinical significance of time warping based markers could be affected. In this chapter, a different lead space reduction technique, named periodic component analysis (πCA), is proposed and tested against PCA-based approach. To perform a thorough and detailed evaluation of the proposed methodology, PCA- and πCA-based time warping markers are extracted in three different specific and supervised scenarios: (i) only $[K^+]$ induced TW variations (ii) controlled postural changes with no concurrent $[K^+]$ variations and (iii) controlled simulation scenario with different noise sources and SNR. The chapter concludes by presenting and comparing the performance in the three scenarios of the proposed πCA with respect to PCA, and then discussing the improvements in clinical terms derived by using πCA-based time warping markers.

  The research described in this chapter generated the following publications:

  1. **F. Palmieri**, P. Gomis, J. E. Ruiz, D. Ferreira, A. Martín-Yebra, E. Pueyo, J. P. Martínez, J. Ramírez and P. Laguna. "ECG-based monitoring of blood potassium concentration: Periodic versus principal component as lead transformation for biomarker robustness" *Biomedical Signal Processing and Control*, vol. 68, Art. no. 102719, 2021, doi: 10.1016/j.bspc.2021.102719.
  2. **F. Palmieri**, P. Gomis, J. E. Ruiz, D. Ferreira, A. Martín-Yebra, E. Pueyo, P. Laguna, J. P. Martínez and J. Ramírez. "Potassium Monitoring From Multilead T-wave Morphology Changes During Hemodyalisis: Periodic Versus Principal Component Analysis." *2020 Computing in Cardiology*, Rimini, Italy, 2020, pp. 1-4, 2020, doi: 10.22489/CinC.2020.199.
  3. **F. Palmieri**, P. Gomis, J. E. Ruiz, D. Ferreira, A. Martín-Yebra, E. Pueyo, P. Laguna, J. P. Martínez and J. Ramírez. "Monitorización en diálisis de la concentración de potasio en sangre mediante los cambios en la morfología multi-lead de la onda T: comparación entre usar la transformación en componentes periódicas y principales". *Actas del XXXVIII Congreso Anual de la Sociedad Española de Ingeniería Biomédica*, Valladolid, Spain, 2020, pp. 434-437, ISBN 978-84-09-25491-0.

- **Chapter 4:** Whereas chapters 2 and 3 focus on the relation between time warping markers and $[K^+]$, in chapter 4 regression models for $\Delta[K^+]$ estimation from the proposed markers are presented. For this purpose, different patient-specific polynomial (i.e. linear, quadratic and cubic) regression models are computed and the accuracy of the model-estimated $\Delta[K^+]$ values are compared with respect to the real measured by blood sample test. Finally, the performance of both quadratic and cubic regression models compared to the linear ones, and the improvement achieved by using the quadratic models are discussed.

  The research described in this chapter generated the following publications:

  1. **F. Palmieri**, P. Gomis, J. E. Ruiz, D. Ferreira, A. Martín-Yebra, E. Pueyo, J. P. Martínez, J. Ramírez and P. Laguna. "Nonlinear T-Wave Time Warping-Based Sensing Model for Non-Invasive Personalised Blood Potassium Monitoring in Hemodialysis Patients: A Pilot Study" *Sensors*, vol. 21, no. 8, Art. no. 2710, 2021, doi: 10.3390/s21082710.

- **Chapter 5:** The presence of TW onset and end point misplacement, consequence of automatic ECG delineation errors, may greatly affect the morphology of a TW by introducing information not related to the ventricular repolarization, and thus reducing the diagnostic reliability of the proposed TW time warping markers. Under the assumption that a weighting stage could reduce the undesired effects of TW boundaries delineation errors, two weighting functions (WFs) are tested for

the computation of time warping markers. According to the results, not only the proposed WFs can enhance the robustness against TW delineation errors, but also their use can improve the SCD risk stratification power of TW time warping analysis derived indexes.

The research described in this chapter generated the following publications:

1. **F. Palmieri**, P. Gomis, J. E. Ruiz, D. Ferreira, E. Pueyo, J. P. Martínez, P. Laguna, and J. Ramírez. "Weighted Time Warping T-wave Analysis Robust to Delineation Errors: Clinical Implications". *2021 Computing in Cardiology (CinC)*, Brno, Czech Republic, vol. 48, pp. 1-4, 2021, doi: 10.23919/CinC53138.2021.9662738.
2. **F. Palmieri**, P. Gomis, J. E. Ruiz, D. Ferreira, E. Pueyo, J. P. Martínez, P. Laguna, and J. Ramírez. " "Time warping" ponderado sobre la onda T para Reducir el Impacto de Errores de Delineación: Implicaciones Clínicas". *Actas del XXXIX Congreso Anual de la Sociedad Española de Ingeniería Biomédica*, Spain, 2021, pp.94-98 ISBN 978-84-09-36054-3.

The following manuscript has been submitted with the results presented in this chapter:

1. **F. Palmieri**, P. Gomis, D. Ferreira, E. Pueyo, J. P. Martínez, P. Laguna, and J. Ramírez. "Weighted Time Warping Improves T-wave Morphology Markers Clinical Significance". *IEEE Transactions on Biomedical Engineering*, doi: 10.1109/TBME.2022.3153791, 2022.

- **Chapter 6:** It summarises the main conclusions of the thesis and presents new lines of research that could be undertaken in future studies.

1.7 Collaborations and research stay

All the research presented in this dissertation was conducted within the joint Ph.D. program in biomedical engineering at both Universitat Politècnica de Catalunya (Barcelona, Spain) and at the Biomedical Signal Interpretation & Computational Simulation (BSICoS) group at University of Zaragoza (Zaragoza, Spain), under the supervision of Professor Pablo Laguna and Professor Pedro Gomis. Moreover, the majority of the studies were performed in collaboration with researchers and clinicians belonging to other research groups and institutions, who actively collaborated with methodological, physiological and data collection and interpretation:

- Dr Julia Ramírez
  William Harvey Research Institute, Queen Mary University of London, London, UK.
- Dr José Esteban Ruiz
  Nephrology Ward, Hospital Clínico Universitario Lozano Blesa, Zaragoza, Spain.
- Dr Beatriz Bergasa
  Nephrology Ward, Hospital Clínico Universitario Lozano Blesa, Zaragoza, Spain.
- Dina Ferreira
  Laboratorios Rubio S.A. Castellbisbal, Barcelona, Spain.

Additionally, I had the opportunity to benefit from a research stay in the context of my Ph.D. from January 2020 to March 2020 at William Harvey Research Institute, Queen Mary University of London, London, UK under the supervision of Prof Patricia B. Munroe and Dr Julia Ramírez.
This stay was an opportunity to discuss closely with Dr Julia Ramírez, who developed the TW time warping analysis methodology, in the context of the application of that methodology to monitor $[K^+]$ in ESRD patients undergoing HD and possible modifications. In addition, I familiarised with genetic analyses and bioinformatics applications to understand the biology underlying cardiovascular risk factors.

CHAPTER

2

T wave Morphology Analysis for Blood Potassium Concentration Tracking

2.1 Introduction

As introduced in chapter 1, $[K^+]$ outside the physiological interval are associated with increased mortality risk [8]. In healthy conditions, the maintenance of $[K^+]$ homeostasis is ensured by normal renal activity [164]. However, ESRD patients undergoing HD suffer from $[K^+]$ imbalance, leading to a high incidence of arrhythmic events [165].

As explained in section 1.4.3, alterations in ECG patterns are known to be directly associated with $[K^+]$. In particular, TW related features are extensively used index to monitoring dyskalemic patients, and different markers have been previously reported to be correlated with $[K^+]$, see section 1.5. However, these markers rely on specific local features of the TW rather than in the overall TW morphology, which we hypothesise may have a stronger potential in following $[K^+]$ variations resulting in markers with higher clinical significance.

The time warping analysis, described in section 2.3.4, was proposed for the quantification of changes in the overall TW morphology. In this chapter, six indices are investigated, d_w^u and d_a, reflecting morphological variations in time and amplitude, respectively, as well as their non-linear version, d_w^{NL} and d_a^{NL} as reported in [166] and two novel markers derived from d_w^u and named d_w and $d_{w,c}$.

The main goal of this chapter is to evaluate the potential use of these markers in monitoring both hypo- and hyperkalemia events excluding the variability due to the HR and to compare their performance against two well-known TW-based markers: the width of the TW (T_w) [134], the TW slope-to-amplitude ratio ($T_{S/A}$) [141] in standard single-lead approach and by applying principal component analysis (PCA) as multilead space reduction technique.

2.2 Materials: DEKOALE dataset

The "**DE**tection of [$\mathbf{K}^+$] c**O**ncentration **AL**terations from the **E**CG (DEKOALE)" dataset was compiled at the Nephrology ward from Hospital Clínico Universitario Lozano Blesa (Zaragoza, Spain) [167]. The study population included 29 ESRD patients undergoing HD. Inclusion criteria were (i) 18-year-old (or older), (ii) having a diagnosed ESRD pathology and (iii) undergoing HD, regardless if conventional, online or Acetate-free biofiltration (AFB), at least three times per week (with venous or cannula access). Table 2.1 shows the population characteristics. The study protocol was approved by the ethics committee of the Aragon research centre (ref. PI18/003, 10/04/2019) and all patients and/or their legal guardians signed informed consent. All the procedures were performed in accordance with the Helsinki Declaration. The database collection is still ongoing.

Table 2.1: Clinical features of the DEKOALE study population. Values are expressed as number (%) for categorical variables, and median (IQR) for continuous variables.

	(N = 29)
Age (years)	75 (12)
Gender (male)	20 (70%)
Anti-arrhythmic drugs (yes)	9 (31%)
Implanted pace-maker (yes)	1 (3%)
Time under HD treatment (months)	15 (59)
HD session duration	
210 min	3 (10%)
240 min	26 (90%)
Kidney disease etiology	
Diabetes mellitus	17 (59%)
Interstitial nephritis	2 (7%)
Glomerulonephritis	2 (7%)
Tuberous sclerosis	1 (3%)
Polycystic kidney	1 (3%)
Cancer	1 (3%)
Unknown	5 (18%)
HD liquid composition	
Potassium (1.5 mmol/L)	21 (72%)
Potassium (3 mmol/L)	5 (17%)
Potassium (decreasing)	3 (11%)
Calcium (2.5 mg/dL)	21 (72%)
Calcium (3 mg/dL)	8 (28%)
HD techniques	
Conventional	18 (62%)
Online	8 (28%)
AFB with decreasing intra-HD [K^+]	3 (10%)

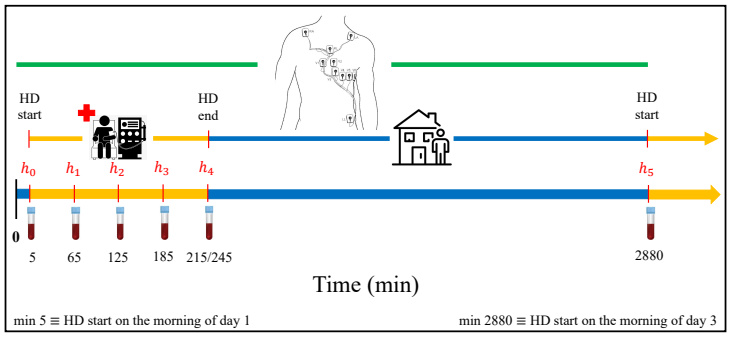

Figure 2.1: Diagram of the DEKOALE study protocol: h_0 to h_5 are the time points (in minutes) for blood sample extraction. h_4 is taken at the end of the HD (minute 215-th or 245-th, depending on the HD duration).

Table 2.2: Blood potassium concentration [K^+] in (mmol/L) patients in the DEKOALE dataset at each blood test. Values are expressed as median (IQR).

	h_0	h_1	h_2	h_3	h_4	h_5
[K^+]	5.00 (1.36)	3.85 (1.08)	3.64 (0.84)	3.39 (0.74)	3.30 (0.62)	4.80 (1.56)

2.2.1 General information

Sex, age, concomitant therapies (e.g. assumption of anti-arrhythmic drugs), kidney disease etiology and HD treatment related information were collected for each enrolled patient, as detailed in Table 2.1.

2.2.2 Blood sample analysis

For each patient, six blood samples were taken and analysed during the HD session: the first one at the HD onset and the next three, every subsequent hour (Figure 2.1, h_0 to h_3 in red). The 5-th blood sample was collected at the end of the HD (minute 215-th or 245-th, depending on the HD session duration) while the 6-th blood sample was taken after 48 hours, immediately before the next HD session. Potassium, magnesium, calcium, urea, creatinine, bicarbonate and pH were measured from each blood test. Blood potassium concentrations values for each blood test are given in Table 2.2.

2.2.3 ECG measurements

A 48h, standard 12-lead ECG Holter recording, (H12+, Mortara Instruments, Milwaukee, WI, USA, sampling frequency of 1 kHz, amplitude resolution of 3.75 μV), was obtained for each enrolled patient, starting the acquisition 5 minutes before the HD onset (Figure 2.1, green line). As an example, an excerpt of a real ECG is depicted in Figure 2.2a.

2.3 Methods

2.3.1 ECG preprocessing

The objective of the preprocessing is to minimize the contamination by noise and artifacts in the signal, and to prepare it for posterior stages. This topic has been widely investigated being an essential step in any ECG processing system. An overview on preprocessing procedures can be found in [53]. The preprocessing following described was restricted to the procedures applied in this work and it was performed by using custom-built MATLAB software.

To ensure a proper ECG waveform analysis, an initial filtration was done to improve the signal-to-noise ratio (SNR). This step included the removal of both baseline wander and high frequency noises, and an example is provided in Figure 2.2b.

Baseline wander

The baseline wander is an external, narrow band low-frequency component in the ECG which may interfere with the signal analysis, and may result from a variety of noise sources including respiration, body movements, and poor electrode contact. As reported in [168], baseline wander filtration can be performed at a lower sampling frequency than at the actual one of the original ECG signal. The main steps of this approach are: (1) decimation of the original signal, which includes antialiasing filtering, to a lower sampling rate better suited to filtering, (2) low-pass filtering to produce an estimate of the baseline wander, (3) interpolation of the estimate back to the original sampling rate, and (4) subtraction of the estimate from the original ECG so as to produce the baseline-corrected signal. The advantage of the sampling rate alteration technique is twofold: it offers low complexity, and it can easily accommodate a time-variable cut-off frequency [168].

High frequency noises

Electromagnetic fields caused by a powerline represent a common noise source in the ECG that is characterized by 50 or 60 Hz sinusoidal interference, possibly accompanied by a number of harmonics. Such noise increases the difficulty in analysising and interpreting the ECG, since the delineation of low-amplitude waveforms becomes unreliable [168]. Muscle activity is another important filtering issue

because of the substantial spectral overlap between the ECG and muscle noise [168].
To remove powerline noise and to reduce the muscle noise, but still allow QRS detection, a 6-th order low-pass Butterworth filter with 40 Hz cut-off frequency was applied.

2.3.2 ECG waveform detection and delineation

After the filtration step, the QRS complex detection and the delineation of each heartbeat at each available lead, was performed with a wavelet-based delineator described in Martínez *et al* [169]. The wavelet transform (WT) decomposes the signal in the time-scale domain, allowing its representation at different resolutions. It is, therefore, a suitable tool to analyse ECG signals, which contain patterns with different frequency content (QRS complexes, P and T-waves).

Single-lead delineation

The discrete dyadic WT [169] is implemented in such a way that it keeps temporal resolution at different scales. The detection of the fiducial points is carried out across the adequate WT scales, attending to the dominant frequency components of each ECG wave: Q,R,S waves correspond to a simultaneous effect in scales 2^1–2^2, while the T and P waves affect mainly scales 2^4 or 2^5 [169]. ECG wave peaks correspond to zero crossings in the WT, and ECG maximum slopes correspond to WT's maxima and minima. Depending on the number and polarity of the slopes found, a wave morphology is assigned and boundaries are located using threshold-based criteria. The onset (end) of a wave occurs before (after) the first (last) significant slope associated with the wave [169].

In this study, TWs delineated from leads V3 to V6, as used in a previous study [145] for $[K^+]$ estimation, and lead II being the most widely used in patient monitoring [170] were analysed.

Selection rules for multi-lead delineation

To obtain multilead peak locations, a median post-processing selection rule over the single-lead-based detected locations is used. The post-processing rules for boundaries consist of ordering the single-lead annotations and selecting as the onset (end) of a wave the first (last) annotation whose k nearest neighbours lay within a δ ms interval [169, 171]. An example of the ECG with the delineation marks for both the QRS complex and the TW is shown in Figure 2.2b.

2.3.3 Spatial lead reduction by principal component analysis

A lead space reduction (LSR) by PCA was performed being this a robust spatial transformation emphasizing waveform SNR [172]. Here, PCA was spatially applied to the 8 independent leads, learned over the TW segment to mainly accentuate this waveform, and resulting in 8 principal components (PCs) or transformed leads (TLs). The coefficients defining the PCA transformation were obtained from the eigenvectors of the 8×8 interlead auto-correlation matrix computed over the TWs in a 10-min wide window at the end of the HD session. The correct delineation of TWs is crucial to emphasize only TW energy content. A segment of the 8 PCs extracted from ECG in Figure 2.2b is depicted in Figure 2.2c.

The first PC, denoted as PC1, was used for the subsequent ECG analysis, as it is the transformed lead where the TWs have maximal energy, and thus, maximal SNR for morphological characterisation [172]. PC1 was further delineated by applying the same delineator described in section 2.3.2, and each TW was further low-pass filtered at 20 Hz to restrict shape analysis to the dominant band of the TW so removing remaining noisy components that could still corrupt the TW shape analysis.

2.3.4 Time warping analysis

Spatial dispersion of ventricular repolarization is a property of the human heart and it is responsible for the genesis of the TW on the ECG [173]. However, an amplification of such dispersion creates suitable conditions for the mechanism of reentry and favours the development of ventricular tachycardia/fibrillation

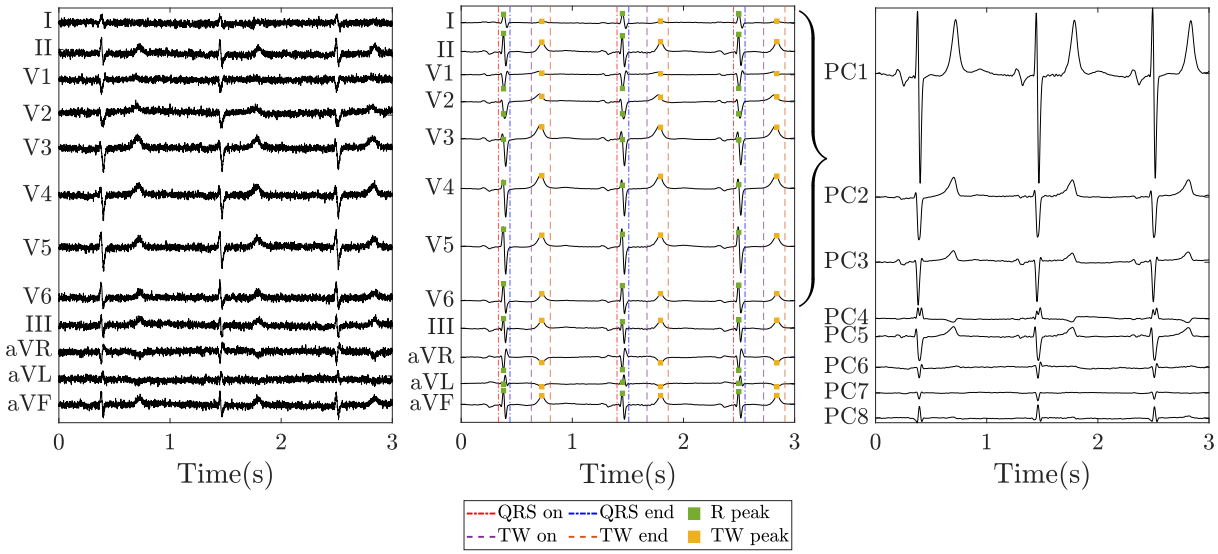

Figure 2.2: Representative diagram of the preprocessing and transformation used to obtain PCs from the standard 12-lead ECG signal. In panel (a), a 5 second long of a real ECG signal is depicted. Panel (b) shows the same excerpt after preforming the pre-processing described in section 2.3.1. In addition, the delineation marks for the QRS complex (being the red and the blue dashed-dot lines the QRS on and QRS end points respectively and the green square the R peak position) and TW (being the magenta and the orange dash line the TW on and TW end points respectively and the yellow square the TW peak position), obtained as reported in section 2.3.2, are displayed. In panel (c) shows the transformed orthogonal leads obtained from the PCA technique performed over the 8 independent leads (see section 2.3.3).

[174, 175], which could potentially lead to SCD [176]. Therefore, detection and prevention of arrhythmic events are the main strategies to decrease SCD outcomes [177].

Since the TW on the ECG reflects the spatio-temporal dispersion of repolarization times of the ventricular myocites [178], several metrics related to TW morphology (such as amplitude [173], width [179], nondipolar components [180], notches or asymmetries [147, 181–183]) and duration (like QT dispersion [184] and T_{apex}–T_{end} [185, 186]) have been proposed to quantify repolarization heterogeneity. Among them, one of the most recently proposed is based on the TW time warping analysis [166] a method, this, which allows to quantify linear and non-linear variations of the TW width and amplitude due to homogeneous increments of this dispersion. The methodology used in this work has been adapted from the mathematical framework presented by Ramírez *et al.* [166].

To illustrate the process of TW morphology comparison, consider two TWs and let call them reference, $\boldsymbol{f}^r(\boldsymbol{t}^r) = [f^r(t^r(1)),...,f^r(t^r(N_r))]^\top$, and studied, $\boldsymbol{f}^s(\boldsymbol{t}^s) = [f^s(t^s(1)),...,f^s(t^s(N_s))]^\top$, where $\boldsymbol{t}^r = [t^r(1),...,t^r(N_r)]^\top$ and $\boldsymbol{t}^s = [t^s(1),...,t^s(N_s)]^\top$ and N_r and N_s being the total duration of $\boldsymbol{t}^r$ and $\boldsymbol{t}^s$, respectively, as illustrated in Figure 2.3a. We take $\boldsymbol{f}^r(\boldsymbol{t}^r)$ as the reference TW and $\boldsymbol{f}^s(\boldsymbol{t}^s)$ as the TW to be compared with respect to $\boldsymbol{f}^r(\boldsymbol{t}^r)$. Both $\boldsymbol{f}^r(\boldsymbol{t}^r)$ and $\boldsymbol{f}^s(\boldsymbol{t}^s)$ are aligned with respect to their centre of gravity, so that only morphology changes, and not those associated with their relative delay, were quantified by the warping algorithm.

Let $\gamma(\boldsymbol{t}^r)$ be the warping function that relates $\boldsymbol{t}^r$ and $\boldsymbol{t}^s$, such that the composition $[\boldsymbol{f}^s \circ \gamma](\boldsymbol{t}^r) = \boldsymbol{f}^s(\gamma(\boldsymbol{t}^r))$ denotes the re-parameterization or time domain warping of $\boldsymbol{f}^s(\boldsymbol{t}^s)$ using $\gamma(\boldsymbol{t}^r)$. To avoid the so called "pinching effect" [187], the square-root slope function (SRSF) was proposed [188, 189] for warping in a well-defined geometrical space, defined as the square-root of the derivative of $\boldsymbol{f}(\boldsymbol{t})$, considering the sign:

$$\boldsymbol{q}_f(\boldsymbol{t}) = \text{sign}\left(\dot{\boldsymbol{f}}(\boldsymbol{t})\right)\sqrt{\left|\dot{\boldsymbol{f}}(\boldsymbol{t})\right|} \tag{2.1}$$

The SRSF of $\boldsymbol{f}^r(\boldsymbol{t}^r)$ and $\boldsymbol{f}^s(\boldsymbol{t}^s)$, $\boldsymbol{q}_{f^r}(\boldsymbol{t}^r)$ and $\boldsymbol{q}_{f^s}(\boldsymbol{t}^s)$, respectively, are shown in Figure 2.3b. The optimal warping function is the one that minimizes the amplitude difference between the SRSF of $\boldsymbol{f}^r(\boldsymbol{t}^r)$ and $\boldsymbol{f}^s(\boldsymbol{\gamma}(\boldsymbol{t}^r))$, $\boldsymbol{q}_{f^r}(\boldsymbol{t}^r)$ and $\boldsymbol{q}_{[f^s\circ\gamma]}(\boldsymbol{t}^r) = \boldsymbol{q}_{f^s}(\boldsymbol{\gamma}(\boldsymbol{t}^r))\sqrt{\dot{\boldsymbol{\gamma}}(\boldsymbol{t}^r)}$, respectively [188, 189]:

$$\begin{aligned}\gamma^*(\boldsymbol{t}^r) &= \underset{\gamma(\boldsymbol{t}^r)}{\arg\min}\left(\left\|\boldsymbol{q}_{f^r}(\boldsymbol{t}^r) - \boldsymbol{q}_{[f^s\circ\gamma]}(\boldsymbol{t}^r)\right\|\right) \\ &= \underset{\gamma(\boldsymbol{t}^r)}{\arg\min}\left(\left\|\boldsymbol{q}_{f^r}(\boldsymbol{t}^r) - \boldsymbol{q}_{f^s}(\gamma(\boldsymbol{t}^r))\sqrt{\dot{\gamma}(\boldsymbol{t}^r)}\right\|\right)\end{aligned} \tag{2.2}$$

The optimal warping function, $\boldsymbol{\gamma}^*(\boldsymbol{t}^r)$, that optimally warps $\boldsymbol{f}^r(\boldsymbol{t}^r)$ and $\boldsymbol{f}^s(\boldsymbol{t}^s)$ is shown in Figure 2.3c. The warped T-wave, $\boldsymbol{f}^s(\boldsymbol{\gamma}^*(\boldsymbol{t}^r))$ is shown in Figure 2.3e, together with the reference T-wave, $\boldsymbol{f}^r(\boldsymbol{t}^r)$, while their corresponding SRSFs are shown in Figure 2.3d.

The dynamic programming algorithm, as described in [166], was used to obtain the solution of this optimization [190].

2.3.5 Unsigned time warping parameter

The level of warping may be different under various situations and it reflects important information regarding time domain variability. We define a metric, d_w^u (corresponding to the index denoted as d_w in [166]), shown as the orange area in Figure 2.3c, that quantifies the level of warping needed to optimally align any two TWs as the average of the absolute difference value between $\boldsymbol{\gamma}^*(\boldsymbol{t}^r)$ and $\boldsymbol{t}^r$:

$$d_w^u = \frac{1}{N_r}\sum_{n=1}^{N_r}\left|\gamma^*(t^r(n)) - t^r(n)\right|, \tag{2.3}$$

If $\boldsymbol{\gamma}^*(\boldsymbol{t}^r) = \boldsymbol{t}^r$, then the functions are perfectly aligned, so it makes sense to use the difference between $\boldsymbol{\gamma}^*(\boldsymbol{t}^r)$ and $\boldsymbol{t}^r$ to quantify the variability between each TW time domain.

Once the time domain variability has been compensated for by optimally warping $\boldsymbol{f}^s(\boldsymbol{t}^s)$, the remaining variability is merely amplitude variability, as shown in Figure 2.3e. Therefore, the amplitude difference between $\boldsymbol{f}^r(\boldsymbol{t}^r)$ and $\boldsymbol{f}^s(\boldsymbol{\gamma}^*(\boldsymbol{t}^r))$, i.e. the variability between $\boldsymbol{f}^r(\boldsymbol{t}^r)$ and $\boldsymbol{f}^s(\boldsymbol{t}^s)$ not due to deviations in the time domain, is quantified as the area contained between $\boldsymbol{f}^r(\boldsymbol{t}^r)$ and $\boldsymbol{f}^s(\boldsymbol{\gamma}^*(\boldsymbol{t}^r))$, normalized by the L2-norm of $\boldsymbol{f}^r(\boldsymbol{t}^r)$:

$$d_a = \frac{e_a}{\|e_a\|}\cdot\frac{\|\boldsymbol{f}^s(\boldsymbol{\gamma}^*(\boldsymbol{t}^r)) - \boldsymbol{f}^r(\boldsymbol{t}^r)\|}{\|\boldsymbol{f}^r(\boldsymbol{t}^r)\|}\times 100, \tag{2.4}$$

where $\frac{e_a}{\|e_a\|}, e_a = \sum_{n=1}^{N_r}(f^s(\gamma^*(t^r)) - f^r(t^r))$, accounts for the sign.

The proposed markers, d_w^u and d_a, contain information about linear and non-linear differences in both time and amplitude, respectively. Isolating the strictly non-linear variability information might provide additional understanding on the different sources generating the morphology of the T-wave.

Figure 2.4a shows the optimal warping function from Figure 2.3c. As explained in eq. (2.3), the marker d_w^u is calculated as the mean deviation of $\boldsymbol{\gamma}^*(\boldsymbol{t}^r)$ from $\boldsymbol{t}^r$, marked in orange in Figure 2.4a. By fitting $\boldsymbol{\gamma}^*(\boldsymbol{t}^r)$ with a linear regression, $\boldsymbol{\gamma}_l^*(\boldsymbol{t}^r)$ (green line), and measuring the mean deviation of $\boldsymbol{\gamma}^*(\boldsymbol{t}^r)$ with respect to this regression, we can have a quantification of the level of non-linear warping (dashed black region). This can be expressed as:

$$d_w^{\mathrm{NL}} = \frac{1}{N_r}\sum_{n=1}^{N_r}\left|\gamma^*(t^r(n)) - \gamma_l^*(t^r(n))\right|, \tag{2.5}$$

where $\boldsymbol{\gamma}_l^*(\boldsymbol{t}^r)$ is the linear fitting of $\boldsymbol{\gamma}^*(\boldsymbol{t}^r)$ using the least absolute residual method [191] (Figure 2.4a). The linear warping can be quantified by measuring the mean deviation of $\boldsymbol{\gamma}_l^*(\boldsymbol{t}^r)$ from $\boldsymbol{t}^r$ (non-dashed region in Figure 2.4a).

Regarding d_a, normalizing the warped TWs, we can quantify non-linear amplitude differences not due to homogeneous scaling, and possibly caused by heterogeneous dispersion of repolarization times:

$$d_a^{\mathrm{NL}} = \left\|\frac{\boldsymbol{f}^r(\boldsymbol{t}^r)}{\|\boldsymbol{f}^r(\boldsymbol{t}^r)\|} - \frac{\boldsymbol{f}^s(\boldsymbol{\gamma}^*(\boldsymbol{t}^r))}{\|\boldsymbol{f}^s(\boldsymbol{\gamma}^*(\boldsymbol{t}^r))\|}\right\|\times 100. \tag{2.6}$$

This is depicted in Figure 2.4b and 2.4c. Panel (b) shows the reference, $\boldsymbol{f}^r(\boldsymbol{t}^r)$ (solid blue), and studied, $\boldsymbol{f}^s(\boldsymbol{t}^s)$ (solid red), TWs with only amplitude variability (we assumed $\boldsymbol{\gamma}^*(\boldsymbol{t}^r) = \boldsymbol{t}^r$ in this example for clarity). Panel (c) shows the remaining non-linear amplitude variability after normalization.

2.3.6 Signed time warping parameters

In this thesis, two different versions of the d_w^u markers were also implemented to define the direction of the warping (i.e. if the studied TW has to be enlarged or shrunken in order to fit the reference one) and to solve the dependency of the TW with the HR.

The original definition of d_w^u eq. (2.3), was modified here to allow the marker to be signed, therefore distinguishing TW widening from narrowing. This signed d_w was proposed in [167] and defined as:

$$d_w = \left(\frac{s_d}{|s_d|}\right)\frac{1}{N_r}\sum_{n=1}^{N_r}|\gamma^*\left(t^r\left(n\right)\right)-t^r\left(n\right)| \tag{2.7}$$

where s_d was used to account for the sign of the d_w and it was computed as:

$$s_d = \sum_{n\in N_r^u}\left(\gamma^*\left(t^r\left(n\right)\right)-t^r\left(n\right)\right)+\sum_{n\notin N_r^u}\left(t^r\left(n\right)-\gamma^*\left(t^r\left(n\right)\right)\right) \tag{2.8}$$

with N_r^u being the set of TW up-slope samples. A positive sign means that the $\boldsymbol{f}^s(\boldsymbol{t}^s)$ has to be widened to fit the $\boldsymbol{f}^r(\boldsymbol{t}^r)$ and vice-versa for a negative sign.

2.3.7 Heart-rate-corrected TW warping marker

It is well known that TW duration and QT interval are strongly dependent on HR [192]. Although aligning the TWs according to their gravity centre reduces most of the dependence of d_w on HR, there may still be some residual dependence in TW morphology that should be compensated for. For that purpose, d_w, as originally proposed in eq. (2.7), was assumed to be modelled as the sum of two components:

$$d_w = d_{w,c} + d_{w,\mathrm{HR}} \tag{2.9}$$

where $d_{w,\mathrm{HR}}$ is the HR dependent component and $d_{w,c}$ is the non-HR dependent component accounting for $[K^+]$ induced variations and possibly others not HR-related.

To estimate the component $d_{w,c}$ of interest, we depart from the literature, where several formulae for HR-dependency correction of repolarization related time intervals, like the QT interval, have been developed [193–196], including a variety of approaches (e.g. linear, hyperbolic, exponential models etc.) being investigated and tested in view of the complex relationship between QT interval and HR [195]. To derive a correction formula and estimate $d_{w,c}$, we started from a linear approximation of a hyperbolic model under small RR changes, derived similarly to the QT interval correction (QTc) [194, 195],

$$QT = \beta(\mathrm{RR})^{\alpha} \tag{2.10}$$

Let's call RR_r the reference RR interval associated to the reference TW and RR_i the one to the i-th RR interval from one beat at the i-th segment, then

$$QT_i - QT_r = \beta\Big((\mathrm{RR}_i)^{\alpha} - (\mathrm{RR}_r)^{\alpha}\Big). \tag{2.11}$$

As the $QT_i - QT_r$ difference, also $d_w(i)$ is a measure of width change between the reference r and the current i-th mean TWs from their respective observations time windows, then it is possible to extend previous relation in eq. (2.11) to $d_w(i)$ obtaining the HR related component

$$d_{w,\mathrm{HR}}(i) = \beta\Big((\mathrm{RR}_i)^{\alpha} - (\mathrm{RR}_r)^{\alpha}\Big). \tag{2.12}$$

By substituting eq. (2.12) in eq. (2.9) we obtain:

$$d_w(i) = d_{w,c}(i) + \beta\Big((\mathrm{RR}_i)^{\alpha} - (\mathrm{RR}_r)^{\alpha}\Big). \tag{2.13}$$

The value $d_{w,c}(i)$ can be assumed to be non-zero mean, and uncorrelated to HR, that is:

$$d_{w,c}(i) = b + \Delta d_{w,c}(i), \tag{2.14}$$

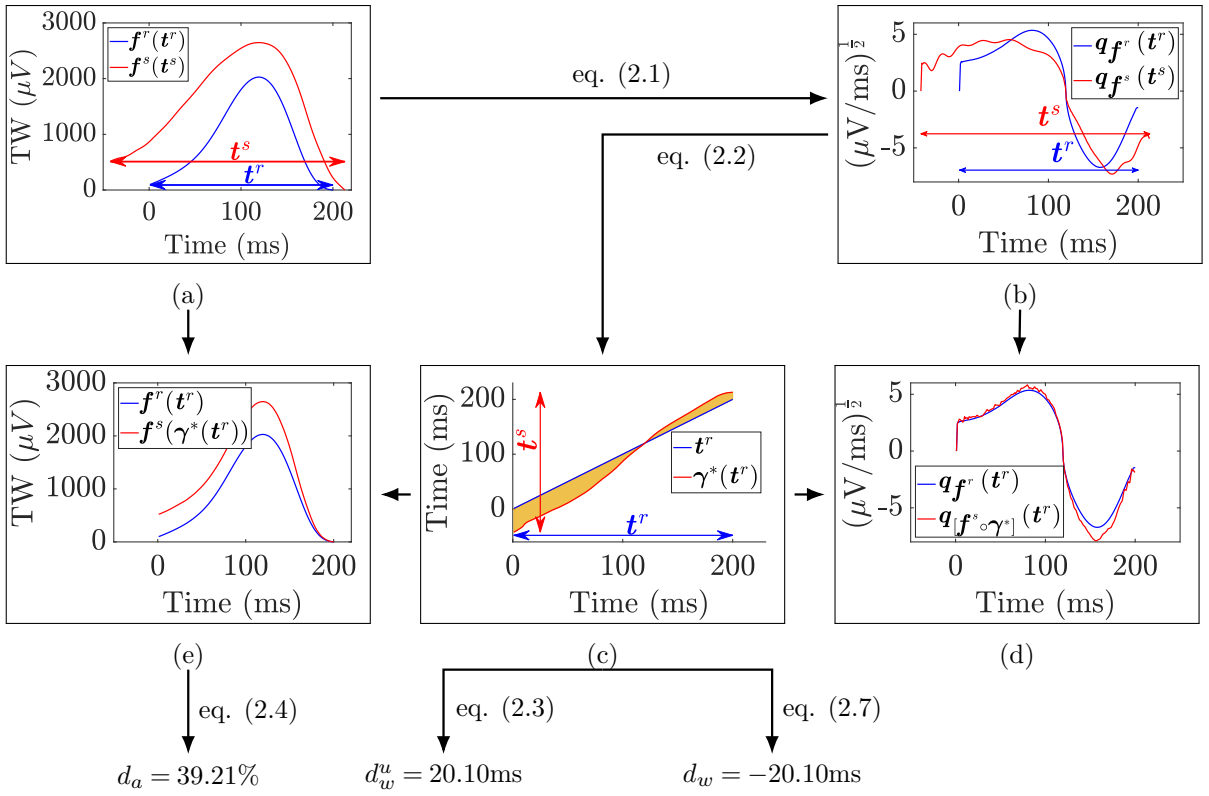

Figure 2.3: Flow diagram illustrating the computation of linear warping and amplitude markers d_w^u, d_w and d_a. Panel (a) shows the reference TW (solid blue) and the one, referred to as TW study, whose morphology is wanted to be compared having longer duration and larger magnitude (solid red). (b) Their respective square-root slope functions are obtained by applying eq. (2.1). (c) Optimizing eq. (2.2) with the "Dynamic Programming" algorithm [166], the warping function that optimally relates $\boldsymbol{t}^r$ and $\boldsymbol{t}^s$, $\boldsymbol{\gamma}^*(\boldsymbol{t}^r)$, is computed. (e) The re-parameterization of $\boldsymbol{f}^s(\boldsymbol{t}^s)$ using $\boldsymbol{\gamma}^*(\boldsymbol{t}^r)$ leads to $[\boldsymbol{f}^s \circ \boldsymbol{\gamma}^*](\boldsymbol{t}^r)$, the warped TW with no remaining time domain variability, and only presenting amplitude variability. (d) Square-root slope functions of the reference (solid blue) and warped (dashed red) TWs.

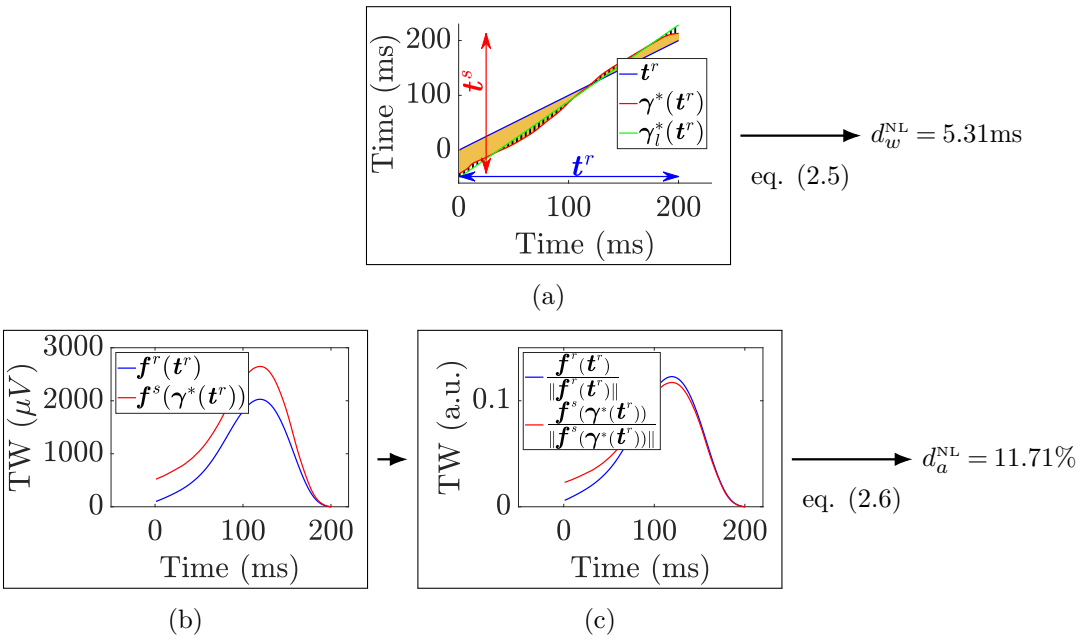

Figure 2.4: Calculation of the non-linear warping and amplitude information. In panel (a), the area between $\boldsymbol{\gamma}^*(\boldsymbol{t}^r)$ and $\boldsymbol{t}^r$ (orange region) represents the total warping information, quantified by d_w^u, while the area between $\boldsymbol{\gamma}^*(\boldsymbol{t}^r)$ and $\boldsymbol{\gamma}_l^*(\boldsymbol{t}^r)$ represents the non-linear warping information (dashed black region), quantified by d_w^{NL}. In panel (b) are the reference, $\boldsymbol{f}^r(\boldsymbol{t}^r)$ (solid blue), and the studied, $\boldsymbol{f}^s(\boldsymbol{t}^s)$ (solid red), TWs with only amplitude variability ($\boldsymbol{\gamma}^*(\boldsymbol{t}^r) = \boldsymbol{t}^r$). Panel (c) shows both the normalized reference, $\frac{\boldsymbol{f}^r(\boldsymbol{t}^r)}{\|\boldsymbol{f}^r(\boldsymbol{t}^r)\|}$, and the studied, $\frac{\boldsymbol{f}^s(\boldsymbol{\gamma}^*(\boldsymbol{t}^r))}{\|\boldsymbol{f}^s(\boldsymbol{\gamma}^*(\boldsymbol{t}^r))\|}$, TWs.

with $\Delta d_{w,c}(i)$ zero mean and uncorrelated to HR. Then, $d_w(i)$ becomes:

$$d_w(i) = b + \Delta d_{w,c}(i) + \beta\Big((\mathrm{RR}_i)^\alpha - (\mathrm{RR}_r)^\alpha\Big), \tag{2.15}$$

where the parameters b, β and α, once jointly estimated (i.e. $\hat{b}$, $\hat{\beta}$ and $\hat{\alpha}$) can be used to derive $\hat{d}_{w,c}(i)$ as:

$$\hat{d}_{w,c}(i) = d_w(i) - \hat{\beta}\Big((\mathrm{RR}_i)^{\hat{\alpha}} - (\mathrm{RR}_r)^{\hat{\alpha}}\Big) \tag{2.16}$$

Note that, $\hat{\beta}$ and $\hat{\alpha}$ cannot be assessed from eq. (2.15) with a directly least square fitting, since the DC component b in eq. (2.15) largely affects the results. Rather, it is possible to jointly estimate $\hat{b}, \hat{\beta}$ and $\hat{\alpha}$, and then use the results in eq. (2.16).
This estimate can be further approximated linearly for small RR changes. Denoting $\Delta\mathrm{RR}(i) = \mathrm{RR}_i - \mathrm{RR}_r$, RR_i can be expressed as $\mathrm{RR}_i = \mathrm{RR}_r + \Delta\mathrm{RR}(i)$ and by replacing this in the right side of eq. (2.12):

$$d_{w,\mathrm{HR}}(i) = \beta\Big((\mathrm{RR}_r + \Delta\mathrm{RR}(i))^\alpha - (\mathrm{RR}_r)^\alpha\Big) \tag{2.17}$$

Operating on the terms and under the assumption that $\Delta\mathrm{RR}(i) \ll \mathrm{RR}_r$, $\frac{\Delta\mathrm{RR}(i)}{\mathrm{RR}_r} \ll 1$ and by using the Taylor's series expansion, we have

$$(\mathrm{RR}_r + \Delta\mathrm{RR}(i))^\alpha - (\mathrm{RR}_r)^\alpha \simeq \alpha\Delta\mathrm{RR}(i)(\mathrm{RR}_r)^{(\alpha-1)}. \tag{2.18}$$

Substituting eq. (2.18) in eq. (2.13):

$$d_w(i) \simeq b + \Delta d_{w,c}(i) + \alpha\ \beta\ \Delta\mathrm{RR}(i)(\mathrm{RR}_r)^{(\alpha-1)} \tag{2.19}$$

where b, α, β and $(\mathrm{RR}_r)^{(\alpha-1)}$ are constant values; then placing:

$$\alpha\ \beta(\mathrm{RR}_r)^{(\alpha-1)} = c, \tag{2.20}$$

the actual $d_w(i)$ dependency with RR will be:

$$d_w(i) \simeq b + \Delta d_{w,c}(i) + c\ \Delta\mathrm{RR}(i). \tag{2.21}$$

From the geometrical point of view, b and c can be estimated as the zero-crossing and the slope, respectively, of the least-squares line fit to the $d_w(i)$ values (in a ΔRR vs. d_w graph). Then, the $d_w(i)$ component that does not dependent on the RR, meaning it is assumed not correlated, can assessed as:

$$\hat{d}_{w,c}(i) = d_w(i) - \hat{c}\ \Delta\mathrm{RR}(i) = d_w(i) - \hat{c}(\mathrm{RR}_i - \mathrm{RR}_r) \tag{2.22}$$

where $\hat{c}$ is the estimated slope from the Holter recording (see Figure 2.5), $\hat{d}_{w,c}(i)$ is then the corrected estimated of $d_{w,c}(i)$, with RR_i and RR_r the mean RR interval from the i-th studied segment and the reference windows respectively and $\hat{c}$ parameter is estimated for every patient during the time course of the Holter recording. When the linear approximation presented above cannot be assumed, $\hat{b}$, $\hat{\beta}$, and $\hat{\alpha}$ can be jointly estimated from the model in eq. (2.15), and use the eq. (2.16) as the corrected estimate.

2.3.8 Mean warped TW

From a set of I TWs, $\{\boldsymbol{f}_1^s(\boldsymbol{t}_1^s), \boldsymbol{f}_2^s(\boldsymbol{t}_2^s), ..., \boldsymbol{f}_I^s(\boldsymbol{t}_I^s)\}$ with temporal and amplitude variability it is possible to calculate a mean warped TW (MWTW) that is an optimal representative average both in temporal and amplitude domains. Consequently, we will iteratively search for the optimal MWTW in the SRSF domain, $\bar{\boldsymbol{q}}^k(\boldsymbol{t}^r)$, where k is the iteration, that minimizes the average of the difference between $\bar{\boldsymbol{q}}^k(\boldsymbol{t}^r)$ and each of the SRSF transformations of the set of T-waves, $\{\boldsymbol{q}_{f_1^s}(\boldsymbol{t}_1^s), \boldsymbol{q}_{f_2^s}(\boldsymbol{t}_2^s), ..., \boldsymbol{q}_{f_I^s}(\boldsymbol{t}_I^s)\}$. Therefore, we initialize $\bar{\boldsymbol{q}}^{k=1}(\boldsymbol{t}^r)$ as the average of $\{\boldsymbol{q}_{f_1^s}(\boldsymbol{t}_1^s), \boldsymbol{q}_{f_2^s}(\boldsymbol{t}_2^s), ..., \boldsymbol{q}_{f_I^s}(\boldsymbol{t}_I^s)\}$ and, then, for iteration k, we look for the optimal set of $\{\boldsymbol{\gamma}_1^{*^k}(\boldsymbol{t}^r), \boldsymbol{\gamma}_2^{*^k}(\boldsymbol{t}^r), ..., \boldsymbol{\gamma}_I^{*^k}(\boldsymbol{t}^r)\}$ that minimizes:

$$\begin{aligned} \boldsymbol{\gamma}_i^{*^k}(\boldsymbol{t}^r) &= \underset{\boldsymbol{\gamma}_i(\boldsymbol{t}^r)}{\arg\min} \left(\left\| \bar{\boldsymbol{q}}^k(\boldsymbol{t}^r) - \boldsymbol{q}_{f_i^s(\boldsymbol{\gamma}_i)}(\boldsymbol{t}^r) \right\| \right), \\ i &= 1, ..., I. \end{aligned} \tag{2.23}$$

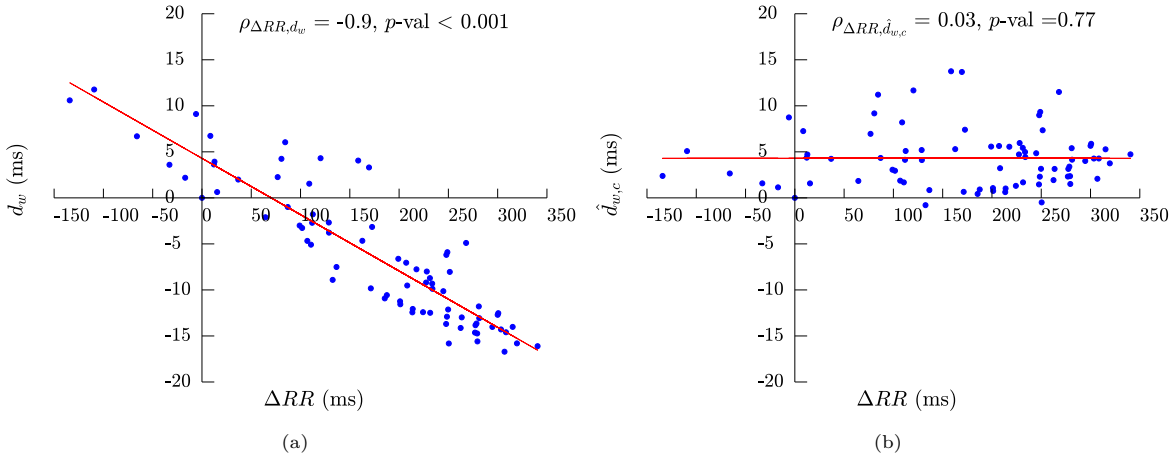

Figure 2.5: Example of the HR corrected d_w. Scatterplot showing the values of both d_w panel (a) – eq. (2.7) – and $\hat{d}_{w,c}$ panel (b) – eq. (2.22) – with respect to ΔRR for a patient undergoing HD in PCA approach. Spearman's correlation coefficients (ρ) and p-values for both d_w and $\hat{d}_{w,c}$ are shown on top of each panel, while the least-square fitting regression lines are plotted in red.

The updated SRSF transformation of the MWTW can be calculated as:

$$\bar{\boldsymbol{q}}^{k+1}(\boldsymbol{t}^r) = \frac{1}{I}\sum_{i=1}^{I} \boldsymbol{q}_{[f_i^s \circ \gamma_i^{*k}]}(\boldsymbol{t}^r) \tag{2.24}$$

We repeated eq. (2.23) and (2.24) until the difference between the energies of $\bar{\boldsymbol{q}}^{k+1}(\boldsymbol{t}^r)$ and $\bar{\boldsymbol{q}}^{k}(\boldsymbol{t}^r)$ was lower than 0.1%. Then, the final MWTW can be obtained as [188, 189]:

$$\bar{f}(t^r(n)) = \frac{1}{I}\sum_{i=1}^{I} f_i^s(t_i^s(1)) + \sum_{l=1}^{n} \bar{q}^k(t^r(l)) \left|\bar{q}^k(t^r(l))\right| \tag{2.25}$$

When the morphology of the set of TWs is very homogeneous, the morphology of the MWTW will be very similar and representative of the set. However, if the morphologies in the set are heterogeneous, like when a large portion of TWs are biphasic or S-shaped while another portion is monophasic, the MWTW morphology will resemble the dominant TW shape, in case there exists one, or the arithmetic TW mean (after warping), if the different populations have the same weight. Therefore, it would be advisable to include a pre-processing step to remove any undesired TW morphology prior the computation of the MWTW. This issue was addressed as explained in the following paragraph.

Mean warped T wave extraction in DEKOALE datset

All the TWs from the selected single leads and from PC1 were low-pass filtered at 20 Hz using a 6-th order Butterworth filter to remove remaining out-of-band frequency components. Then, two-minute ECG segments, centred on the 5-th and 35-th minutes of each available hour, were analysed. The window duration was short enough to hold the assumption of stability for both $[K^+]$ and HR values and previously adopted for similar purpose (i.e. TW-based index extraction for $[K^+]$ variations monitoring) [141]. For each i-th 2-min segment, the predominant TW polarity, defined as that having the highest number of occurrences, was obtained. This preliminary step was essential since TW polarity change can be physiological or induced by delineator oscillation when by-phasic to regular TWs appears almost indistinguishable. A TW was considered to have inverted polarity if the magnitude of its peak had negative sign and vice-versa. Only those TWs having the same polarity as the predominant one were considered for the following steps.

First, all the selected TWs were aligned with respect to their gravity center and used to compute an initial MWTW. Then, all the TWs were checked to find and discard the outliers, defined as having time duration outside the range $T_{dm_i} \pm 1.5 \times \sigma_{d_i}$ being T_{dm_i} and σ_{d_i} the mean TW duration and standard deviation of the TWs duration respectively, for the i-th segment. Finally, among the remaining, only those

TWs highly correlated (Pearson's correlation > 0.98) with the initial MWTW were used to recalculate a final MWTW, which best represents the general TW morphology for that particular segment.

Since hyperkalemia has been reported to cause TW inversions [197], any MWTWs with negative-polarity was inverted before performing the warping with the reference MWTW.

Once extracted all the MWTW, time warping analysis (described in section 2.3.4) was performed. The MWTW at the end of the HD treatment was taken as the reference for parameters computation, given that it is the time when the patient (a) is supposed to have recovered the normal $[K^+]$ level and (b) was discharged from hospital, being an appropriate reference for out-of-hospital ambulatory monitoring.

For comparison purposes, both T_w [134] and $T_{S/A}$ [141] were extracted from each MWTW and their performance, with respect to time warping based parameters in monitoring $[K^+]$, was assessed.

2.3.9 Potassium concentration variations $\Delta[K^+]$

The proposed parameters have been compared with the relative variations in $[K^+]$ (denoted as $\Delta[K^+](h)$) with respect to a reference $[K^+]$ that was taken at the end of the HD:

$$\Delta[K^+](h) = [K^+]_h - [K^+]_r \tag{2.26}$$

being $[K^+]_h$ the concentration at the h-th hour during the HD and $[K^+]_r$ the concentration at the end of the treatment. An example of the $\Delta[K^+](h)$ evolution is shown in Figure 2.7a (purple diamonds).

2.3.10 Statistical analysis

Results are presented as median and interquartile range (IQR). Spearman rank correlation coefficient (ρ) and Pearson correlation (r) were used for correlation analysis between $\Delta[K^+]$ and the marker, giving information about both the monotonic relation and the strength of the association between the markers and $[K^+]$ changes and then providing a more complete characterization.

The average duration of the ECG recordings was 44 hours mainly due to electrode detachment or early battery exhaustion. For this reason, in this chapter, correlation coefficients were computed by using the first five values of $\Delta[K^+](h)$ throughout the HD (i.e., h_0 to h_4 in Figure 2.1) and the warping markers evaluated at the corresponding i-th segment points ($h = (i-1)/2$ where i=1,3,5,7,9 or i=1,3,5,7,8 depending on the HD duration). All statistical analyses were performed using MATLAB.

2.4 Results

In this study, ECG signals and $[K^+]$ from 29 ESRD patients undergoing HD were investigated. An example of d_w and $\hat{d}_{w,c}$ time evolution for a particular patient, in PCA approach, was provided in Figure 2.5. ΔRR was represented on the x-axis in both panels, while d_w and $\hat{d}_{w,c}$ were shown on the y-axis in panel (a) and panel (b), respectively. The least-square fitting line (red line) was depicted in both panels. Spearman's correlation coefficients (ρ) and p-values were also showed in each panel. High and significant correlation ($\rho = -0.90$ and p-val < 0.001) was found between ΔRR and d_w. However, after correcting for the HR-dependency, $\rho = 0.03$ and p-val$= 0.76$.

Boxplots in Figure 2.6 show the distributions of $\Delta[K^+]$ and the proposed PCA-based time warping descriptors during HD. Figure 2.7b shows the average time evolution of PCA-based d_w^u, d_w, $\hat{d}_{w,c}$ and d_w^{NL} in the studied population along the monitoring period, while d_a and d_a^{NL} are in Figure 2.7c.

Table 2.3 shows the intra-patient Spearman's (ρ) and Pearson's (r) correlation coefficients computed between $\Delta[K^+]$ and the time warping parameters. In both single-lead and PCA approaches, the highest median Spearman's and Pearson's correlation coefficients were found for d_w^u, d_w and $d_{w,c}$ being $\rho \geq 0.82$ and $r \geq 0.86$ for single-lead analysis and $\rho \geq 0.82$ and $r \geq 0.89$ in PCA.

Spearman's and Pearson's correlation coefficients between $[K^+]$ values and mean HR, expressed in beats per minute (bpm), during the HD period were computed and the results are presented in Table 2.4. The Spearman's correlation coefficient median (IQR) values were 0.10 (1.35), with p-val$= 0.33$. Similarly, Pearson's correlation coefficient median (IQR) were 0.09 (1.45) with p-val$= 0.22$.

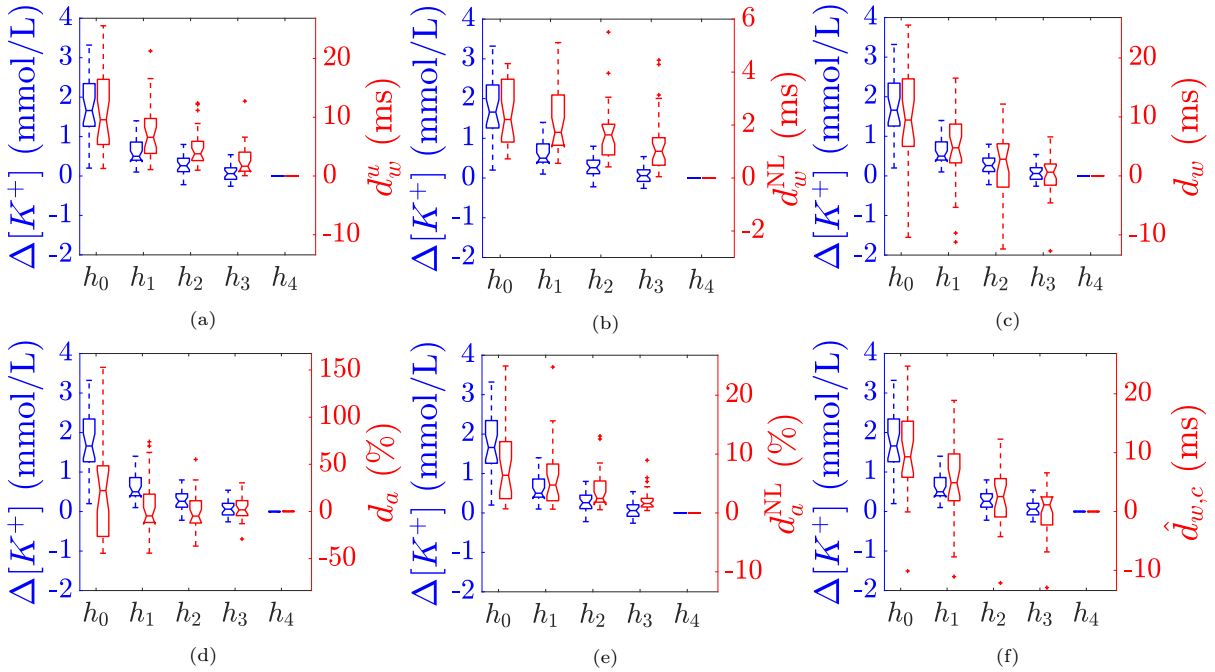

Figure 2.6: Distribution of blood potassium variations ($\Delta[K^+]$) and PCA-based time warping markers during the HD. In each panel, $\Delta[K^+]$ (blue) and markers (red) distributions are provided at any time point from the beginning, h_0, to the end, h_4, of the HD session (h_0 to h_4 in Figure 2.1). The central line of the boxplots represents the median, the edges of the box are the 25-th and 75-th percentiles, and the whiskers extend to the most extreme data points not considered as outliers. The notches represent the 95% confidence interval of the median, calculated as $q_2 - 1.57(q_3 - q_1)/\sqrt{n}$ and $q_2 + 1.57(q_3 - q_1)/\sqrt{n}$ being q_2 the median, q_1 and q_3 are the 25-th and 75-th percentiles, respectively, and n is the sample size. Finally, red "+" denotes outliers.

2.5 Discussion

In this chapter, two previously reported potassium estimators, T_w [134] and $T_{S/A}$ [141], four warping-based ECG-derived descriptors for $[K^+]$ monitoring proposed in Ramírez *et al.* [166], d_w^u, d_a, d_w^{NL}, d_a^{NL}, and the here proposed modified versions d_w and $d_{w,c}$ were tested as bloodless indices for $[K^+]$ variations in ESRD patients undergoing HD therapy computed from standard leads as well as in a PCA-derived lead. The most encouraging results, in terms of correlation, were obtained for markers d_w^u, d_w, and $d_{w,c}$, leading to the highest median intra-patient $\rho \geq 0.82$ and $r \geq 0.87$ in single-lead and $\rho \geq 0.82$ and $r \geq 0.89$ in PC1 lead respectively, evidencing high monotonic and linear association with $[K^+]$ and making them a promising non-invasive indices for blood $[K^+]$ monitoring.

2.5.1 Comparison between d_w^u and d_w

The signed marker d_w followed a similar time-trend as the original d_w^u during the whole monitoring period, showing a similar distribution in Figure 2.7b, as a result of the fact that the sign computed as in eq. (2.8) is positive in roughly all the patients. That can be explained by the fact that the TW morphology in hyperkalemia is usually more peaked and shorter in time than a TW from regular $[K^+]$ concentrations, as happens at the end of HD, where the reference has been taken [90, 91].

Therefore, all the other MWTWs needed to be shrunk in amplitude and widened in time duration during the warping procedure to fit the reference one, and this is given by a positive signed d_w. However, other external factors, such as the potassium removal rates [198] or the dialysate potassium level [199, 200], might also have played a role in altering ventricular repolarization activity.

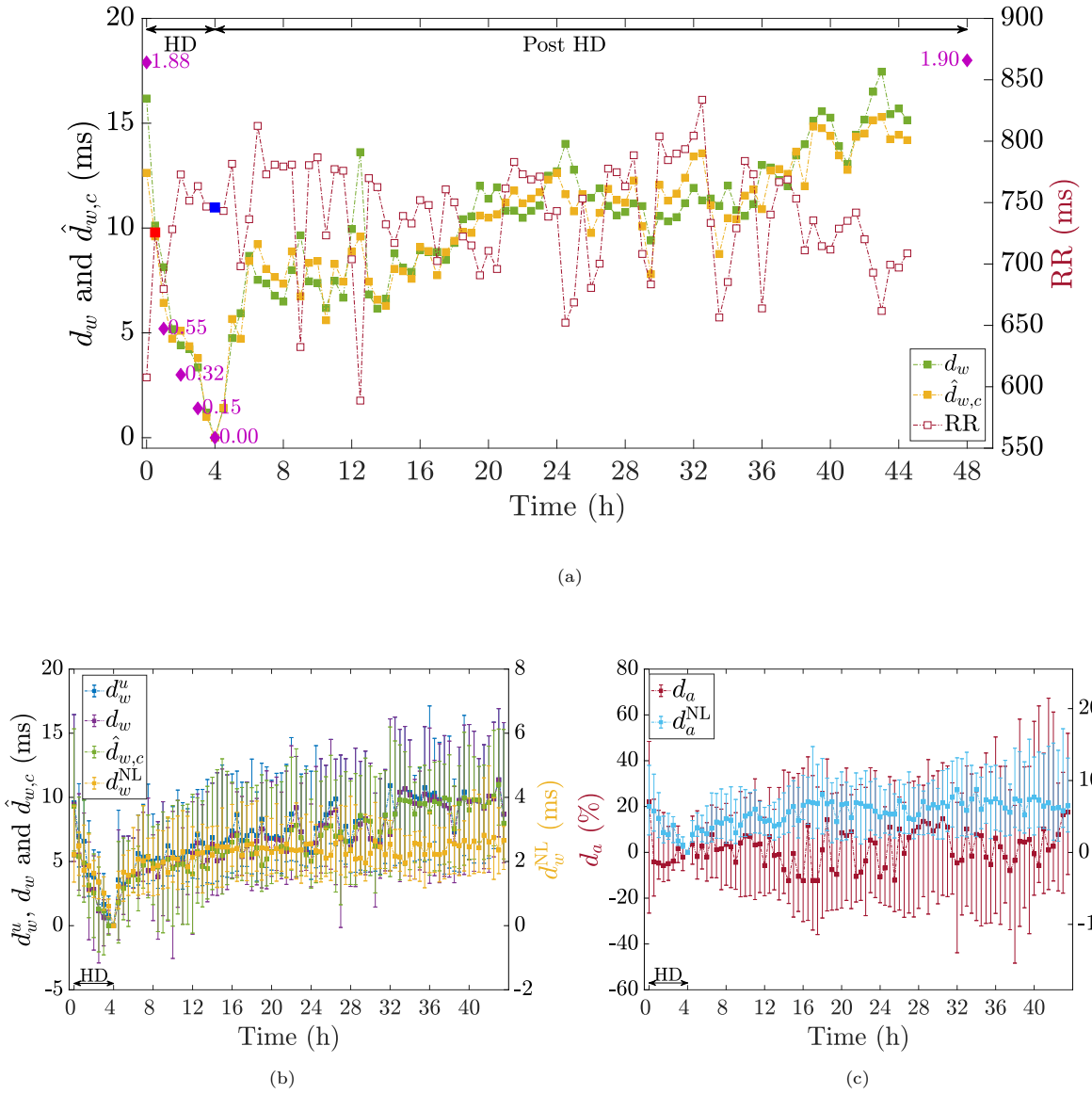

Figure 2.7: PCA-based time warping markers and RR interval time trends. An example for a given patient undergoing 4h-long HD therapy, is depicted in panel (a) with the evolution of d_w (filled green squares), $\hat{d}_{w,c}$ (filled orange squares), both referring to the left vertical scale, and the average RR intervals (unfilled dark red squares, referring to the right vertical scale). $\Delta[K^+]$ relative variations with respect to the concentration at HD end (purple diamonds) are expressed in mmol/L. Time is expressed in hours from the beginning of the treatment onward. Each square denotes the mean RR interval in a 2-min wide segment used to compute the warping parameters, while the highlighted blue square corresponds to the reference segment at the end of HD. The filled red square denotes the time-point from which the studied MWTWs in Figure 2.3 was selected. Note that for this patient, the Holter recording did not reach the planned 48h. Panel (b) shows the median and IQR for each observing i-th segment, computed by using the values from all the available patients for d_w^u, d_w and $\hat{d}_{w,c}$ and d_w^{NL} (this latter refers to the right axis, while the others to the left). Time trends (expressed as median and IQR) for d_a and d_a^{NL}, referring to the left and right axes respectively are in panel (c). Panels (b) and (c) give an overview of the time evolution for these descriptors along the ECG acquisition from the beginning of the HD onward. Only the first 44h were depicted being that the average ECG duration in the DEKOALE dataset.

Table 2.3: Intra-patient Spearman's (ρ) and Pearson's (r) correlation coefficients between $\Delta[K^+]$, and time warping based markers, and T_w and $T_{S/A}$, in all cases evaluated from the PC1 transformed lead, and from standard single leads II, V3, V4, V5 and V6. Values are expressed as median (IQR).

	Spearman's (ρ)						Pearson's (r)					
	PCA	II	V3	V4	V5	V6	PCA	II	V3	V4	V5	V6
d_w^u	0.90 (0.37)	0.90 (0.40)	0.86 (0.50)	0.90 (0.38)	0.90 (0.25)	0.90 (0.29)	0.92 (0.36)	0.91 (0.37)	0.85 (0.37)	0.86 (0.41)	0.92 (0.14)	0.86 (0.30)
d_w	0.82 (0.45)	0.90 (0.37)	0.90 (0.49)	0.90 (0.46)	0.90 (0.30)	0.90 (0.39)	0.89 (0.35)	0.90 (0.26)	0.88 (0.31)	0.86 (0.39)	0.93 (0.11)	0.87 (0.29)
$\hat{d}_{w,c}$	0.90 (0.31)	0.82 (0.28)	0.86 (0.40)	0.90 (0.50)	0.90 (0.30)	0.90 (0.38)	0.89 (0.25)	0.87 (0.33)	0.89 (0.29)	0.86 (0.49)	0.91 (0.17)	0.86 (0.27)
d_w^{NL}	0.82 (0.57)	0.43 (0.60)	0.70 (0.45)	0.67 (0.60)	0.70 (0.64)	0.80 (0.56)	0.68 (0.52)	0.47 (0.58)	0.61 (0.47)	0.56 (0.45)	0.56 (0.64)	0.61 (0.47)
d_a	0.21 (1.20)	0.00 (1.22)	0.50 (0.80)	0.40 (1.45)	0.45 (1.59)	-0.10 (1.15)	0.57 (1.53)	0.14 (1.55)	0.83 (0.67)	0.63 (1.71)	0.62 (1.65)	-0.32 (1.52)
d_a^{NL}	0.80 (0.42)	0.65 (0.70)	0.70 (0.59)	0.70 (0.77)	0.86 (0.45)	0.87 (0.40)	0.75 (0.39)	0.82 (0.83)	0.66 (0.56)	0.68 (0.84)	0.88 (0.30)	0.84 (0.38)
T_w	-0.70 (0.59)	-0.84 (0.57)	-0.90 (0.52)	-0.75 (0.67)	-0.80 (0.63)	-0.90 (0.65)	-0.92 (0.32)	-0.85 (0.35)	-0.87 (0.40)	-0.81 (0.62)	-0.84 (0.44)	-0.75 (0.48)
$T_{S/A}$	0.80 (0.42)	0.62 (0.80)	0.60 (0.85)	0.46 (1.07)	0.76 (0.59)	0.63 (0.69)	0.86 (0.38)	0.83 (0.77)	0.71 (0.65)	0.46 (0.83)	0.74 (0.45)	0.72 (0.52)

Table 2.4: Blood potassium concentration $[K^+]$ values (in mmol/L) at each blood extraction during the HD (h_0 to h_4, see Figure 2.1) and corresponding HR (beats/min). Spearman's (ρ) and Pearson's (r) intra-patient correlation coefficients between $[K^+]$ and RR. Values are expressed as median (IQR).

	h_0	h_1	h_2	h_3	h_4	ρ	r
$[K^+]$	5.00 (1.36)	3.85 (1.08)	3.64 (0.84)	3.39 (0.74)	3.30 (0.62)	0.10	0.09
HR	81 (28)	76 (28)	80 (23)	80 (17)	80 (25)	(1.35)	(1.45)

2.5.2 The HR correction of the d_w improve the correlation with $\Delta[K^+]$

The warping algorithm is applied over the MWTWs computed from different observing windows with different HRs. Therefore, a corrected version of the d_w, derived similarly to the QT correction formula [194, 195], was proposed since the HR influences this marker as pointed out in Ramírez *et al.* [166], and can be observed in Figure 2.4 as an example around hours h=9, 12 and 43.

A large number of models have been proposed for the computation of QTc values independent of HR [193–196]. However, a previous study [194] found that the linear regression model fits better than any other model to the relationship between QT and the RR intervals. Also, for small RR variations, in section 2.3.7 it is shown that hyperbolic QT to RR dependency becomes linear. Therefore, we used a linear model to derive an HR-corrected index, $d_{w,c}$. This approach was used to estimate the d_w component strictly related to $[K^+]$ removing its relation with HR as showed in Figure 2.5, where the HR-dependency, clearly visible in panel (a), was cancelled after the correction, panel (b).

Comparing the results for d_w^u, d_w and $\hat{d}_{w,c}$, all of them have proved to be highly correlated with $[K^+]$ variations. However, it is important to remember that d_w^u (an so d_w) is biased by the HR effects as previously described [166], while $\hat{d}_{w,c}$ is no longer dependent on it, possibly being responsible for the

lower IQR in the correlation, 0.25, as compared to 0.35 and 0.36 for d_w and d_w^u, respectively (see Table 2.3, PCA column). It should also be noted that the small differences between the ρ and r computed for $\hat{d}_{w,c}$ and d_w could be due to the low HR variations observed during HD, but larger HR variations, and consequently a higher impact of the correction, are expected in ambulatory monitoring.

2.5.3 d_a marker shows poor correlation with $\Delta[K^+]$

As described in section 1.4.3, ECGs recorded under hyperkalemic conditions commonly present TWs which are taller than those for normal levels of blood $[K^+]$. The marker d_a was designed to capture the amplitude variability between the reference, $\boldsymbol{f}^r(\boldsymbol{t}^r)$, and the studied, $\boldsymbol{f}^s(\boldsymbol{t}^s)$, MWTWs after warping. However, from its original definition, d_a can take both positive and negative values, producing positive intra-patient ρ and r between $\Delta[K^+]$ and d_a in 62% of the cases and negative in 38% of the cases. This explains the low median inter-patient correlation ($\rho = 0.21$) and the wide IQR (1.20).

Nevertheless, if its absolute value was considered then correlation between $\Delta[K^+]$ and d_a becomes larger being $\rho = 0.70$ (0.60) and $r = 0.75$ (0.31).

2.5.4 The non-linear time warping markers reflect $[K^+]$ fluctuations

Cellular AP duration can be affected in a heterogeneous manner by $[K^+]$ fluctuations since ion channel expression is heterogeneous throughout the ventricles [10] and this can result in non-linear changes on T-wave morphology. According to their definition [166], d_w^{NL} and d_a^{NL} were designed to quantify the inhomogeneous morphological variations during ventricular repolarization; this fact might explain their correlation with $\Delta[K^+]$. Both markers showed a remarkable sensitivity to the variations of ventricular spatio-temporal dispersion independently from changes in HR [166], meaning that they did not need a HR correction as was done for d_w. This last point, particularly for d_a^{NL}, in addition to its also high correlation with $\Delta[K^+]$, make it an interesting TW descriptor for blood $[K^+]$ assessment.

2.5.5 Relationship between HR and $[K^+]$

In this chapter, the correlation between HR and $[K^+]$ was investigated, finding no significant correlation between them. To place these results into a proper context, in a previous study on computer-based models it was found that the heart rate in ESRD patients undergoing HD is influenced by the combined effects of $[K^+]$, calcium and pH [201]. In particular, it was observed that when $[K^+]$ is between 3 and 4 mmol/L, the HR sensitivity is about 10 bpm/mmol of $[K^+]$ [201].

As reported in Table 2.4, the median $[K^+]$ falls within the above mentioned range from h_1 to h_4 (i.e., during the entire HD session) but the range of HR variations is much bigger than the 10 bpm mentioned in Severi *et al.* [201] (minimum IQR = 17 bpm at h_3) so anticipating the obtained low and insignificant median correlations coefficients between HR and $[K^+]$. This result suggests that HR variations are a poor indicator of $\Delta[K^+]$, at least in our dataset. Moreover, this finding gives validity to the proposal of the $\hat{d}_{w,c}$ presented in this work, which assumes no correlation between HR and $[K^+]$-related changes on TW morphology.

2.5.6 Performance evaluation of the proposed time warping indexes respect to T_w and $T_{S/A}$

In a previous study [154] a comparison of T_w, $T_{S/A}$, d_w, d_w^{NL}, d_a and d_a^{NL}, based on a electrophysiological simulation of ECG under hyperkalemia, was performed, and tested on a subset of the ESRD patients undergoing HD therapy. In that study, it is shown that similar results were obtained in terms of Pearson's correlation coefficient between $[K^+]$ and T_w, $T_{S/A}$, and time warping based markers, also showing a high correlation with HR.

In the present work we extended the analysis by increasing the sample size, introducing the proposed correction by HR, and comparing with single lead recordings. According to the Spearman's (ρ) and Pearson's (r) correlation coefficients, the median values are higher, and the IQR smaller, for d_w^u, d_w

and $d_{w,c}$ than for $T_{S/A}$ using both PCA and standard single-lead approaches. For T_w, we found similar r median absolute values, as compared to d_w^u, d_w and $d_{w,c}$, while Spearman's correlation values were much lower for T_w when using PCA and several single-leads (e.g. lead V4 and V5). This shows that the proposed time warping based markers present either higher correlation or stronger monotonic relationship with $\Delta[K^+]$ than T_w, and $T_{S/A}$, making them more suitable for $[K^+]$ monitoring purposes.

2.5.7 Clinical Significance

In this chapter it has been demonstrated that d_w, $\hat{d}_{w,c}$ and d_w^{NL} have potential value in monitoring changes in blood potassium concentration. All of them exhibit a time-course similar to that of $[K^+]$ in ESRD patients undergoing HD as described in literature [199, 200]: a rapid decline during the HD with a fast rebound just after the end of the therapy as continued mobilization of potassium from intracellular space to extracellular space occurs, followed by a steady increase in the remaining hours before the next HD session (see Figure 2.7b and Figure 2.7c).

Based on that, it seems reasonable to consider the use TW time warping based markers for continuous $[K^+]$ monitoring, also in other clinical scenarios such as in patients suffering heart failure [202], where hyperkalemia also increases the risk of SCD.

2.5.8 Limitations

The main limitation concerns the reduced amount of blood tests (only six) took from each patient during the 48-hour ECG recording, which provided an accurate representation of the $[K^+]$ time evolution only during HD, but not during the ambulatory period. On this basis, it was possible to investigate the relationship between the proposed markers and the $\Delta[K^+]$ only during the therapy but not through the remaining hours. Moreover, the course of HD procedures can be accompanied by ischaemia [203, 204], which can also be associated with changes in the TW, independently from HR, therefore reflected on $d_{w,c}$. Elucidation of its impact in monitoring normal-life outside the HD process needs to be explored in a dedicated study.

Postural or body position changes (BPC) are known to affect the TW morphology and mainly the TW amplitude [205], which can influence d_a related markers. The fact that those markers were measured on PCA lead could attenuate the effect of BPC on TW, however in chapter 3 a specific study is performed to precisely establish the impact of this aspect on the TW-time warping markers.

Assessment of the performance of the proposed descriptors in patients with hypokalemia remains to be studied. In addition, the methodology proposed in this work needs to be validated in: a) a larger population; and b) subsequent HD sessions on the same population, which would allow to quantify the accuracy in $[K^+]$ estimation.

Finally, PCA transformation may be dominated by TWs in precordial leads (see section 1.4.1), which have the highest amplitude. In other words, the algorithm may have not captured the morphological variation reflected in other leads.

2.6 Conclusions

In this chapter, ECG-based time warping markers (d_w, d_a), their non-linear components (d_w^{NL} and d_a^{NL}) and a HR corrected version $d_{w,c}$, in all cases personalised making it relative to a reference point (the end of the HD), were studied in ESRD patients undergoing HD and evaluated as estimator of $[K^+]$ changes over time.

Among the analysed markers and methods (i.e. standard single-lead or PCA transformed lead approaches), the proposed PCA-based d_w and its HR corrected version, $d_{w,c}$, achieved better results than the previously proposed $T_{S/A}$ in terms of both Spearman's and Pearson's correlation with $\Delta[K^+]$, and showed higher monotonic relationship than T_w. This makes the proposed time warping markers a valid and more accurate alternative to the currently available tools for routine $[K^+]$ monitoring of ESRD patients undergoing HD without the need of invasive blood test, in both hospital and ambulatory scenarios.

CHAPTER

3

Periodic Component Analysis to Improve time warping Marker Robustness

3.1 Introduction

In chapter 2, TW morphology markers, obtained by applying time warping analysis, have been proposed for noninvasive $[K^+]$ variation monitoring in ESRD patients undergoing HD, and their performance was assessed against two previously proposed TW-based markers: the width of the TW [134], the TW slope-to-amplitude ratio [141]. All these markers were extracted from standard single-lead and from the first PC, and the most promising results were found for PCA-based d_w, $\hat{d}_{w,c}$ and d_w^{NL}.

However, PCA is a LSR technique that maximise TW variance, which may not be the best strategy for emphasising clinically relevant information [163]. Indeed, PCA's maximum-variance criterion might be problematic when there is a low SNR or in the presence of body position changes (BPC) [172,206]. In other words, PCA may not be able to distinguish between noise and the useful $[K^+]$-driven TW morphological variations, thus jeopardizing the potential clinical significance of time warping based markers.

An alternative LSR technique to PCA is periodic component analysis (πCA) [207,208], which transforms the multi-lead ECG signal by maximizing the periodic components on the TL. This technique was already applied for TW alternans detection on ECG [163], demonstrating superior performance to PCA in noisy scenarios. In this chapter, πCA was performed to enhance the TW one-beat periodicity under the hypothesis that it would outperform PCA in minimising the contribution of noise and other non-cardiac, no-beat periodic sources before deriving time warping based markers to monitor $[K^+]$ variations.

TW changes can also occur as a consequence of causes other than $[K^+]$ variations including (i) BPC which have been shown to influence TW morphology, in particular its amplitude [205, 209] and (ii) different noise sources [210]. These sources could affect the specificity and robustness of TW morphological markers as surrogate of electrolyte changes, thus jeopardising their clinical validity.
In this chapter, a detailed analysis is carried out to understand how both BPC and noise influence the TW-based descriptors as function of the TL.

This chapter aims to compare the performance of πCA and PCA as LSR techniques prior to TW time warping analyses for deriving robust TW-based markers for $[K^+]$ monitoring.

3.2 Materials

Two data sets were analysed in this chapter: ECG signals from DEKOALE dataset (section 2.2) as well as recordings from 20 healthy subjects undergoing controlled BPC.

3.2.1 BPC dataset

The BPC database contains ECGs from 20 healthy (eleven males and nine females, 32 $\pm$ 9 years old) performing the following sequence of BPC: supine (S), right side (R), and left side (L): S→R→S→L [211]. The complete sequence was repeated five times with a duration of 1 min per body position, so that muscular activity and other artifacts were allowed to decay before the next BPC was initiated. A standard 12-lead ECG was simultaneously acquired at a sampling rate of 1 kHz and amplitude resolution of 0.6 μV [205]. All participants gave explicit consent to participate in the study. The experimental procedures involving healthy volunteers described in this data collection were in agreement with the principles outlined in the Helsinki Declaration [205, 211].

The BPC database has been made available for the study by professor Leif Sörnmo from Lund University, Lund, Sweden.

3.3 Methods

3.3.1 ECG preprocessing and single lead analysis

As reported in section 2.3.1, preprocessing of ECG recordings included baseline wander removal at 0.5 Hz in each lead and low-pass filtration to remove power-line noise and to attenuate muscular activity. Then, QRS complexes were detected and TW delineated using the wavelet-based delineation previously mentioned in section 2.3.2. An example ECG before and after this pre-processing are in in Figure 3.1a and Figure 3.1b, respectively. Similarly to the study done in chapter 2, standard lead analysis was performed for ECG signals in the DEKOALE dataset. In this chapter, TW were selected in leads II, V4 and V6 being those having the highest Spearman's and Pearson's correlation coefficients, in median, with $\Delta[K^+]$ (see Table 2.3). In addition, as previously explained, waveforms from leads V4 and V6 were used in a previous study [145] for estimating $[K^+]$ while lead II is the most popularly used in patient monitoring [170].

3.3.2 Lead space reduction techniques

For each ECG recording, a transformation matrix $\mathbf{\Psi}$ was obtained using πCA or PCA and applied to the 8 independent leads (I, II, V1, V2, V3, V4, V5 and V6) to obtain 8 TLs. Since the different datasets investigated in this study were recorded under different conditions, πCA and PCA learning period locations were specifically defined for each of them and summarised in Table 3.1. The portion of heartbeat (onset and end points) considered in the learning of each LSR technique are summarised in Table 3.2.

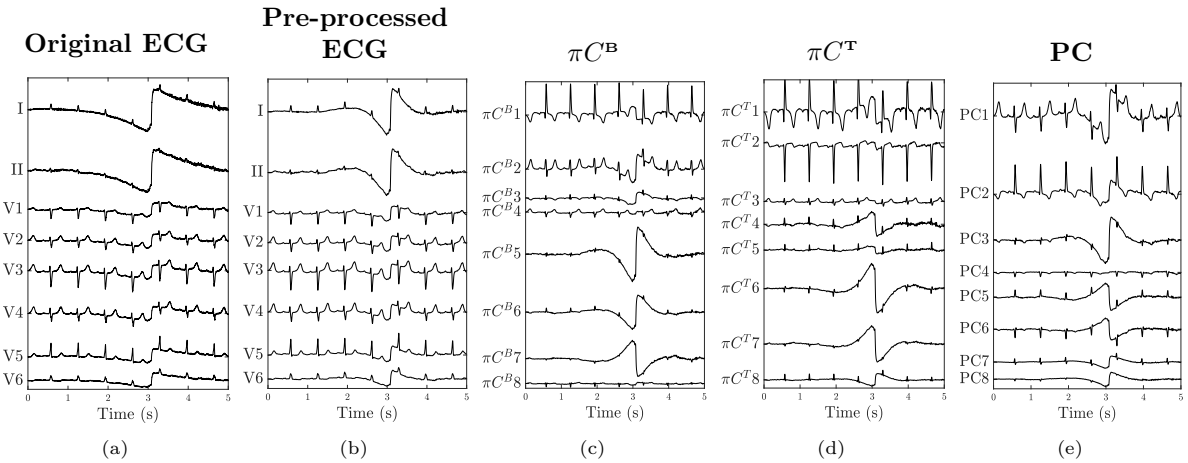

Figure 3.1: Example of the implemented ECG pre-processing and πC^{B}, πC^{T} and PCA computation. Panel (a) shows the original eight independent ECG leads from a particular ESRD patient undergoing HD while in panel (b) is depicted the final pre-processed filtered signal from panel (a) as described in section 3.3.1. Panels (c), (d) and (e) show, πC^{B}, πC^{T} and PCs, respectively, obtained after linear transformation of (b). Figure from [212].

Principal Component Analysis

The matrix $\mathbf{\Psi}_{\mathrm{PCA}}$ defining the PCA transformation was obtained from the eigenvectors of the 8×8 inter-lead ECG auto-correlation matrix computed using the samples in the TW, as described in section 2.3.3, within the corresponding learning window (see Table 3.2).

Periodic component analysis

This technique aims to emphasise the periodic structure of the 8 independent leads, instead of the variance as in PCA. In this work, we applied $\mathbf{\Psi}_{\pi CA}$ to maximise the beat-to-beat periodic components on the transformed signal, in contrast to [163], where it was used to emphasise the every-second-beat periodicity for TW alternans detection. To avoid spurious variability due to errors in QRS detection (section 3.3.1), a pre-alignment of QRS complexes falling within the learning period (see Table 3.1) at each lead was performed. Then, TWs were obtained by using a window from R wave peak (R_p) plus 60 ms to R_p + 400 ms. The complete QRST complex, defined as the segment from R_p-80 ms to R_p + 400 ms, was also extracted (Table 3.2). Then πCA was computed by learning either at the TWs or at the complete QRST complexes, resulting in πC^{T}#s, or πC^{B}#s, respectively.

3.3.3 Computation of πCA transformation matrix

Let K be the number of aligned TW (or QRST complexes) in the learning window, having N samples each, for L available leads. Let $x_{k,l}(n)$ denote the n-th selected sample of the k-th beat in the l-th lead of the filtered ECG signal. In vector notation, $\mathbf{x}_{k,l} = \begin{bmatrix} x_{k,l}(0) & \cdots & x_{k,l}(N-1) \end{bmatrix}^T$ represents the TW (or QRST complex) from the k-th beat of the l-th lead, which are piled together in the $L \times N$ matrix $\mathbf{X}_k$:

$$\mathbf{X}_k = \begin{bmatrix} \mathbf{x}_{k,1} & \mathbf{x}_{k,2} & \dots & \mathbf{x}_{k,L} \end{bmatrix}^T, \tag{3.1}$$

where the n-th column of $\mathbf{X}_k$ contains the amplitudes of the L leads at a given sample n. Two data matrices $\mathbb{X}$ and $\mathbb{X}^{(m)}$ were then constructed by concatenating K consecutive matrices $\mathbf{X}_k$,

$$\mathbb{X} = \begin{bmatrix} \mathbf{X}_1 & \mathbf{X}_2 & \cdots & \mathbf{X}_K \end{bmatrix}, \tag{3.2}$$

and the m-beat delayed version

$$\mathbb{X}^{(m)} = \begin{bmatrix} \mathbf{X}_{m+1} & \mathbf{X}_{m+2} & \cdots & \mathbf{X}_{m+K} \end{bmatrix}. \tag{3.3}$$

Table 3.1: Time excerpts location for: i) learning of $\mathbf{\Psi}_{PCA}$ and $\mathbf{\Psi}_{\pi CA}$, ii) MWTW analysis for markers estimation and iii) MWTW reference computation.

DEKOALE datset	BPC	ECG Simulation
Learning period to estimate $\mathbf{\Psi}_{PCA}$ and $\mathbf{\Psi}_{\pi CA}$ matrices		
10-min window at the end of HD	60-s window at first supine position	Last 60 beats simulating the end of HD
Width and analysis window locations of MWTW and marker estimation		
2-min every 30 min	60-s (each BPC)	Intervals of 60 beats
Window location for reference MWTW computation		
End of HD [167]	First supine position	Last 60 beats simulating the end of HD

Table 3.2: Segmented beat excerpt limits for PCA and πCA learning. R_p, T_{on} and T_{end} positions were obtained by using the delineator described in section 2.3.2.

	πC^{B}	πC^{T}	PCA
Initial Point	R_p - 80 ms	R_p + 60 ms	T_{on}
Final Point	R_p + 400 ms	R_p + 400 ms	T_{end}

To maximise the m=1-beat periodicity of the signal, the desired πCA transformation must minimise the following residual measure of periodicity [163]:

$$\varepsilon(\mathbf{w}) = \frac{\|\mathbf{w}^T\mathbb{X}^{(1)} - \mathbf{w}^T\mathbb{X}\|}{\|\mathbf{w}^T\mathbb{X}\|}. \tag{3.4}$$

By the Rayleigh-Ritz theorem, it can be shown that the weight vector $\mathbf{w}^* = \begin{bmatrix} w_1^* & w_2^* & \cdots & w_L^* \end{bmatrix}^T$ that minimises eq. (3.4) is given by the generalised eigenvector corresponding to the smallest generalised eigenvalue of the matrix pair $\left(\mathbf{A}_{\mathbb{X}}^{(1)}, \mathbf{R}_{\mathbb{X}}\right)$ that accomplishes the following equation:

$$\mathbf{A}_{\mathbb{X}}^{(1)}\mathbf{\Psi}_{\pi CA} = \mathbf{R}_{\mathbb{X}}\mathbf{\Psi}_{\pi CA}\mathbf{\Lambda}, \tag{3.5}$$

being $\mathbf{\Lambda}$ a diagonal matrix containing the eigenvalues at the diagonal, $\mathbf{R}_{\mathbb{X}}$ the spatial correlation matrix of $\mathbb{X}$, estimated as

$$\mathbf{R}_{\mathbb{X}} = \frac{1}{KN}\mathbb{X}\mathbb{X}^T, \tag{3.6}$$

and $\mathbf{A}_{\mathbb{X}}^{(1)}$ the spatial correlation of the non-beat-to-beat periodic residue, estimated as:

$$\mathbf{A}_{\mathbb{X}}^{(1)} = \frac{1}{KN}\left(\mathbb{X}^{(1)} - \mathbb{X}\right)\left(\mathbb{X}^{(1)} - \mathbb{X}\right)^T. \tag{3.7}$$

Then, the transformation matrix $\mathbf{\Psi}_{\pi CA}$ is taken as the generalized eigenvector matrix of matrix pair $\left(\mathbf{A}_{\mathbb{X}}^{(1)}, \mathbf{R}_{\mathbb{X}}\right)$, with the eigenvectors (columns) sorted according to the corresponding eigenvalues in ascending order of magnitude. In this way, the transformation $\mathbb{Y} = \mathbf{\Psi}_{\pi CA}^T\mathbb{X}$ projects the component with smaller relative non-periodic residuum (i.e., the most periodic component) into the first row of $\mathbb{Y}$.

An illustration of πC^{B}#, πC^{T}# and PC# and be found in Figure 3.1c, Figure 3.1d and Figure 3.1e. As hypothesised, the high-energy artifact around second 3 in Figure 3.1b is preserved in PC1 but much more attenuated in the first two πC^{B} and πC^{T} components. Also note that πC^{B} dominantly emphasises the QRS at $\pi C^{\mathrm{B}}1$, while the TW is dominantly emphasised at $\pi C^{\mathrm{T}}1$.

3.3.4 TW morphology markers

For all datasets, $\pi C^{\mathrm{T}}1$ and PC1 were taken for subsequent analyses while the optimal $\pi C^{\mathrm{B}}\#$ was chosen as the one ($\pi C^{\mathrm{B}}1$ or $\pi C^{\mathrm{B}}2$) having the highest TW energy content, by computing the total TW energy within the same period used for learning (see Table 3.1) as there is no guarantee that the highest TW energy content is in $\pi C^{\mathrm{B}}1$ or in $\pi C^{\mathrm{B}}2$, due to the interplay between TW and QRS dominance at TL energy projection, see Figure 3.1c.

All TW from the selected πCA or PCA were further low-pass filtered at 20 Hz using a 6-th order Butterworth filter to remove remaining out-of-band frequency components. Then, the specific analysis windows (see Table 3.1) were selected to perform the TW time warping. The duration of these windows was selected to be small enough to hold the assumptions of HR and $[K^+]$ values stability in case of ECGs from ESRD patients undergoing HD. In each window, a MWTW was computed as detailed in section 2.3.8.

Finally, the three TW time warping markers having the highest correlation with $[K^+]$ variations (i.e., d_w, $\hat{d}_{w,c}$ and d_w^{NL}) were estimated from the time excerpts locations described in Table 3.1 as detailed in section 2.3.5 and 2.3.7.

3.3.5 ECG simulation

To validate the usage of both πCA and PCA in extracting time warping parameters and to assess their performance against noise, a Monte Carlo simulation approach was adopted. Each trial was generated as the sum of a clean 8-lead ECG and an 8-lead noise component, expressed in the matrix $\mathbf{V}_{h_i}$ $(8 \times N)$, where $i \in \{0, \cdots, 4\}$ denotes each of the 5 hour time points corresponding to the blood sample extractions during HD with the noise being of one of these three types: baseline wander (bw), muscle artifact (ma), and electrode motion artifact (em).

MIT-BIH Noise Stress Test database

This database includes 12 half-hour ECG recordings and 3 half-hour recordings of noise typical in ambulatory ECG recordings [213], which were accessed by using the Wave Form Data Base (WFDB) Toolbox for MATLAB/Octave [214]. The noise recordings were made using physically active volunteers and standard ECG recorders, leads, and electrodes; the electrodes were placed on the limbs in positions in which the subjects' ECGs were not visible.

The three noise records were assembled from the recordings by selecting intervals that contained predominantly bw, ma and em. This last is generally considered the most troublesome, since it can mimic the appearance of ectopic beats and cannot be removed easily by simple filters, as can noise of other types.

Clean ECG signal

A set of clean beats were extracted from a ESRD patient under HD therapy having the following clinical features: (i) The patient was in evident hyperkalemia having, at the beginning of the therapy, $[K^+]$ >5 mmol/L; (ii) The patient did not suffer major adverse cardiovascular events or arrhythmic events; (iii) The patient underwent conventional HD, the most frequent in the dataset. Then, two-minute ECG windows were selected at each hour during the HD session (h_0 to h_4 in Figure 2.1 in correspondence to each blood sample and in each lead, the beats were detected, aligned and averaged to get a clean representative beat per lead and hour. Each of those representative beats were repeated 60 times and then concatenated for the five hours getting a clean 300-beat 8-lead synthetic ECG.

Noise generation

For each of the three type of noises, 100 different realisations $\mathbf{V}_{h_i}$ were extracted, to be added to the same clean ECG (previously described). Each realisation starts at an arbitrary point in one of the two leads of the noisy records also randomly selected.

In real signals, noise is spatially correlated but due to the its generation setup $\mathbf{V}_{h_i}$ wasn't. Therefore, to correlate $\mathbf{V}_{h_i}$ a realistic way, the first step was to estimate the spatial correlation of the real ECG noise

from which the clean beats were extracted. Thus, at each i-th hour, up to 150 segments of ECG, assumed to contain only noise (50 ms intervals following the TW end), were selected from each independent lead. These segments were concatenated creating the noise component of the 8-lead vectors which were then normalised to be zero-mean and unit standard deviation recordings from where the noise correlation matrix $\mathbf{R}_{\mathbf{V}_{h_i}}$ was estimated.

The Cholesky decomposition [215] was applied to $\mathbf{R}_{\mathbf{V}_{h_i}}$, obtaining a whitening matrix $\mathbf{D}_{h_i}$. The inverse of $\mathbf{D}_{h_i}$ was used to generate a spatially correlated noise $\mathbf{V}'_{h_i}$,

$$\mathbf{V}'_{h_i} = \mathbf{D}_{h_i}^{-1}\mathbf{V}_{h_i}. \tag{3.8}$$

These zero-mean, unitary-standard deviation $\mathbf{V}'_{h_i}$ noise components were modulated and added to the clean ECG to create five different SNR levels, SNR $\in \{10, 15, 20, 25, 30\}$ dB.

Transformation matrix estimation

A transformation matrix $\mathbf{\Psi}$ (using πCA or PCA) was estimated from the learning period in each noisy ECG , and later applied over: (i) the corresponding entire noisy signal, making both the learning and the lead transformation phases done over the noisy signal, and denoted "NtoN" and (ii) the simulated clean ECG, having the learning phase in noisy conditions while lead transformation done over the clean ECG, denoted "NtoC".

3.3.6 LSR performance quantification and statistical analysis

The analysis and statistical tests carried out to evaluate LSR technique performance in each dataset are presented in this section. Results are given as the median (IQR).

ESRD patients dataset

Two different analysis were performed on the results obtained from the ESRD patients undergoing HD.

Marker performance assessment during the HD: Pearson's (r) correlation coefficients were computed to test the linear association between each T-wave morphology marker d ($d \in \{d_w, \hat{d}_{w,c}, d_w^{\text{NL}}\}$) and the corresponding relative $[K^+]$ variations computed as in eq. (2.26) in section 2.3.9.

Marker dynamics evaluation in post HD: For every patient, a fitting error (ϵ) between each LSR-specific marker series d and its linear regression fit between the 12-th and 44-th hours after HD onset was computed [212, 216]. This ϵ provides information on the marker's deviation from a gradual linear trend along time, hypothesised a surrogate of the trend followed by $[K^+]$. An example of linear fit is presented in Figure 3.2.

BPC dataset

Markers extracted from BPC dataset by warping MWTWs from each BPC with respect to the reference taken at first supine position (Table 3.1) were tested to check their robustness against postural changes and, for that purpose, two different tests were carried out.

The warping markers were grouped by body position type and the non-parametric Kruskal-Wallis test was applied to check for statistically significant differences (p-val≤ 0.05) between the supine, right and left positions medians. This allowed to assess whether or not the TW markers were influenced by the posture.

To check whether the marker values generated by the $\Delta[K^+]$ during HD therapy are larger or comparable, and thus indistinguishable, to those generated by a BPC, we compared the values from each marker from the ESRD dataset with those from the BPC using the Mann-Whitney U-test. For this, markers from the BPC dataset were pooled together and, since the same BPC could occur in both directions (e.g. S→L, but also L→S), resulting in markers with the same magnitude but opposite sign, we extended the pool by duplicating each value and reverting its sign.

ECG simulation

For each LSR technique, noise type, marker (d), SNR (n), and simulation run (j), normalised relative errors e were computed as:

$$e_{n,d,j} = \sqrt{\frac{\sum_{i=0}^{4}\left(d^{\mathrm{NtoN}}(n,j,h_i) - d^{\mathrm{NtoC}}(n,j,h_i)\right)^2}{\sum_{i=0}^{4}\left(d^{\mathrm{NtoC}}(n,j,h_i)\right)^2}} \times 100 \tag{3.9}$$

where $n \in \{10,15,20,25,30\}$ dB accounts for the SNR, $j \in \{1,\cdots,100\}$ accounts for the simulation run for each noise type, $i \in \{0,\cdots,4\}$ for the i-th hour where the markers are estimated, and $d \in \{d_w, \hat{d}_{w,c}, d_w^{\mathrm{NL}}$. We considered the d^{NtoC} marker series as the reference for evaluation of markers under noisy conditions. The transformation matrix was learnt in the same noisy conditions, at the reference as when applied to estimate the marker, so the error really quantifies how the noise affects the computation of the marker rather than $\mathbf{\Psi}_{PCA}$ or $\mathbf{\Psi}_{\pi CA}$ estimation.

3.4 Results

3.4.1 DEKOALE dataset

As a results of the TW maximum energy content selection criterion, $\pi C^{\mathrm{B}}1$ was selected over $\pi C^{\mathrm{B}}2$ in 19 out of 29 patients (66%) as the TL having the highest TW energy.

The intra-patient Pearson's (r) correlation coefficients, calculated between $\Delta[K^+]$ and each time warping markers d computed with the LSR techniques (πC^{B}, πC^{T} and PCA) and the standard leads (II, V4 and V6) are shown in Table 3.3.

The temporal evolution for πCA and PCA-based d_w is depicted in Figure 3.3a up to the 44-th hour, the average ECG duration in the DEKOALE dataset. Similar dynamics were found for $\hat{d}_{w,c}$ markers, Figure 3.3b. A zoomed view of the first 10 hours is also presented in an inset in both Figure 3.3a and Figure 3.3b, allowing a proper time dynamics comparison with the 10 hours-long $[K^+]$-recovery curve (Figure 3.3c) available in the literature [199, 200].

Values of the fitting error ϵ for the trends of markers, expressed as median and IQR across patients, are given in Table 3.4. Finally, to further evaluate the relations among TL derived markers, Pearson's correlation between makers derived from πC^{B}, πC^{T}, PC along the whole ECG was computed for each patient, and presented in Table 3.5.

3.4.2 BPC dataset

Figure 3.4 shows the distributions of d_w (panel a), $\hat{d}_{w,c}$ (panel b) and d_w^{NL} (panel c) grouped by LSR technique: πC^{B}, πC^{T} and PC, and arranged according to the body position type: supine (S), right-side (R) and left-side (L).

The Kruskal-Wallis test was used for evaluating the statistical significance level of the differences across the supine, right and left positions for each πC^{B} (purple), πC^{T} (blue) and PC (green) and p-val are indicated in each panel. The Kruskal–Wallis test showed significant marker differences between positions for all markers and LSR techniques, with the exception of πC^{T}-based d_w and $\hat{d}_{w,c}$ (p-val$= 0.27$ and p-val$= 0.14$, respectively).

3.4.3 DEKOALE and BPC dataset results comparison

Figure 3.5 presents the distributions of $\Delta[K^+]$ (in blue), d_w, $\hat{d}_{w,c}$ and d_w^{NL} markers (in red) computed at different hours of the HD, being the rightmost boxplot the zero-mean distribution of each markers obtained

at the BPC dataset. The Mann–Whitney U-test significance values between zero-mean distribution markers from BPC dataset and h_2 and h_3 markers from DEKOALE dataset are shown over-plotted. For h_2, markers were always significantly different from the BPC cases. On the contrary, for h_3, only d_w^{NL} resulted significantly different from BPC marker values, also regardless of the LSR technique.

3.4.4 ECG simulation

Error plot showing the median and IQR values of e for d_w, $\hat{d}_{w,c}$ and d_w^{NL} computed from πC^{B}, πC^{T} and PC are depicted in Figure 3.6a, Figure 3.6b and Figure 3.6c respectively. In each panel, the blue line represents values for bw, while the orange and the yellow are for em and ma, respectively.

3.5 Discussion

In this chapter, periodic component analysis implemented in two different versions, πC^{B} and πC^{T}, was compared to PCA as LSR technique prior to TW time warping analysis. To perform a thorough and comprehensive evaluation of the proposed time warping markers, we investigated three different specific and supervised scenarios: (i) $[K^+]$ induced variations with no concurrent BPC (DEKOALE dataset during HD), (ii) controlled BPC with no concurrent $[K^+]$ variations (BPC dataset) and (iii) simulated ECGs with three types of added noise at different SNR values simulating $[K^+]$-driven TW induced variations but without BPC (ECG simulation dataset).

3.5.1 Preliminary considerations

The results in each dataset can be evaluated by themselves or jointly, based on the concurrency/non-concurrency of the underlying mechanism that generates the TW change (i.e., only postural changes in BPC dataset and controlled SNR in the simulate ECG). This allow the assessment of behaviour of the proposed markers in different scenarios, which can be later compared with those in the DEKOALE dataset, allowing a more complete understanding and evaluation of our findings.

Time warping markers were derived from the different transformed and standard leads and compared in terms of their ability for $[K^+]$ monitoring, as well as robustness against BPC and noise. Note that this study focused on the understanding of both dynamics and behaviour of the markers under controlled events that can be found during a regular ECG monitoring. In other words, the drawn were not affected by the duration of the different signals, as long as it ensures the correct evaluation of the MWTWs as previously mentioned in section 3.3.4.

3.5.2 DEKOALE dataset

The ability of πCA and PCA in emphasising $[K^+]$-induced TW variations was tested on the DEKOALE dataset. In addition, the same warping markers were computed from the standard leads II, V4 and V6 to evaluate whether the use of a LSR techniques (either πCA or PCA) improve the performance of the TW morphology markers in following $\Delta[K^+]$ over the standard leads.

In chapter 2, PCA was successfully applied as LSR technique before extracting TW morphology markers and d_w, $\hat{d}_{w,c}$ and d_w^{NL} performance in tracking $[K^+]$ was compared with respect to two TW-based indexes previously reported to be related with $\Delta[K^+]$. As a result, both Spearman's and Pearson's correlation coefficients with $\Delta[K^+]$ were, in median, higher for the time warping based markers than other descriptors. However, πCA was found to be more robust than PCA against noise in other ECG applications [163], supporting the hypothesis that the use of πCA could improve the $[K^+]$-tracking ability of d_w, $\hat{d}_{w,c}$ and d_w^{NL}.

For each marker, two performance metrics were investigated: Pearson's correlation with $\Delta[K^+]$ during the HD and marker deviation from a linear trend in the late post-HD period. In this study, only Pearson's correlation coefficient was investigated since it provides meaningful information about the linear relationship between $\Delta[K^+]$ and the proposed markers.

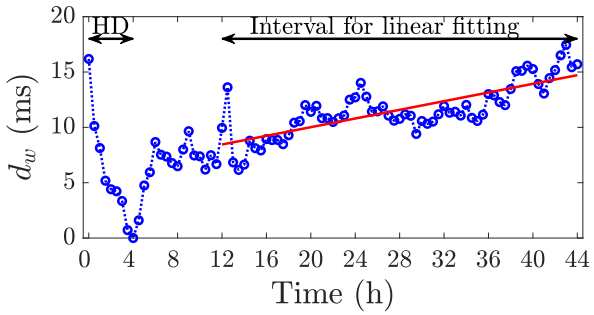

Figure 3.2: Example of linear fitting computation for marker dynamics evaluation in post HD. The red line represents the fitting performed over the PCA-based d_w values (blue dotted line) between the 12-th and 44-th hours after HD. Similar procedure is done for each πCA and PCA based d_w and $\hat{d}_{w,c}$ markers.

Table 3.3: Intra-patient Pearson's (r) correlation coefficients between $\Delta[K^+]$, πC^{B}, πC^{T}, PC, Lead II, V4 and V6 time warping parameters d_w, $\hat{d}_{w,c}$ and d_w^{NL}. Values are expressed as median (IQR).

r	πC^{B}	πC^{T}	PC	II	V4	V6
d_w	0.91 (0.32)	0.90 (0.27)	0.89 (0.35)	0.90 (0.26)	0.86 (0.39)	0.87 (0.29)
$\hat{d}_{w,c}$	0.90 (0.24)	0.90 (0.29)	0.89 (0.25)	0.87 (0.33)	0.86 (0.49)	0.86 (0.27)
d_w^{NL}	0.65 (0.49)	0.75 (0.50)	0.68 (0.52)	0.47 (0.58)	0.56 (0.45)	0.61 (0.47)

Table 3.4: Linear fitting error ϵ estimated across patients in DEKOALE dataset. Values, given as median (IQR) (ms/ms), are for πC^{B}, πC^{T}, PC, II, V4 and V6 leads, for d_w and $\hat{d}_{w,c}$ markers, and estimated from the 12-th to the 44-th hour.

ϵ	πC^{B}	πC^{T}	PC	II	V4	V6
d_w	3.37 (3.22)	2.71 (2.01)	3.21 (3.02)	4.16 (3.28)	3.22 (4.77)	3.68 (3.25)
$\hat{d}_{w,c}$	3.22 (3.13)	2.68 (1.23)	2.51 (2.68)	3.03 (3.04)	2.48 (3.05)	3.26 (2.42)

Table 3.5: Median (IQR) intra-patient Pearson's correlation coefficients in DEKOALE dataset for πC^{B}, πC^{T} and PC based markers evaluated using the whole ECG recordings.

r	PC - πC^{B}	PC - πC^{T}	πC^{B} - πC^{T}
d_w	0.69 (0.56)	0.75 (0.40)	0.87 (0.52)
$\hat{d}_{w,c}$	0.63 (0.53)	0.68 (0.41)	0.78 (0.45)
d_w^{NL}	0.55 (0.48)	0.61 (0.58)	0.60 (0.44)

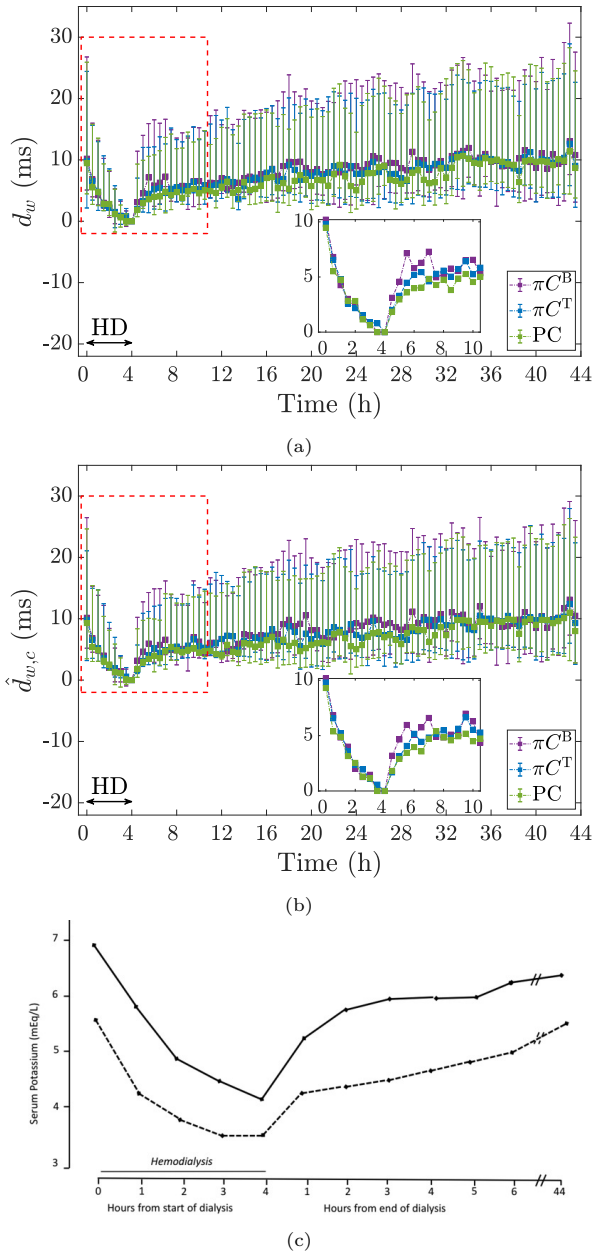

Figure 3.3: Comparison of time trend for d_w and $\hat{d}_{w,c}$ computed applying πCA and PCA and $[K^+]$-recovery curves reproduced from literature. Time dynamic for d_w and $\hat{d}_{w,c}$ computed by applying πC^{B} (purple), πC^{T} (green) and PCA (blue) given as median and IQR is displayed in panel (a) and (b), respectively. Only the first 44 hours were depicted being the average ECG duration in the DEKOALE dataset. A detailed view of the first 10 hours (zoomed rectangle) allows better trend comparison with the $[K^+]$-recovery curves reproduced from [200], panel (c), coming from two different serum-dialysate gradient cases (i.e. the difference between the patient's $[K^+]$ level and the $[K^+]$ concentration in the dialysate liquid) scenarios: 5.8 mmol/L (solid line) and 4.7 mmol/L (dashed line). Note that curves in panel (b) only cover the first 10 hours (4 hours of HD and 6 hours after the HD end) but no values are depicted between the 6-th and the 44-th hour after the HD therapy ends.

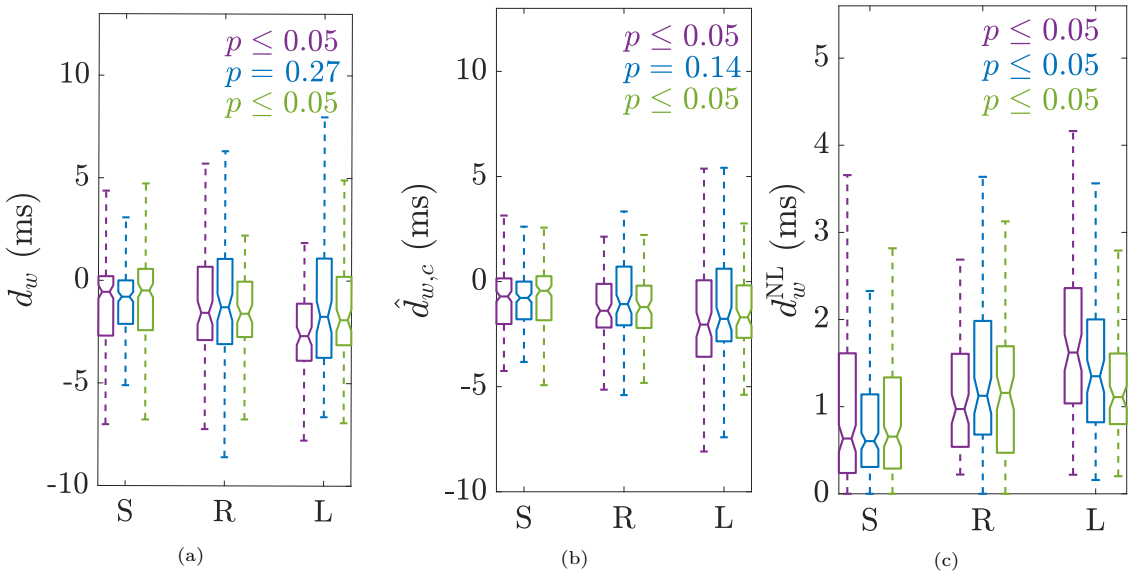

Figure 3.4: Distributions of the warping markers d_w (panel a), $\hat{d}_{w,c}$ (panel b) and d_w^{NL} (panel c) obtained for the BPC dataset. The markers values were grouped by body position: supine (S), right (R) and left (L) and by LSR technique: πC^{B} (purple-coloured boxplots), πC^{T} (blue-coloured boxplots) and PC (green-coloured boxplots). The statistical significance level (p-value, Kruskal-Wallis test) of the differences among the supine, right and left positions for each πC^{B} (purple), πC^{T} (blue) and PC (green) is indicated in each panel. Outliers are not depicted.

Note from Table 2.2 that $[K^+]$ is higher at h_0 than at h_5, a result attributable to the fact that at h_5 all patients were ending a two-day inter-dialysis pause, while at h_0 most of the patients, 27 out of 29, were at the end of a three-day inter-dialysis pause.

Correlation between TW markers and $\Delta[K^+]$

Results from Table 3.3 reveal that d_w and $\hat{d}_{w,c}$ are the descriptors having the highest r median values ($r \geq 0.89$). Also, single-lead-based markers were outperformed by those obtained by applying a LSR technique, PCA or πCA, as already proved in chapter 2. Moreover, πC^{T}-based indices are slightly better correlated with $\Delta[K^+]$ (higher median r and lower deviation as in case of d_w^{NL}). This can be a consequence of the fact that in πC^{B}, the overall ventricular activity is considered to learn the transformations, and then the more energetic QRS complex could had prevailed over the TW. On the other side, πC^{T} learning was fully driven by TW. However, results are still very similar to strongly conclude which LSR technique should be preferred for $\Delta[K^+]$ tracking during the HD period.

Post-HD marker trend and linear fitting error

Throughout the first 10 hours of recording, both d_w, Figure 3.3a, and $\hat{d}_{w,c}$, Figure 3.3b, showed time dynamics similar to $[K^+]$-recovery curve from the literature [199, 200], Figure 3.3c.

After that period, both markers settled on a apparent linear trend, a behaviour in agreement with an expected gradual increase of $[K^+]$ over time in ESRD patients undergoing HD [199, 200]. This led us to conjecture about the deviation from a linear trend, measured by ϵ, as a metric to evaluate the performance of each LSR technique in the interval where no blood samples were collected. Therefore, for a given LSR technique the smaller the ϵ, the more coherent is the measurements across patients of the proposed markers.

The idea of a linear polynomial to fit marker values was already presented by Attia *et al.* [145] to generate a patient specific regression model. Results reported in Table 3.4 suggest that πC^{T}, resulted in the least scattered values, i.e. in more coherent measurements across patients, than the other LSR techniques in the post HD period, confirmed by the small median ϵ and reduced variability being median $2.68 \leq \epsilon \leq 2.71$ and variability $1.23 \leq \mathrm{IQR} \leq 2.01$. πC^{B} and PCA led to similar results with $2.51 \leq \epsilon \leq 3.37$

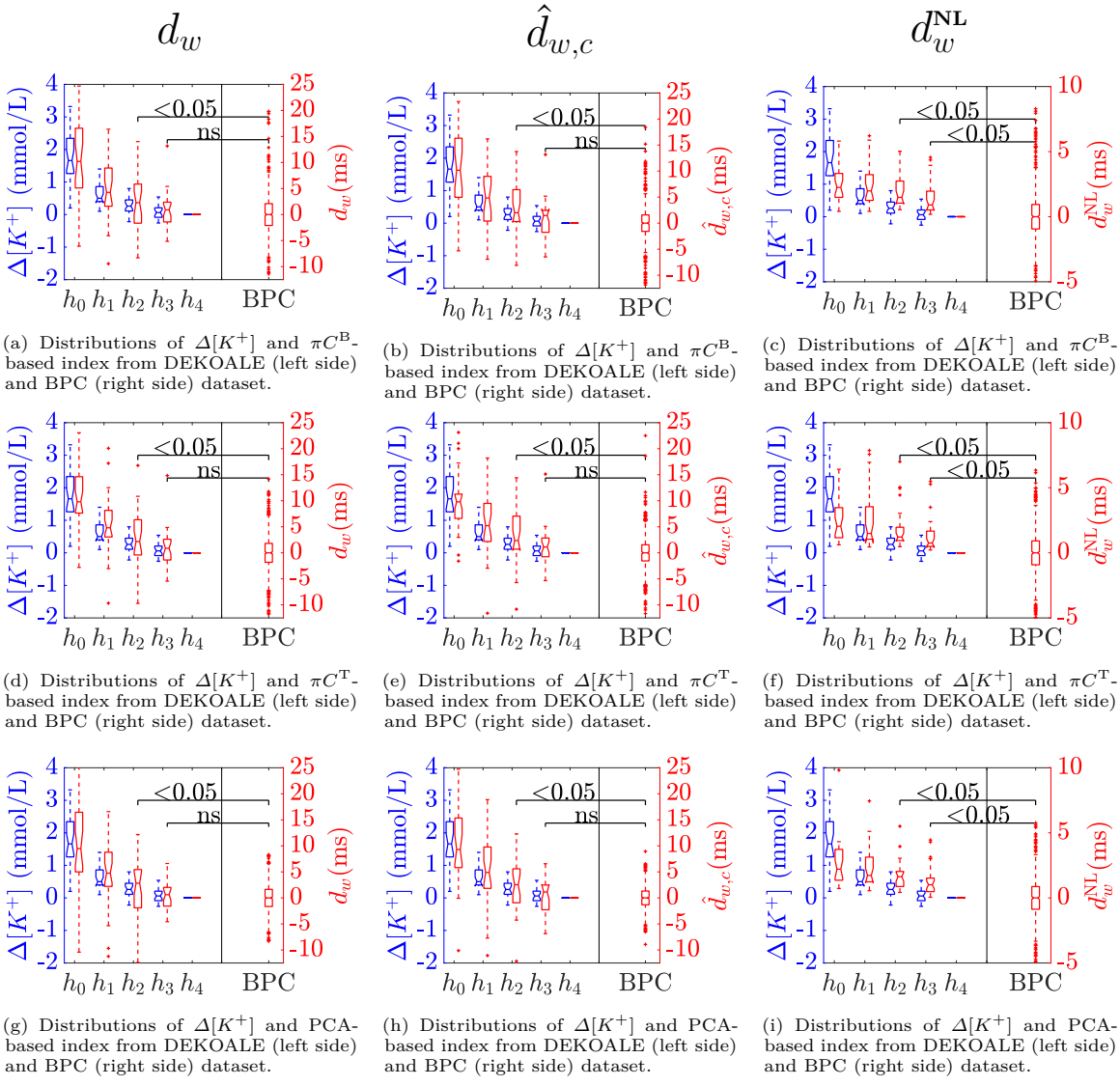

(a) Distributions of $\Delta[K^+]$ and πC^{B}-based index from DEKOALE (left side) and BPC (right side) dataset.

(b) Distributions of $\Delta[K^+]$ and πC^{B}-based index from DEKOALE (left side) and BPC (right side) dataset.

(c) Distributions of $\Delta[K^+]$ and πC^{B}-based index from DEKOALE (left side) and BPC (right side) dataset.

(d) Distributions of $\Delta[K^+]$ and πC^{T}-based index from DEKOALE (left side) and BPC (right side) dataset.

(e) Distributions of $\Delta[K^+]$ and πC^{T}-based index from DEKOALE (left side) and BPC (right side) dataset.

(f) Distributions of $\Delta[K^+]$ and πC^{T}-based index from DEKOALE (left side) and BPC (right side) dataset.

(g) Distributions of $\Delta[K^+]$ and PCA-based index from DEKOALE (left side) and BPC (right side) dataset.

(h) Distributions of $\Delta[K^+]$ and PCA-based index from DEKOALE (left side) and BPC (right side) dataset.

(i) Distributions of $\Delta[K^+]$ and PCA-based index from DEKOALE (left side) and BPC (right side) dataset.

Figure 3.5: Distributions of $\Delta[K^+]$ (blue, scale at the left side of each panel), d_w, $\hat{d}_{w,c}$ and d_w^{NL} markers (red, scale at the right side of each panel) from DEKAOLE dataset are shown in the left side of each panel. In each panel, the rightmost boxplot, includes the zero-mean distribution of markers obtained from the BPC dataset. πC^{B}-based markers are shown in panels (a)-(c), πC^{T}-based markers are in panels (d)-(f) while PCA-based markers are in panles (g)-(i). Mann-Whitney U-test significance level (p-value) between BPC and both h_2 and h_3 of HD are given in each panel, where ns stands for "not significant" (p-value > 0.05). Note that for the first two groups (i.e. HD onset h_0, and h_1) p-values were always lower than 0.05, hence, not displayed. Red "+" indicate outliers.

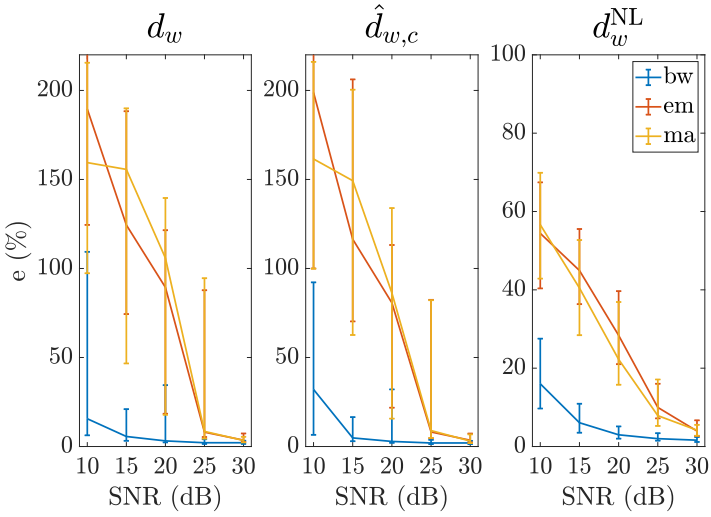

(a) Relative error curves for πC^{B}-based time warping

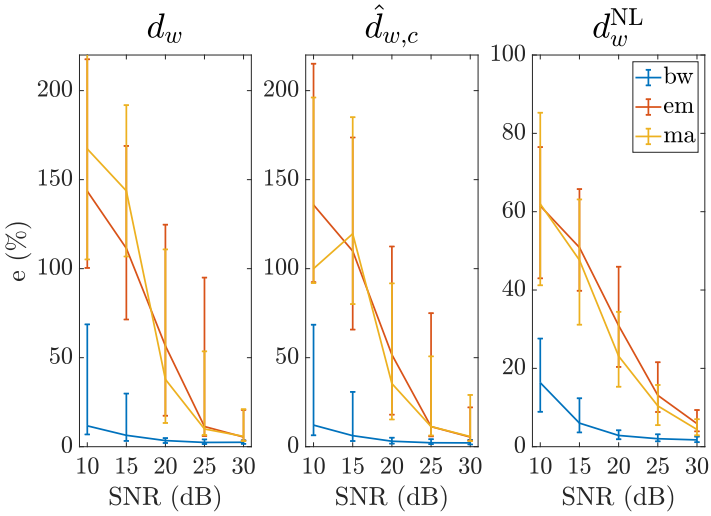

(b) Relative error curves for πC^{T}-based time warping

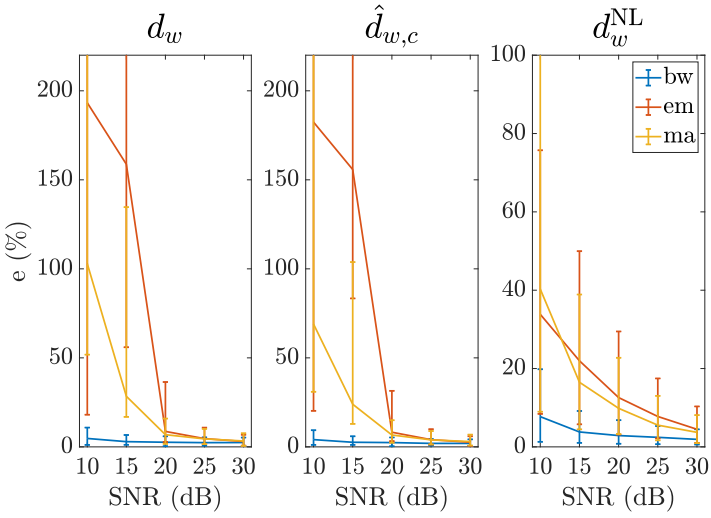

(c) Relative error curves for PCA-based time warping

Figure 3.6: Relative error e distributions evaluated between the reference d^{NtoC} and estimated d^{NtoN} under the presence of additive bw (blue line), em (orange line) and ma (yellow line) noises at different SNRs. Median and IQR from the 100 runs were given for each SNR.

and variability $2.68 \leq \text{IQR} \leq 3.22$. Finally, the standard lead analysis was those with the biggest dispersion being the median $2.48 \leq \epsilon \leq 4.16$ and $2.42 \leq \text{IQR} \leq 4.77$.

From Table 3.5, it can be observed that the highest correlation between markers was obtained when comparing πC^{B} and πC^{T} (last column), probably as a consequence of the fact that both LSR techniques use the same maximisation criteria. However, this test just measures agreement between markers but not with $\Delta[K^+]$, preventing us from taking further conclusions from it.

Correlations with $\Delta[K^+]$ and linear fitting error metrics confirmed that πC^{B}, πC^{T} and PCA-based markers outperform standard lead estimations, and it may be concluded that πC^{T} is the most consistent LSR technique in terms of trend dispersion (post-HD period), and r (during the HD therapy). In Holter where 12 leads are not available but a reduced number, the πC^{T} can be still applied even though the capacity to extract beat-to-beat periodicity would be reduced and further works are needed to evaluate the degree of the reduction. The lower limit in performance would be the here reported study in standard single-lead analysis as described in Chapter 2 (see Table 2.3) where we will still get markers with better correlation with $\Delta[K^+]$ than those reported in the literature (i.e. $T_{S/A}$ and T_w).

3.5.3 BPC dataset

The relative position of the heart electric axis with respect to the surface electrodes changes with body position, influencing the shape of the ECG waveform [205, 209] and, consequently, the TW morphology markers measured on the signal. We tested the proposed LSR techniques to figure out if any of them resulted in higher marker robustness against BPC. The analysis of marker distributions, Figure 3.4, evidences that all markers are affected by BPC.

For all LSR techniques, the S position showed the smallest median and IQR values as a result of the election of the warping reference in S position, see Table 3.1, followed by R and L. However, only πC^{T} showed non-significant differences in Kruskal-Wallis test between d_w and $\hat{d}_{w,c}$ when computed and compared in different body positions suggesting that πC^{T} is the least affected by the patient's posture.

3.5.4 Comparing results from DEKOALE and BPC datasets

To elucidate up to what extend d_w, $\hat{d}_{w,c}$ and d_w^{NL} can capture waveform alterations generated by $\Delta[K^+]$ remaining no-significantly affected by concomitant BPC, markers from ESRD patients undergoing HD were compared with respect to those from BPC dataset. Patients in HD therapy remained still (usually seated) during the whole session, ensuring that no marker alteration occurred due to changes in the posture. Conversely, in the BPC dataset, where healthy subjects were enrolled, the ECG waveform and thus marker values alterations were mainly attributed to postural changes.

The comparison between results from two datasets was necessary since $[K^+]$ values were not acquired for the BPC dataset. This test meant to evaluate the behaviour of the same markers in two different scenarios, i.e. $[K^+]$ changes and BPC. Therefore the recording duration did not play a relevant role provided that it ensured the correct assessment of the MWTW as detailed in section 3.3.4.

According to Figure 3.5, significant differences can be observed for any given LSR technique and marker when comparing distributions from h_0, h_1, h_2 and BPC, probably due to the $[K^+]$ being outside the normal range (considered to be in h_4, Table 2.2) thus being the main factor in the ECG waveform shaping. On the contrary, as HD final stage approaches, h_3, the value of $\Delta[K^+]$ reduces and the ECG waveforms returns close to shapes at reference in h_4. At h_3, all markers computed in the DEKOALE dataset, but d_w^{NL}, showed median values similar to those obtained in the BPC signals. This different behaviour of d_w^{NL} could be attributed to the fact that a postural changes generate a rotation of the electrical axis, not introducing any non-linearity across time behaviour to be captured by d_w^{NL}, therefore making it insensitive to BPC. No preferential behaviour in this respect is observed as a function of the chosen LSR.

3.5.5 ECG simulation

Synthetic ECG signals with controlled noise contamination, emulating recordings from DEKOALE dataset, were used to test the robustness of the d_w, $\hat{d}_{w,c}$ and d_w^{NL} against noise for the different LSR

techniques. Noise signals were taken from real Holter recordings and forced to be spatially correlated as in the 12-lead recordings [217].

According to Figure 3.6, for a given SNR and for any LSR technique, em and ma noises resulted in the highest e, possibly due to their spectra are comparable to that of the ECG, and so preprocessing is less efficient. Because of that, em and ma filtration was not as effective as bw which showed the smallest e median and IQR.

However, a general decreasing error trend with increasing SNR can be observed. Moreover, these graphs would confirm that πCA outperforms PCA for low SNR (10 dB and 15 dB) as hypothesised. In addition, it appears that πC^{T} has median e smaller than πC^{B} in the majority of the proposed markers. This outcomes can be attributable to the fact that the QRS complex, despite having larger SNR, has different spatial distribution than the TW and thus favouring πC^{T} spatial transformation. Finally, no clear advantages in using πCA over PCA can be appreciated for high SNR (i.e. SNR $>$ 20 dB).

Nevertheless, these results would confirm our hypothesis that πCA performs better than PCA for low SNR values as it was evidenced in [163] for TW alternans detection.

3.5.6 Clinical Significance

According to results from DEKOALE dataset, markers extracted from a TL outperform those obtained from standard single leads. In particular, πC^{T} appears to be the most suitable LSR technique to extract the TW morphology marker best correlated with $\Delta[K^+]$, thus allowing a more reliable continuous monitoring of ESRD patients undergoing HD during the HD as well as in the post-HD period.

Even though it is technically possible to continuously monitor the markers, it can also be possible to restrict the ESRD patients monitoring just to some specific points such as one per hour or any other periodicity that may be considered suitable for clinical evaluation. This will allow to stop the recording in the intermediate periods with the related advantages in terms of battery saving, information transmission, data storing, etc.

Outcomes from the BPC dataset revealed that the proposed TW time warping markers to quantify morphology changes are not significantly affected by the subject's posture when evaluated at πC^{T} TL. This suggests that πC^{T} should be the preferred TL for daily life continuous monitoring of ESRD patients undergoing HD therapy. Moreover, the marker reflecting TW nonlinear morphological changes, d_w^{NL}, is able to still capture relevant information describing small $\Delta[K^+]$ that are not affected by concomitant BPC. These results can be of great interest when choosing a marker to robustly monitor $[K^+]$ in ESRD patients undergoing HD therapy $[K^+]$ in daily life [108].

Finally, findings from ECG simulation indicated that at low SNR, πC^{T}-based markers are the most robust against ECG noises meaning that πC^{T} is the most suitable LSR to extract relevant multilead TW morphology information from noisy records (i.e. Holters) in non-invasive ambulatory $[K^+]$ monitoring of ESRD patients undergoing HD therapy.

3.5.7 Limitations

Despite the encouraging results, several limitations deserve to be mentioned. First, a direct correlation study between markers and $\Delta[K^+]$ was only possible during the HD therapy since no $[K^+]$ samples were collected in the post-HD period until the 48-th h. In other words, an explicit relation between d_w, $\hat{d}_{w,c}$ and d_w^{NL} and $\Delta[K^+]$ in the post-HD period could not be assessed nor inferred from the linear fitting error ϵ since there is no certainty that $[K^+]$-recovery trend is exactly linear. However, $[K^+]$ dynamics tend to appear slow, gradual and monotonic [199, 200], making the deviation from a linear trend still a plausible indirect indicator to assess the marker robustness. Other regression types could be further investigated, together with studies including regular blood samples extraction during the post-HD period.

Second, as mentioned in chapter 2, the sample size in DEKOALE dataset is smaller than the study population in similar investigations [108]. Thus, even if the usage of πC^{T} as LSR technique is a step toward robust TW morphology feature extraction from the ECG, it needs to be validated in larger cohorts to be finally translated to clinical practice.

Third, the BPC series only contained lying-based changes, thus excluding daily-life postural changes (e.g. lying-seated-standing), representing a limitation for the generalization of the results. However, we believe that this limitation is attenuated when considering the fact that the analysed postural changes can be considered as the most strenuous in terms of heart rotations with respect to electrodes positions [205].

Fourth, times of meal and medication intake were not registered in the DEKOALE. This means that it was not possible to distinguish between $\Delta[K^+]$ due to the ESRD pathology itself or, for instance, due to insulin spikes that can modify intracellular concentration of $[K^+]$ [95]. Different issue is the dependence of $\Delta[K^+]$ with the circadian rhythm [218] as can be observed in the example in Figure 3.2. However, no special attention to circadian rhythm has been paid in the present study. All the above mentioned could be a limitation of the analysis performed in the post HD period; but since the interest here is in the long term trends transients, modifications as those resulting from food or medication intake are most likely no to affect the global trend. In addition, a direct correlation between markers and $\Delta[K^+]$ was computed only during the hours of the HD therapy thus when the patients were not supposed to be having a meal nor taking medication other than those inside the dialysis fluid. Nevertheless, further studies are need to assess how meals, medications and circadian rhythm could affect the proposed markers of potassium changes.

Finally, in addition to producing TW changes generated by $[K^+]$ variations, HD can trigger myocardial ischaemia events [203, 219, 220], which could also affect the TW morphology and the marker validity.

3.6 Conclusion

Results from this chapter highlight the advantages of applying one-beat-period πCA, and, in particular, πC^{T} rather than PCA as LSR technique before deriving TW morphology markers to monitor $[K^+]$ variations in ESRD patients undergoing HD therapy. The main advantages concern a greater robustness against BPC and noise, improving the accuracy of TW time warping based markers in monitoring $\Delta[K^+]$.

The πC^{T}-derived d_w and $\hat{d}_{w,c}$ markers seem to be the most suitable (better correlated) for $[K^+]$ monitoring in both HD therapy and recovery periods. Nevertheless, d_w^{NL}, computed by using either πCA or PCA, appears to be the least affected by postural changes, offering a new starting point when evaluating $[K^+]$-driven TW morphological changes.

CHAPTER

4

Regression Models for Personalised and Non-Invasive Blood Potassium Estimation

4.1 Introduction

In chapter 3 two LSR techniques, πCA and PCA, were tested as step previous to TW time-warping analysis for extracting markers able to monitoring $[K^+]$ variations. In particular, two different implementation of πCA were proposed: by exploiting the complete QRST complex periodicity, πC^{B}, or just restricting to the TW, πC^{T}. As a result of this analysis, d_w and $\hat{d}_{w,c}$ were the markers showing, in median, the highest Pearson's correlation with $\Delta[K^+]$. Moreover, πC^{T} presented higher robustness against noise than PCA and πC^{B}, making it the most suitable LSR technique for $\Delta[K^+]$ tracking during the HD session, as well as in the post therapy monitoring before the next HD session. Nevertheless, a quantitative relation between these TW morphological parameters derived from ECG analysis and $\Delta[K^+]$ has not yet been established for clinical use, which would allow a noninvasive measurement of $\Delta[K^+]$ value.

The direct assessment of a marker as $[K^+]$ surrogate by Pearson's correlation analysis implies the assumption of a linear relation between them. However, previous works have reported that the reconstruction of $[K^+]$ from the ECG significantly improves by employing a quadratic regression [141]. This result is compatible with the findings from chapter 3, where a non-linear correspondence between $\Delta[K^+]$ and the TW time warping markers d_w and $\hat{d}_{w,c}$ (purple and green boxplots, respectively, in Figure 4.1) was observed. Therefore, the analysis in the present chapter was performed under the hypothesis that using patient-specific polynomial models based on TW time warping-derived markers can provide better quantitative assessment of $\Delta[K^+]$. Thus, the aim of this study is to derive and to evaluate polynomial sensing models to estimate $\Delta[K^+]$ by using πC^{T}-based markers, d_w and $\hat{d}_{w,c}$. As a reference, a patient-specific linear model is also estimated for each marker.

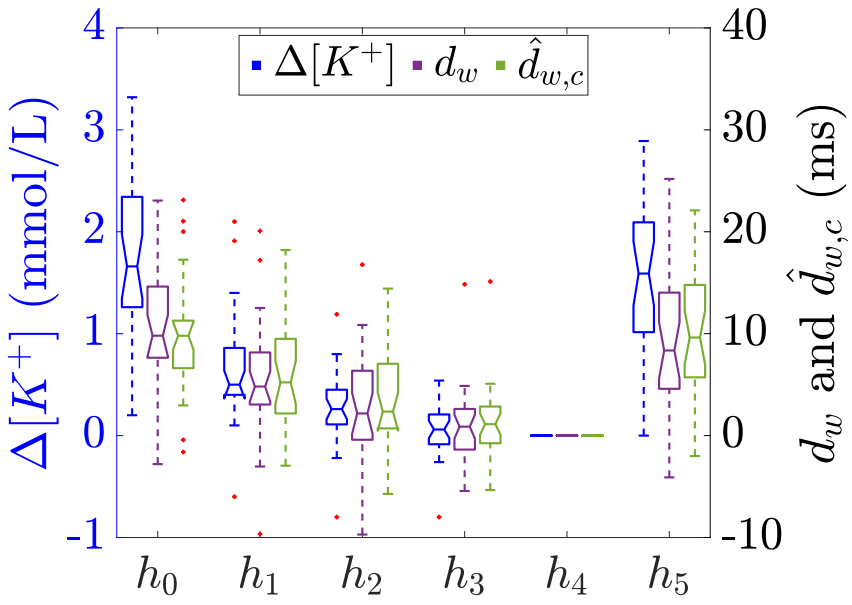

Figure 4.1: Distribution of $\Delta[K^+]$ and πC^{T}-based markers in DEKOALE dataset. Boxplots in blue shown the distribution of $\Delta[K^+]$ while in purple and in green are those for d_w and $\hat{d}_{w,c}$, respectively, computed at each blood sample extraction from h_0 to h_5 (see Figure 2.1). Red "+" denotes outliers. Figure from [221].

4.2 Materials and Methods

4.2.1 Study population

In this chapter, ECG signals from DEKAOLE dataset (section 2.2) were analysed.

4.2.2 ECG preprocessing and single lead analysis

As described in section 2.3.1, preprocessing of ECG recordings included baseline wander removal at 0.5 Hz in each lead and low-pass filtration to remove power-line noise and to attenuate muscular activity. Then, QRS complexes were detected and TW delineated using the wavelet-based delineation previously mentioned in section 2.3.2. The different steps from the ECG acquisition to the $[K^+]$ regression models construction are summarised in the block diagram presented in Figure 4.2.

4.2.3 Spatial lead reduction by periodic component analysis

As in chapter 3, πCA was applied with a one-beat periodicity to maximise the TW beat-to-beat periodic components on the transformed signal. Then, for each ECG, a transformation matrix $\mathbf{\Psi}_{\pi CA}$ was estimated as detailed in section 3.3.3, and applied to the eight independent standard leads. Now, by ordering the TL inversely to their associated eigenvalue, the most beat-to-beat periodic components appear projected onto the first component, $\pi C^{\mathrm{T}}1$, which was selected for subsequent analysis.

4.2.4 Warping-Based TW morphology markers

All TW from $\pi C^{\mathrm{T}}1$ were further low-pass filtered at 20 Hz using a 6-th Butterworth filter to remove remaining out-of-band frequency components. TWs in 2-min wide windows centered around the 5-th minute and 35-th minute of each available hour were selected and a MWTW was computed in each window (see section 2.3.8).

Finally, the two TW morphology parameters, d_w and $\hat{d}_{w,c}$, were computed by comparing each MWTW with respect to a reference MWTW, selected at the end of the HD session, resulting in relative markers to

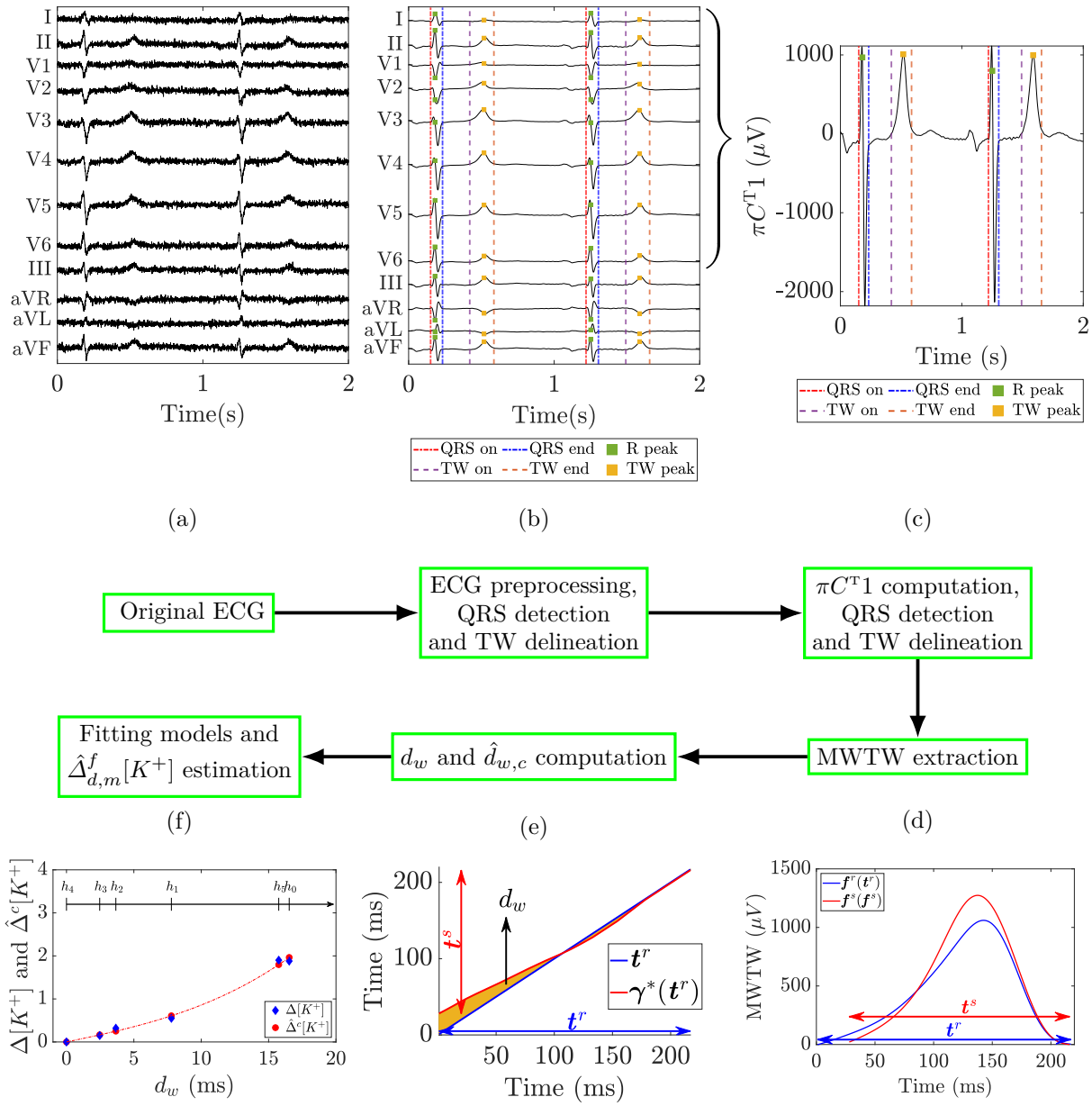

Figure 4.2: Flow chart showing the main steps from ECG acquisition to the evaluation of personalised $\Delta[K^+]$ regression models. Panel (a) shows an example of an ECG (the independent leads I, II, V1 to V6 are depicted) obtained from one of the patients in the DEKAOLE dataset (see section 2.2). In panel (b) is the resulting ECG after performing the preprocessing described in section 2.3.1. In panel (c) is depicted the transformed $\pi C^{\mathrm{T}}1$ signal with both QRS complexes and TW are detected and delineated as detailed in section 2.3.2. From 2-min wide windows, a MWTW (panel (d)) is extracted and TW morphology markers d_w and $\hat{d}_{w,c}$ (panel (e)) are computed as detailed in section 2.3.6. Finally, in panel (f) is an example of fitting model for $\hat{\Delta}^f_{d,m}[K^+]$ estimation, evaluated as in section 4.2.6. In this particular case, a cubic model with $m = a$ is presented.

the reference point at the end of HD (h_4 in Figure 2.1). A detailed description of d_w and $\hat{d}_{w,c}$ mathematical derivation can be found in section 2.3.6.

4.2.5 Blood potassium concentration variations

The two proposed descriptors, measured along time, have been associated with the corresponding relative variations in $[K^+]$ with respect to the $[K^+]$ at the reference point (h_4). The $\Delta[K^+]$ values were computed as in eq. (2.26) in section 2.3.9.

4.2.6 Marker fitting models for $\Delta[K^+]$ estimation

For a given patient p, the relationship between the marker $d \in \{d_w, d_{w,c}\}$ and $\Delta[K^+]$ measured along time was modelled by means of a linear (l), quadratic (q), and cubic (c) regression models for each patient to noninvasively calculate $\Delta[K^+]$ values, according to the following models:

$$\hat{\Delta}^l_d[K^+](h_i) = \alpha_l\, d(h_i), \tag{4.1}$$

$$\hat{\Delta}^q_d[K^+](h_i) = \alpha_q\, d(h_i) + \beta_q\, d^2(h_i), \tag{4.2}$$

$$\hat{\Delta}^c_d[K^+](h_i) = \alpha_c\ d(h_i) + \beta_c\ d^2(h_i) + \gamma_c\ d^3(h_i), \tag{4.3}$$

respectively, which are linear in the coefficients and nonlinear in the markers in case of eq. (4.2) and eq. (4.3). The coefficients α_l, α_q, β_q, α_c, β_c, and γ_c were estimated for each patient p and marker d by using a least square regression analysis between $\hat{\Delta}[K^+]$ and $\Delta[K^+]$ values. For each patient and marker, the parameters of the three models were estimated with two different approaches: (i) By using all the available $\Delta[K^+]$ values ("$m = a$") and (ii) by adopting a leave-one-out cross validation ("$m = o$") by excluding the h_i-th $\Delta[K^+](h_i)$ value from the training-set and evaluating the prediction error at this h_i-th point, repeating this for all possible h_i exclusions.

Finally, to avoid physiologically meaningless $\hat{\Delta}_d[K^+]$ trends, the three models in eq. (4.1)–(4.3) were computed with a constrained parameter estimation in order to guarantee a monotonically increasing relationship between $\hat{\Delta}[K^+]$ and d, as physiologically expected and corroborated by the marker trend evolution in Figure 4.1 in this chapter and in Corsi *et al.* [141] in Figure 2 and 4. That was implemented as:

$$\frac{\partial \hat{\Delta}_d[K^+]}{\partial d} \geq 0, \tag{4.4}$$

which for positive values of the marker, $d > 0$, implies $\alpha_l \geq 0$, $\alpha_q \geq 0$, $\beta_q \geq 0$, $\alpha_c \geq 0$, $\beta_c \geq 0$, and $\gamma_c \geq 0$. The case with $d < 0$ is anecdotal, see Figure 4.1, and most likely is due to outliers, since they do not follow physiological interpretations of TW narrowing with increased potassium.

4.2.7 Statistical analysis

Spearman's rank and Pearson's correlation coefficients (ρ and r, respectively) were used for correlation analyses between $\Delta[K^+]$ and $\hat{\Delta}^f_{d,m}[K^+]$, where $f \in \{l, q, c\}$ denotes the fitting model, $d \in \{d_w, \hat{d}_{w,c}\}$ the TW morphology parameter and $m \in \{a, o\}$ the estimation method. This analysis gives information about both the monotonic relation and the strength of the association between each modelled TW morphology parameter and $\Delta[K^+]$, thus providing a more complete characterisation. In addition, for each patient p and hour h_i, an estimation error $e^f_{d,m}(p, h_i)$ was computed as:

$$e^f_{d,m}(p, h_i) = \left| \hat{\Delta}^f_{d,m}[K^+](p, h_i) - \Delta[K^+](p, h_i) \right| \tag{4.5}$$

where $i \in \{0, 1, 2, 3, 5\}$ is the set of hours where the computation of the estimation error is meaningful. Note that h_4 is the reference point where both $\Delta[K^+]$ and $\hat{\Delta}^f_{d,m}[K^+]$ are equal to zero and therefore it is excluded from error computation to avoid a biased error evaluation. The value $\hat{\Delta}^f_{d,a}[K^+](p, h_i)$ represents the estimation at time h_i when training is done including all available h_i hours values from the corresponding patient, while $\hat{\Delta}^f_{d,o}[K^+](p, h_i)$ represents the estimate at hour h_i when all but the h_i-th point of the patient are used in the training. Results are given as median (IQR).

4.3 Results

In Figure 4.3 are the distributions of $\Delta[K^+]$ values from blood samples and from the implemented regression models for each hour h_0 to h_5. In each panel, the real $\Delta[K^+]$ from blood samples is shown in blue, while the black and the red boxplots represent $\hat{\Delta}^f_{d,m}[K^+]$ for $m = a$ and $m = o$, respectively. Panels (a) and (d) show results for linear models $f = l$; panels (b) and (e) show the quadratic and panels $f = q$; and panels (c) and (f) show the cubic model $f = c$.

Boxplots in Figure 4.4 show the estimation error $e^f_{d,m}(p, h_i)$ distributions, sorted by hours h_i, using the linear (Figure 4.4a and Figure 4.4d), the quadratic (Figure 4.4b and Figure 4.4e) and the cubic (Figure 4.4c and 4.4f) models. In addition, the aggregated distribution for all hours is presented with the label (ALL). The widest error distributions are obtained for hours h_0 and h_5, whose median and IQR are given in Table 4.1. These time points are of great interest since: (i) the samples are the furthest from the reference (h_4) and (ii) when they are estimated by using the leave-one-out (m=o) approach they do not have any temporarily close sample before (i.e. in case of h_0) and/or after (i.e. in case of h_5) as opposed to h_1, h_2 and h_3; this together with the fact that their associated marker values are also the farthest from the rest, Figure 4.1. Therefore, it seemed worthy performing a detailed hour-based error analysis.

The median and IQR values of intra-patient Spearman's (ρ) and Pearson's (r) correlation coefficients, computed between $\Delta[K^+]$, and $\hat{\Delta}^f_{d,m}[K^+]$, are given in Table 4.1. The same table also displays the median and IQR values of the errors $e^f_{d,m}(p, h_i)$, pooling together all patients and all blood extractions (ALL), and segregated for hour h_0 and h_5.

An example of cubic modelling results for a given patient with and without parameter constriction for monotonic $\hat{\Delta}^c_{d_w,o}[K^+]$ behaviour with d is presented in Figure 4.5. Results are given for the case with no restrictions on $\{\alpha_c, \beta_c, \gamma_c\}$ (Figure 4.5a); by imposing $\alpha_c \geq 0$ (Figure 4.5b); and by using a full constrained model ($\alpha_c \geq 0$, $\beta_c \geq 0$, $\gamma_c \geq 0$) (Figure 4.5c).

Table 4.1: Intra-patient ρ, r, $e^f_{d,m}$ - either when pooling all patients and blood samples together (ALL) or specifically for h_0 and h_5 - evaluated between $\Delta[K^+]$ and $\hat{\Delta}^f_{d,m}[K^+]$, expressed as median (IQR), for each model $f \in \{l, q, c\}$, marker $d \in \{d_w, \hat{d}_{w,c}\}$, and estimation rule $m \in \{a, o\}$.

d	f	m	ρ	r	$e^f_{d,m}$		
					ALL	h_0	h_5
d_w	l	a	0.83 (0.33)	0.86 (0.35)	0.30 (0.48)	0.28 (0.77)	0.29 (0.55)
		o	0.77 (0.48)	0.76 (0.47)	0.38 (0.61)	0.56 (1.10)	0.45 (0.66)
	q	a	0.83 (0.36)	0.91 (0.29)	0.22 (0.34)	0.24 (0.58)	0.27 (0.49)
		o	0.83 (0.49)	0.77 (0.51)	0.38 (0.59)	0.64 (1.15)	0.63 (0.60)
	c	a	0.89 (0.35)	0.92 (0.27)	0.21 (0.34)	0.23 (0.37)	0.30 (0.54)
		o	0.83 (0.49)	0.79 (0.61)	0.39 (0.72)	0.64 (1.24)	0.69 (0.75)
$\hat{d}_{w,c}$	l	a	0.83 (0.31)	0.88 (0.34)	0.27 (0.50)	0.26 (1.03)	0.31 (0.54)
		o	0.80 (0.44)	0.81 (0.34)	0.40 (0.63)	0.54 (1.11)	0.50 (0.59)
	q	a	0.83 (0.35)	0.90 (0.27)	0.21 (0.36)	0.25 (0.73)	0.27 (0.50)
		o	0.80 (0.53)	0.77 (0.39)	0.41 (0.67)	0.57 (1.45)	0.71 (0.61)
	c	a	0.83 (0.31)	0.90 (0.25)	0.20 (0.39)	0.25 (0.67)	0.23 (0.52)
		o	0.80 (0.49)	0.72 (0.45)	0.43 (0.81)	0.77 (1.25)	0.76 (0.80)

4.4 Discussion

In this chapter, ECG signals from ESRD patients undergoing HD therapy were analysed, and two TW morphology indexes, d_w and $\hat{d}_{w,c}$, previously reported to have a strong correlation with $\Delta[K^+]$ (see

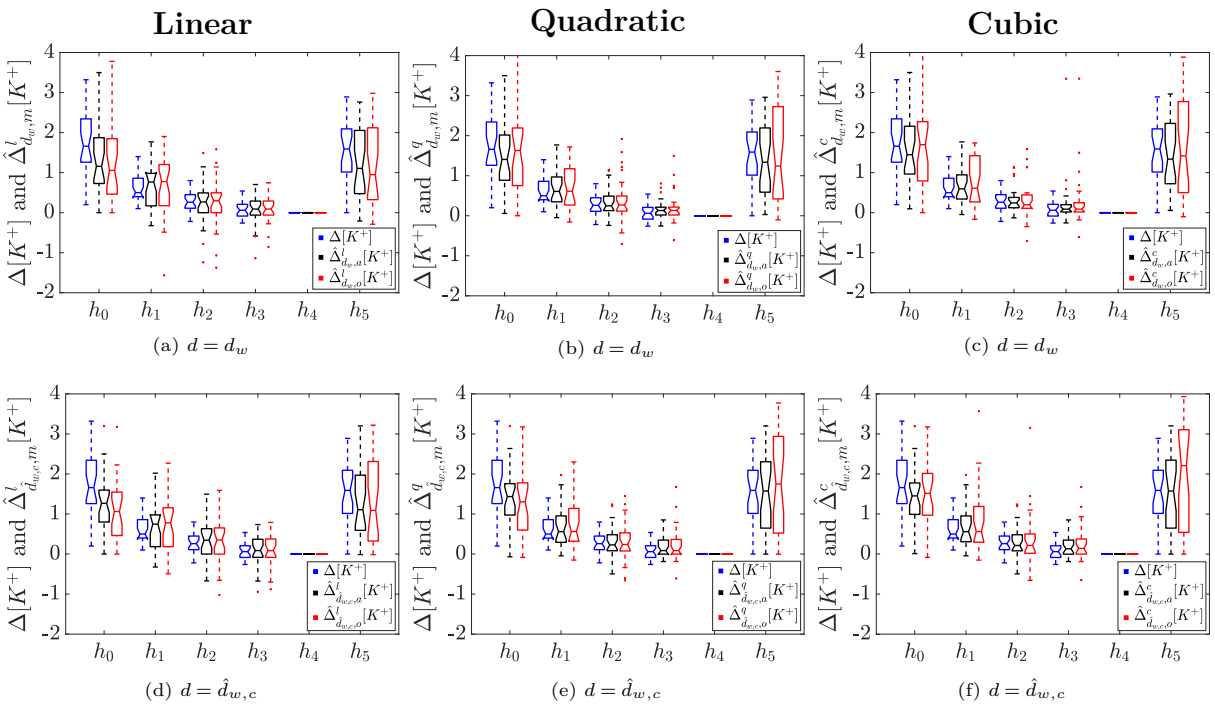

(a) $d = d_w$ (b) $d = d_w$ (c) $d = d_w$

(d) $d = \hat{d}_{w,c}$ (e) $d = \hat{d}_{w,c}$ (f) $d = \hat{d}_{w,c}$

Figure 4.3: Distributions of $\Delta[K^+]$ values from blood samples and from regression models for each hour h_0 to h_5. In each panel, the real $\Delta[K^+]$ from blood samples are in blue, while the black and the red ones represent $\hat{\Delta}^f_{d,m}[K^+]$ for $m = a$ and $m = o$, respectively. Panels (a) and (d) show results for linear models $f = l$; panels (b) and (e) show the quadratic and panels $f = q$; and panels (c) and (f) show the cubic model $f = c$. Red "+" denotes outliers.

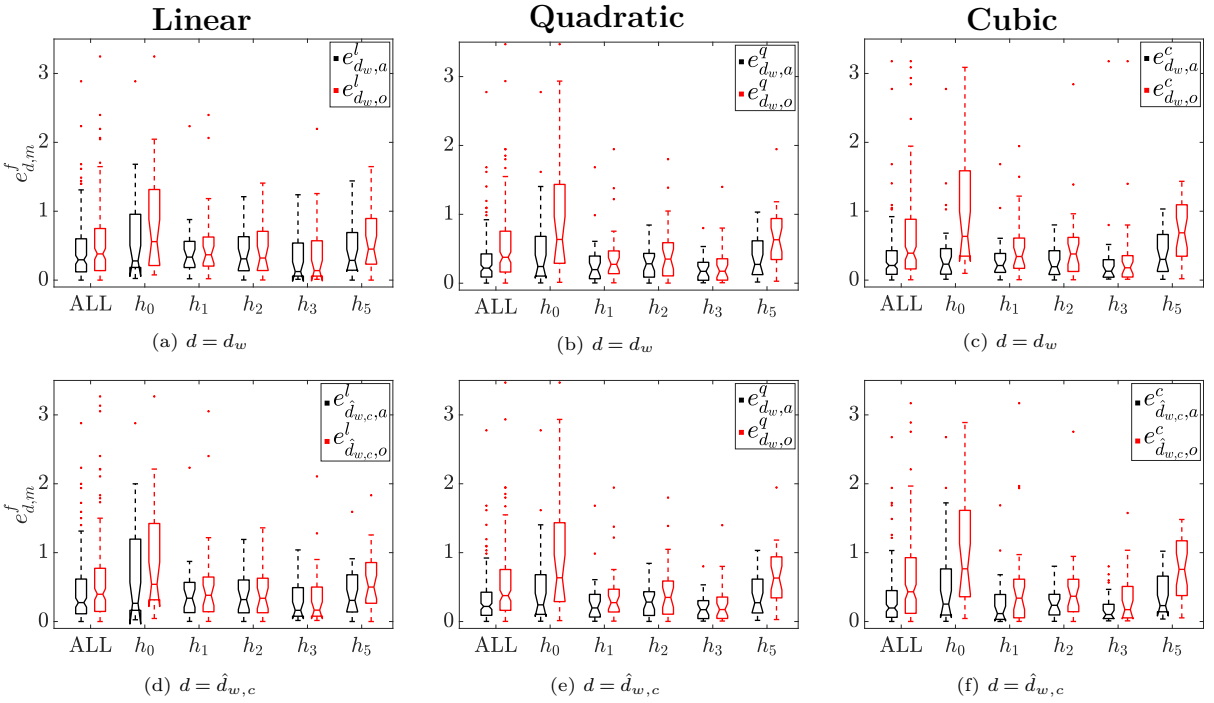

(a) $d = d_w$ (b) $d = d_w$ (c) $d = d_w$

(d) $d = \hat{d}_{w,c}$ (e) $d = \hat{d}_{w,c}$ (f) $d = \hat{d}_{w,c}$

Figure 4.4: Estimation error ($e^f_{d,m}(p,h_i)$) distributions across patients for each hour h_i and when pooling all samples together (ALL). Panels (a) and (d) show results for linear models $f = l$; panels (b) and (e) show the quadratic and panels $f = q$; and panels (c) and (f) show the cubic model $f = c$. Black boxplots represent the errors in $m = a$ while the red ones represents error in case of $m = o$. Red "+" denotes outliers.

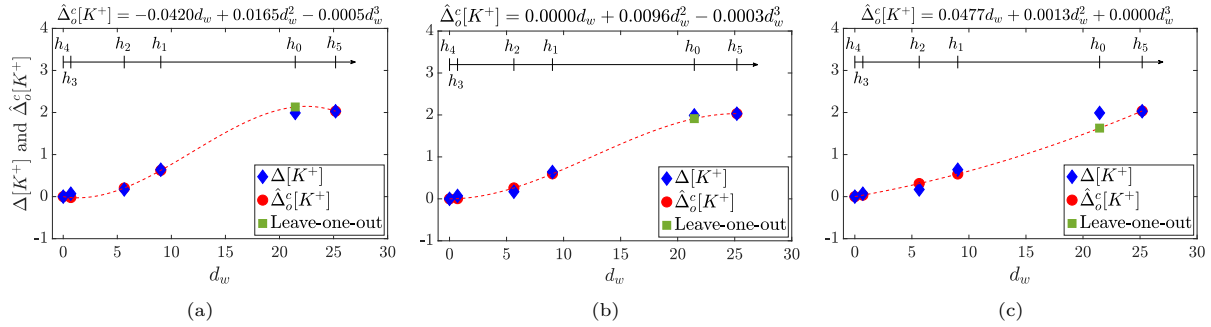

Figure 4.5: Examples of cubic regression models computation for a given patient by imposing different parameter restrictions for leave-on-out cross-validation method. The model obtained without restrictions on $\{\alpha_c, \beta_c, \gamma_c\}$ is in panel (a), while those from imposing $\alpha_c \geq 0$, or full constrained model are presented in panels (b) and (c) respectively. In each panel: the red dotted line represents the model being corresponding equations reported above the graph; the blue diamonds represent measured $\Delta[K^+]$ values at the hours $\{h_0, h_1, h_2, h_3, h_4, h_5\}$; while red dots are the estimated $\hat{\Delta}^c_{d_w,o}[K^+]$ corresponding to the computed d_w used in the training set and computed at $\{h_1, h_2, h_3, h_4, h_5\}$; the green square is the estimated $\hat{\Delta}^c_{d_w,o}[K^+]$ corresponding to the d_w at h_0, the hour excluded from the training set in this example, and then the one with higher risk for error in the estimation. Notice that only full set of parameters forced to be positive result in a monotonic, physiologically plausible, function.

chapter 3), were extracted. Then, we proposed and compared, the use of linear, quadratic and cubic regression models for $\Delta[K^+]$ estimation from d_w and $\hat{d}_{w,c}$ markers. The performance of each model was evaluated through Spearman's and Pearson's correlation coefficients of the estimated $\hat{\Delta}[K^+]$ with respect to actual $\Delta[K^+]$ values and through hourly-based absolute estimation errors. The results on ESRD patients undergoing HD therapy here reported showed that quadratic and cubic regression models could be advantageously used to quantitatively estimate $\Delta[K^+]$ and could, therefore, be an effective tool for remote, frequent and noninvasive monitoring of those patients.

4.4.1 Correlation coefficients reveal over-fitting in $m = a$ approach

Similarities in the distributions of real $\Delta[K^+]$ and $\hat{\Delta}^f_{d,m}[K^+]$ for every markers and regression model can be observed in Figure 4.3, a results, this, confirmed by the Spearman's correlation coefficient (ρ) between measured and estimated variations in $[K^+]$ as reported in Table 4.1. Indeed, similar ρ median values were found across the three models, being 0.06 the highest median increment when moving from a linear to a cubic model for $d = d_w$ in m=a and, thus, denoting an analogous monotonic relationship between real $\Delta[K^+]$ and estimated values ($\hat{\Delta}^f_{d,m}[K^+]$).

However, an improvement can be appreciated when comparing Pearson's correlation coefficient (r) evaluated in the three models, being the IQR reduced in $d = d_w$ and $m = a$ by 0.06 and 0.08 when comparing the quadratic and cubic models, respectively, with respect to the linear model. Similar considerations can be made for $d = \hat{d}_{w,c}$. This is an expected outcome since the models here proposed were designed to avoid distorting the original monotonic increasing relationship between $\Delta[K^+]$ and the ECG derived markers, but only to adjust for the linear/non-linear relationship between them.

Nevertheless, the overall performance decreases considerably when the leave-one-out method, $m = o$, was used, being the median r lower and the IQR wider than in $m = a$. Also, for both d_w and $\hat{d}_{w,c}$ in $m = o$, a remarkable increase in the IQR can be observed when comparing linear and cubic models: from 0.47 to 0.61 for the first marker and from 0.34 to 0.45 for the second one. Overall, these findings seem to suggest that the cubic model does not provide any additional advantages to the linear or quadratic models in estimating $\Delta[K^+]$ using the leave-one-out approach. Therefore, the results we observed for $m = a$ could potentially be affected by over-fitting.

Another interesting observation can be made when comparing d_w with $\hat{d}_{w,c}$ in terms of r: for the linear model and $m = a$, a small gain is obtained by HR correction, which is more significant for $m = o$. However, this improvement for the HR corrected index $\hat{d}_{w,c}$ vanishes in $m = a$ when using the quadratic model or the cubic model getting even worse in $m = o$. This can also be a result of the over-fitting in these estimates, $\hat{d}_{w,c}$ since already subjected to an HR correction estimation (see section 2.3.7).

4.4.2 Quadratic model shows the smallest estimation error

A reduction in the median and IQR estimation error for $d = d_w$ in $m = a$ results when hours and patients values are pooled together. The IQR decreases from 0.48 for the linear model to 0.34 for both the quadratic and cubic models. The median error goes from 0.30 in the linear model to 0.22 and 0.21 in the quadratic and the cubic models, respectively. An analogous trend can be found for $d = \hat{d}_{w,c}$ in $m = a$: IQR reduces from 0.50 in $f = l$ to 0.36 in $f = q$ and to 0.39 in $f = c$. However, for both markers, the improvements disappear when the leave-one-out method $m = o$ is used, which would support the previously hypothesised over-fitting for $m = a$.

These outcomes would point at the quadratic model as the most suitable model for $\Delta[K^+]$ estimation in $m = a$, as well as in $m = o$, even if in this latter case the advantage is not very remarkable. Moreover, as mentioned above, there is no clear benefit in using a cubic rather than a quadratic model in any of both $m = a$ and $m = o$ cases, probably due to the full constrained parameter estimation rule we imposed which, when applied to the cubic model, we observed it resulted in a very small cubic term, reducing to quadratic model as in Figure 4.5.

4.4.3 $\Delta[K^+]$ reconstruction at h_0 and h_5 exhibits high uncertainty

The most distant hours from the reference point (h_0 and h_5 in this work) are the most interesting and challenging for $\Delta[K^+]$ estimation. Indeed, these two are the time points where the estimation errors are the highest and the error distributions are the widest, which is particularly true when they are taken out of the training set in the $m = o$ case (red boxplot in Figure 4.4).
That could be considered as an indication of the high uncertainty in predicting such values, especially when the values to be estimated do not have closer samples before and/or after, resulting in the wide IQR values reported for $e^f_{d,m}$ at h_0 and h_5, Table 4.1.

In general, the IQR value for $e^f_{d,m}$ at h_0 decreases for $d_w/\hat{d}_{w,c}$ in $m = a$ from 0.77/1.03 for linear to 0.58/0.73 for quadratic and to 0.37/0.67 for cubic model (similarly for the median), but again these reductions vanish in $m = o$. Analogous considerations can be made for $e^f_{d,m}$ at h_5.

4.4.4 Technical considerations

The results observed so far may lead to the conclusion that, according to the performance metrics r or $e^f_{d,o}$ considered, the observed improvement for quadratic model estimation in the case of $m = a$ vanishes, or it is largely attenuated, in $m = o$. However, when analysing data distributions we realise that values of d_w and $\hat{d}_{w,c}$ markers are not evenly distributed in all the analysed range (see Figure 4.1). This fact can imply an overweight of small d values in $m = o$ modelling, penalising the estimates at h_0 and h_5, which present d values that might not be well represented in the training set. This could also mean that the leave-one-out cross-validation needs to be cautiously framed when the value of d to be estimated is far from those used in the training set range, which in DEKAOLE dataset usually happens at h_0 and/or at h_5 as exemplified in Figure 4.6. In these cases, the estimation error between real $\Delta[K^+]$ and $\hat{\Delta}^f_{d,o}[K^+]$ would be larger than the error with respect to $\hat{\Delta}^f_{d,a}[K^+]$. This could be due to the fact that when the training set consists of all the available d values (i.e., $m = a$), thus covering all the whole spanning range for that patient, the estimated coefficients make a proper modelling and $\Delta[K^+]$ estimation possible.

However, if that range is not well represented (e.g., in $m = o$ mainly for h_0 and h_5), then the estimated coefficients model well the range of low d values, but do not model well large d values outside that range, thus not being able to provide accurate estimates for high d values, resulting in inconsistent models and then in unreliable $\Delta[K^+]$ estimation. This circumstance is particularly true for the cubic model rather than for the quadratic one, as a consequence of having an extra parameter to fit, then increasing the possibility of over-fitting, obtaining divergent values outside the training range.

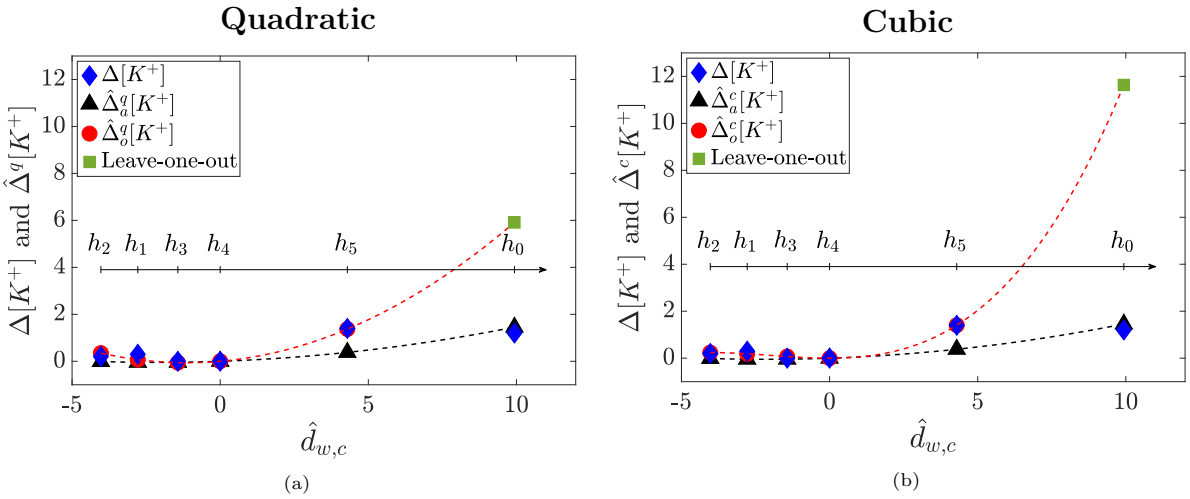

Figure 4.6: Example of leave-one-out model prediction (m=o) at h_0 compared to a $m = a$ approach for a given patient in DEKOALE dataset. The quadratic models ($f = q$) are depicted in panel (**a**) while the cubic ones ($f = c$) are in panel (**b**). In each panel: The blue diamonds represent measured $\Delta[K^+]$ values at each hour $\{h_0, h_1, h_2, h_3, h_4, h_5\}$; the black triangles are the estimated $\hat{\Delta}^f_{\hat{d}_{w,c},a}[K^+]$ while the red dots are $\hat{\Delta}^f_{\hat{d}_{w,c},o}[K^+]$ corresponding to the $\hat{d}_{w,c}$ used in the training set $\{h_1, h_2, h_3, h_4, h_5\}$, and the green square is the predicted $\hat{\Delta}^f_{\hat{d}_{w,c},o}[K^+]$ corresponding to the $\hat{d}_{w,c}$ at h_0, the hour excluded from the training set. The black-dashed line is the model in m=a while the red-dashed line accounts for the model in m=o.

4.4.5 Clinical significance

These results contribute to open a new way to turn a well-established clinical qualitative observation, i.e. the presence of hypo/hyperkalemic patterns in the ECG, into a new quantitative, noninvasive marker of blood potassium concentration. Moreover, this analysis holds promise for multiple applications and for several diseases, both in the clinical environment and in a health-monitoring scenario where it is not possible to make biochemical measurements (such as at home).

4.4.6 Limitations

Several limitations deserve to be mentioned. First of all, the reduced amount of blood sample available. Indeed, if blood samples had been collected more frequently during the early stage of the HD treatment when $[K^+]$ and, consequently, d more rapidly change, covering a broad range of values, then the model training set in $m = o$ could have better represented all the possible cases of d in the quadratic as well as in the cubic model, and then the results could have been more conclusive for the polynomial modelling improvement in predicting $[K^+]$. If this refined learning would have been done, or is done in future studies, it will, predictably, result in less error at the extreme times h_0 and h_5 of the process, and consequently also in a notably improved performance of the quadratic model both for $m = a$ and for $m = o$.

The second limitation is the lack of perfect time synchronisation between the actual $\Delta[K^+]$ and the evaluated d used for estimation at h_5. As previously reported in chapter 2, 44 h is the average ECG duration in our database – not 48 h, when the last blood sample is taken – mainly due to electrode detachment or early battery exhaustion. However, results from chapter 3 revealed a low marker dynamics in the late post-HD treatment, as can be observed in Figure 3.3. Therefore, with some degree of confidence, for this study it was assumed that the estimation error obtained between $\Delta[K^+]$ and $\hat{\Delta}^f_{d,m}[K^+]$ at h_5 would be quite similar if the actual value – had the ECG lasted, as planned, for 48 h – had been used for modelling.

Third, specific aspects of the clinical status of ESRD patients undergoing HD (e.g., possibility of previous infarction not always revealed in clinical history) could have influenced the results, generating the inter-patient variability here observed.

Finally, the reduced number of patients and available blood samples for each patient included in this study also represents a limitation to frame the conclusion of the work. Indeed, even if the proposed approach may entail a significant step towards a robust and reliable $\Delta[K^+]$ sensing from TW time-warping

based markers, it needs to be validated in larger cohorts before any translation to clinical practice. However, the available data would suggest that a patient-specific quadratic model could estimate $\Delta[K^+]$ time trends with better accuracy than a linear-model. Also, in real practice, this method implies the collection of several blood samples, which may result in cumbersome procedures. It remains to be studied to what extent the models learned in one session can be extrapolated for sessions in later days/weeks, reducing the learning to just a single session.

4.5 Conclusions

The present study shows the possibility of obtaining acceptable $\Delta[K^+]$ measurements from a digital analysis of the TW-based markers derived from the ECG in ESRD patients undergoing HD. In particular, these findings suggest a new noninvasive strategy for ECG-based $[K^+]$ sensing, with large implications for monitoring patients with cardiovascular and renal diseases, providing a meaningful tool for a personalised ambulatory cardiac risk assessment of ESRD patients undergoing HD.

CHAPTER 5

Increasing Marker Robustness to T wave Delineation Errors by Weighted Time Warping

5.1 Introduction

The use of TW morphology indexes, computed from time warping analysis, to monitor and quantify $[K^+]$ variations in ESRD patients undergoing HD was validated in previous chapters 2 and 3. In particular, both d_w^u (section 2.3.5) and d_w (section 2.3.6), have demonstrated high correlation with $\Delta[K^+]$ and d_w^u was found to be highly correlated with the dispersion of ventricular repolarization [166]. Notably, the TW morphology restitution index (TMR), obtained from d_w^u, was found to be specifically associated with sudden cardiac death (SCD) patients [222] in 651 chronic heart failure (CHF) patients when tested in the MUSIC (MUerte Súbita en Insuficiencia Cardiaca) study [223]. It was also shown that d_w^u is significantly associated with CV risk in a middle-aged population undergoing an exercise stress test in UKBiobank [224].

Automatic location of TW boundaries (i.e. onset and end position) is a necessary step in the calculation of both markers and so, a reliable delineation of TW boundaries is of great importance for the evaluation of TW-based morphology marker for SCD risk stratification [225]. In other words, errors in locating TW boundaries, due to ECG noise contamination (such as motion artifacts, powerline interference, muscle artifacts, high-frequency noise and baseline wander) and low TW amplitude and morphological variability [226, 227], may greatly affect the robustness and sensitivity of d_w^u and d_w, thus potentially impacting its risk stratification value as well as diminishing its correlation with $\Delta[K^+]$.

Therefore, it was hypothesized that inaccurate delineation of TW boundaries could introduce spurious components over the TW-based markers physiologicaly useful information. This can happen for both, $\Delta[K^+]$ monitoring and SCD risk stratification tasks. A possible solution to this problem could be to include a weighting stage in the calculation of d_w^u and d_w which would reduce the delineation errors effects on the marker. This chapter aims to assess the advantages of introducing the weighting stage and to test the markers performance as compared to a baseline case when no weighting is performed.

For this purpose, two weighting functions (WFs) are proposed and their introduced robustness in the marker against TW boundary errors in a simulated set up is evaluated. Then, an electro-physiological cardiac model is used to investigate the relation between d_w^u and d_w, obtained with and without the WFs, and the morphological changes of the action potential at cellular level. Next, the ability of the resulting markers to monitor $\Delta[K^+]$ during a HD treatment was tested. Finally, TMR index [222] was quantified by using both d_w^u and d_w with and without applying the WFs, in order to evaluate whether or not the proposed weighting stage can improve the already settled prediction value of arrhythmic risk leading to SCD in CHF patients.

5.2 Materials

5.2.1 DEKAOLE dataset

ECG signals from the DEKAOLE dataset (section 2.2) were investigated to assess the performance of the WFs when computing d_w^u and d_w for $\Delta[K^+]$ tracking.

5.2.2 MUSIC dataset

A total of 992 patients with symptomatic CHF were enrolled in the MUSIC study, a prospective, multicenter study designed to assess risk predictors of CV mortality in ambulatory CHF patients [222]. Two-(3%) or 3-lead (97%) 24-h Holter ECG sampled at 200 Hz was recorded for each patient using ELA Medical equipment (Sorin Group, Paris, France). The study protocol was approved by the institutional investigation committees, and all patients signed informed consent [223]. Although the MUSIC study included patients in atrial fibrillation, sinus, flutter, and pacemaker rhythm, in the present study we only analyzed the ECG from the 651 patients in sinus rhythm.

Follow-up visits were conducted on an outpatient basis for a median of 44 months. Subjects were classified as SCD, CD, PFD and survivors. CD was defined as SCD if it was (1) a witnessed death occurring within 60 minutes of the onset of new symptoms, unless a cause other than cardiac was obvious; (2) an unwitnessed death ($<$ 24 hours) in the absence of preexisting progressive circulatory failure or other causes of death; or (3) a death during attempted resuscitation. Deaths occurring in hospitals as a result of refractory progressive end-stage CHF were defined as PFD [223].

As previously done in [222], we considered in the group of non cardiac event (non-CE) the aggregation of survivors and non-CD, and as non-SCD the aggregation of non-CE and PFD. The number of patients in each group (SCD, PFD and non-CE) and the number of patients with two or three recorded leads are given in Table 5.1.

Table 5.1: Characteristics of the analyzed MUSIC dataset: number of patients in sinus rhythm for each considered group (i.e. SCD, PFD and non-CE) and number of records with two or three leads.

Classification Criteria	Clinical outcome			#ECG leads	
Group	SCD	PFD	non-CE	3 leads	2 leads
# Patients	55	67	529	630	21

5.3 Methods

5.3.1 Real ECG preprocessing and lead space reduction techniques

Preprocessing of ECG recordings in the DEKOALE and MUSIC datasets included baseline wander removal by high-pass, cut-off frequency of 0.5Hz, filtering in each lead followed by low-pass filtration to remove power-line noise and to attenuate muscular activity. Then, QRS complexes were detected and TW delineated using the wavelet-based delineation previously mentioned in section 2.3.2.

To emphasised TW energy content, PCA was applied lead-wise in both DEKOALE (see section 2.3.3) and MUSIC (learnt as described in [166]) datasets. The TWs in the first transform component PC1 were further delineated and smoothed by applying a 6-th order Butterworth 20 Hz low-pass filter to remove remaining noise components outside the TW frequency band.

5.3.2 Time warping markers

Markers d_w^u and d_w were computed as detailed in section 2.3.5 and 2.3.6 respectively. However, the sign was computed in the control case ($\mathcal{C}$) with no weighting, $\mathcal{W}_{\mathcal{C}}(\boldsymbol{t}^r) = \mathbf{1}$, and then applied to d_w obtained with and without weighting.

5.3.3 Weighting functions computation

Aiming to attenuate the undesired effects caused by TW delineation errors on the computation of d_w^u and d_w, two different WFs were used to emphasize the TW peak and the regions of maximum slope, respectively, while attenuating both ends.

As described in section 2.3.4, let $\boldsymbol{f}^r(\boldsymbol{t}^r)$ be a reference TW and $\boldsymbol{f}^s(\boldsymbol{t}^s)$ the studied TW (Figure 5.1a in blue and red respectively), with $\boldsymbol{t}^r = \begin{bmatrix} t^r(1) & \dots & t^r(N_r) \end{bmatrix}^\top$ and $\boldsymbol{t}^s = \begin{bmatrix} t^s(1) & \dots & t^s(N_s) \end{bmatrix}^\top$ their time duration with N_r and N_s the total length of $\boldsymbol{t}^r$ and $\boldsymbol{t}^s$, respectively.

The first proposed WF, $\mathcal{W}_{\mathcal{T}}(\boldsymbol{t}^r)$, was taken as the normalized reference TW itself, obtained by dividing $\boldsymbol{f}^r(\boldsymbol{t}^r)$ by its maximum value (Figure 5.1b, blue TW). Then, the linear function connecting the first and last samples was subtracted (Figure 5.1b, magenta), obtaining the green TW (Figure 5.1b, green), which later was also normalized by its maximum value, resulting in the final $\mathcal{W}_{\mathcal{T}}(\boldsymbol{t}^r)$ (Figure 5.1b, black).

The second weighting function, $\mathcal{W}_{\mathcal{D}}(\boldsymbol{t}^r)$, was taken as the derivative of the reference TW and computed as follows. First, the absolute value of the derivative of the reference TW, $\boldsymbol{f}^r(\boldsymbol{t}^r)$, was divided into two halves, with the middle zero value (corresponding to the $\boldsymbol{f}^r(\boldsymbol{t}^r)$ peak) taken as the splitting point. Then, the same procedure previously described for $\mathcal{W}_{\mathcal{T}}(\boldsymbol{t}^r)$ was individually applied to each half. Finally, the two parts were linked, obtaining $\mathcal{W}_{\mathcal{D}}(\boldsymbol{t}^r)$ (Figure 5.1c).

The $\gamma^*(\boldsymbol{t}^r)$ function was then multiplied by each WF:

$$\gamma^*_{\Gamma}(\boldsymbol{t}^r) = \gamma^*(\boldsymbol{t}^r) \cdot \mathcal{W}_{\Gamma}(\boldsymbol{t}^r), \tag{5.1}$$

being $\Gamma \in \{\mathcal{C}, \mathcal{T}, \mathcal{D}\}$. The resulting $\gamma^*_{\mathcal{T}}(\boldsymbol{t}^r)$ and $\gamma^*_{\mathcal{D}}(\boldsymbol{t}^r)$ are depicted in Figure 5.1e and Figure 5.1f (black solid line) respectively. Finally, both d_w^u and d_w were re-computed. We denoted markers d_w^u and d_w extracted in the control case as $d^u_{w,\mathcal{C}}$ and $d_{w,\mathcal{C}}$, respectively, while as $d^u_{w,\mathcal{T}}$, $d_{w,\mathcal{T}}$, and $d^u_{w,\mathcal{D}}$, $d_{w,\mathcal{D}}$, those after weighting with $\mathcal{W}_{\mathcal{T}}(\boldsymbol{t}^r)$ and $\mathcal{W}_{\mathcal{D}}(\boldsymbol{t}^r)$, respectively. The resulting $d_{w,\mathcal{T}}$ and $d_{w,\mathcal{D}}$, quantifying the weighted dark orange area, are depicted in Figure 5.1e and Figure 5.1f, respectively.

5.3.4 Simulation of TW boundaries shift

To assess the impact of TW boundaries shift on the calculation of d_w^u and d_w with and without applying the proposed WFs, a study simulating controlled variations in the TW duration and amplitude at different levels of TW boundaries shift was performed.

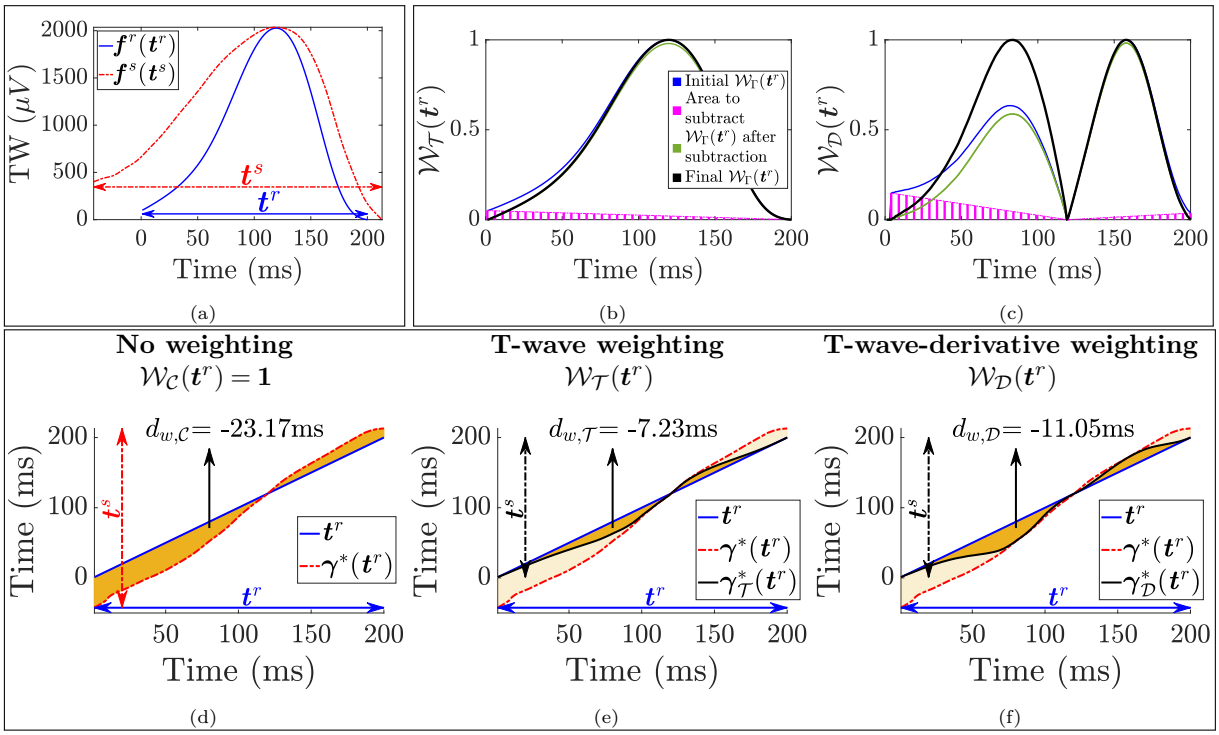

Figure 5.1: Illustration of the proposed weighting functions $\mathcal{W}_\Gamma(\boldsymbol{t}^r)$, $\Gamma \in \{\mathcal{C},\mathcal{T},\mathcal{D}\}$, and application for d_w computation. Panel (a) shows the reference and studied TW (blue and red, respectively). Panels (b) and (c) show the process to derive $\mathcal{W}_\mathcal{T}(\boldsymbol{t}^r)$ and $\mathcal{W}_\mathcal{D}(\boldsymbol{t}^r)$, respectively, as detailed in section 5.3.3. Panel (d) shows the calculation of the control $d_{w,\mathcal{C}}$ (dark orange area under $\gamma^*(\boldsymbol{t}^r)$), while panels (e) and (f) show the computation of $d_{w,\mathcal{T}}$ and $d_{w,\mathcal{D}}$, estimated by using $\gamma^*_\mathcal{T}(\boldsymbol{t}^r)$ and $\gamma^*_\mathcal{D}(\boldsymbol{t}^r)$, respectively computed as in eq. (5.1), obtaining the updated dark orange areas.

TW modulation

A reference TW, $\boldsymbol{f}^r(\boldsymbol{t}^r)$, was extracted from PC1 of a clean 12-lead ECG sampled at 1 kHz from a healthy subject [205]. Then, a set of $K = 300$ TWs modulated in amplitude and duration were generated, as in [166], according to the following steps:

1. Adding amplitude variability. Nonlinear TW amplitude variability was introduced as:

$$\begin{aligned} \boldsymbol{f}^s_{\mathrm{NL},k}(\boldsymbol{t}^r) &= \boldsymbol{f}^r(\boldsymbol{t}^r) + c(k)\sin\left(2\pi\frac{1}{4N_r}\boldsymbol{t}^r\right), \\ c(k) &= 150\sin\left(\frac{\pi\left(\frac{K}{2}+k-1\right)}{K}\right), \quad k = 1,\cdots,K \end{aligned} \tag{5.2}$$

   with N_r and $\boldsymbol{t}^r$ previously defined and k the TW index. Next, TW linear amplitude variability was modeled multiplying the deviations from the isoelectric line of $\boldsymbol{f}^s_{\mathrm{NL},k}$ by a factor sinusoidally modulated across TW:

$$\boldsymbol{f}^s_{\mathrm{L},k}(\boldsymbol{t}^r) = \left(1 + 0.15\sin\left(\frac{\pi\left(\frac{K}{2}+k-1\right)}{K}\right)\right)\boldsymbol{f}^s_{\mathrm{NL}}(\boldsymbol{t}^r) \tag{5.3}$$

2. Adding time variability. Linear variations in the time of the TW were simulated as in following equations:

$$\boldsymbol{t}^s_{\mathrm{L},k} = \gamma_k(\boldsymbol{t}^r), \quad k = 1,\cdots,K \tag{5.4}$$

   where $\gamma_k(\boldsymbol{t}^r)$ resamples $\boldsymbol{t}^r$ based on the factor $\alpha(k)$ [166]:

$$\alpha(k) = \frac{0.6\cdot(k-1)}{K-1} + 0.7, \quad k = 1,\cdots,K \tag{5.5}$$

Nonlinear variations in the temporal domain of the TW were introduced by adding a sinusoidal modulation of period N_r and linearly varying amplitude, guaranteeing a monotonic increasing function:

$$\begin{aligned} \boldsymbol{t}_k^s &= \boldsymbol{t}_{\mathrm{L},k}^s + \beta(k)\frac{N_r}{N_s}\cdot\sin\left(2\pi\frac{1}{N_r}\boldsymbol{t}_{\mathrm{L},k}^s\right), \\ \beta(k) &= \frac{30(k-1)}{K-1} - 15, \quad k = 1,\cdots,K \end{aligned} \tag{5.6}$$

The whole TW duration and amplitude variability can be expressed as:

$$\boldsymbol{f}_k^s(\boldsymbol{t}^s) = \boldsymbol{f}_{\mathrm{L},k}^s\left(\gamma_k(\boldsymbol{t}^r) + \beta(k)\frac{N_r}{N_s}\cdot\sin\left(2\pi\frac{1}{N_r}\gamma_k(\boldsymbol{t}^r)\right)\right) \tag{5.7}$$

Panels (a)-(f) in Figure 5.2 show the resulting modulated TWs for $k = 1, 60, 120, 180, 240$ and 300: the reference TW, $\boldsymbol{f}^r(\boldsymbol{t}^r)$, is displayed in solid blue in each panel, while the simulated TW ,$\boldsymbol{f}^s(\boldsymbol{t}^s)$, is plotted in solid red.

Boundaries shift

For each of the K=300 modulated $\boldsymbol{f}_k^s(\boldsymbol{t}^s)$, we simulated TW boundary location errors to: (1) T onset (T_o) only, (2) T end (T_e) only and (3) both T_o and T_e positions symmetrically. In each test, n samples, ranging from n=1 up to n=25, were progressively removed (added). Therefore, for each $\boldsymbol{f}_k^s(\boldsymbol{t}^s)$, a total of 50 boundary-shifted TWs were generated, having a boundary location standard deviation of $\sigma = 14.9$ ms, a value within the manual TW end determination tolerance [228].

Panels (g)-(l) in Figure 5.2 show the resulting TWs after simulating shifts just of the T_o position, in panels (m)-(r) are depicted the resulting TWs after T_e shift only, while in panels (s)-(x) are the TWs after shifting both T_o and T_e at the same time. In each panel (g)-(x) the s-th modulated TWs without shift (i.e. n=0) was highlighted in red. Then, markers $d_{w,\Gamma}^u$ and $d_{w,\Gamma}$ were evaluated by time warping each boundary-shifted $\boldsymbol{f}_k^s(\boldsymbol{t}^s)$ and the reference $\boldsymbol{f}^r(\boldsymbol{t}^r)$.

Finally, for every test (i.e. shift of T_o only, T_e only and symmetrical T_o-T_e shift), a variation ratio ($\mathcal{R}$) was computed for each $\boldsymbol{f}_k^s(\boldsymbol{t}^s)$ and WF as:

$$\mathcal{R}_{\Gamma,k} = \frac{\sigma(d_{\Gamma,k}(n))}{|d_{\Gamma,k}(n=0)|}, \tag{5.8}$$

where $k = 1,\cdots,300$ accounts for the modulated TW, $n \in \{-25,\cdots,25\}$ denotes the samples added (removed), $d \in \{d_w^u, d_w\}$, $\Gamma \in \{\mathcal{C},\mathcal{T},\mathcal{D}\}$, $d_{\Gamma,k}(n{=}0)$ is the marker value computed when no shift is performed and $\sigma(d_{\Gamma,k}(n))$ is the standard deviation of the marker series for kth simulated TW.

5.3.5 Simulated variability in an electrophysiological model

To assess whether using the proposed WFs affects the relationship between changes in myocardial repolarization dynamics and d_w^u [166] and d_w, an electrophysiological model [229] was used.

This equivalent double layer model formalizes the forward problem in which action potentials at M ventricular sites are projected onto the body surface. The action potentials repolarization time at each cardiac site m is given by $\rho_m = \bar{\rho} + \Delta\rho_m$, where $\bar{\rho}$ is the spatial mean repolarization time and $\Delta\rho_m$ represents the deviation from $\bar{\rho}$ at site m. The standard deviation of $\Delta\rho_m$, σ, is a measure of the global dispersion of repolarization. Ventricular action potential data was obtained from a normal male, and the ECG leads were calculated as described in [166]. Spatial PCA was performed on the resulting ECG leads, and the PC1 was preprocessed and delineated as described in section 2.3.1. The extracted TW was taken as the reference in this simulation study.

Then, a total of five different TWs, $j = 1,\cdots,5$, were generated by varying the level of σ in two scenarios:

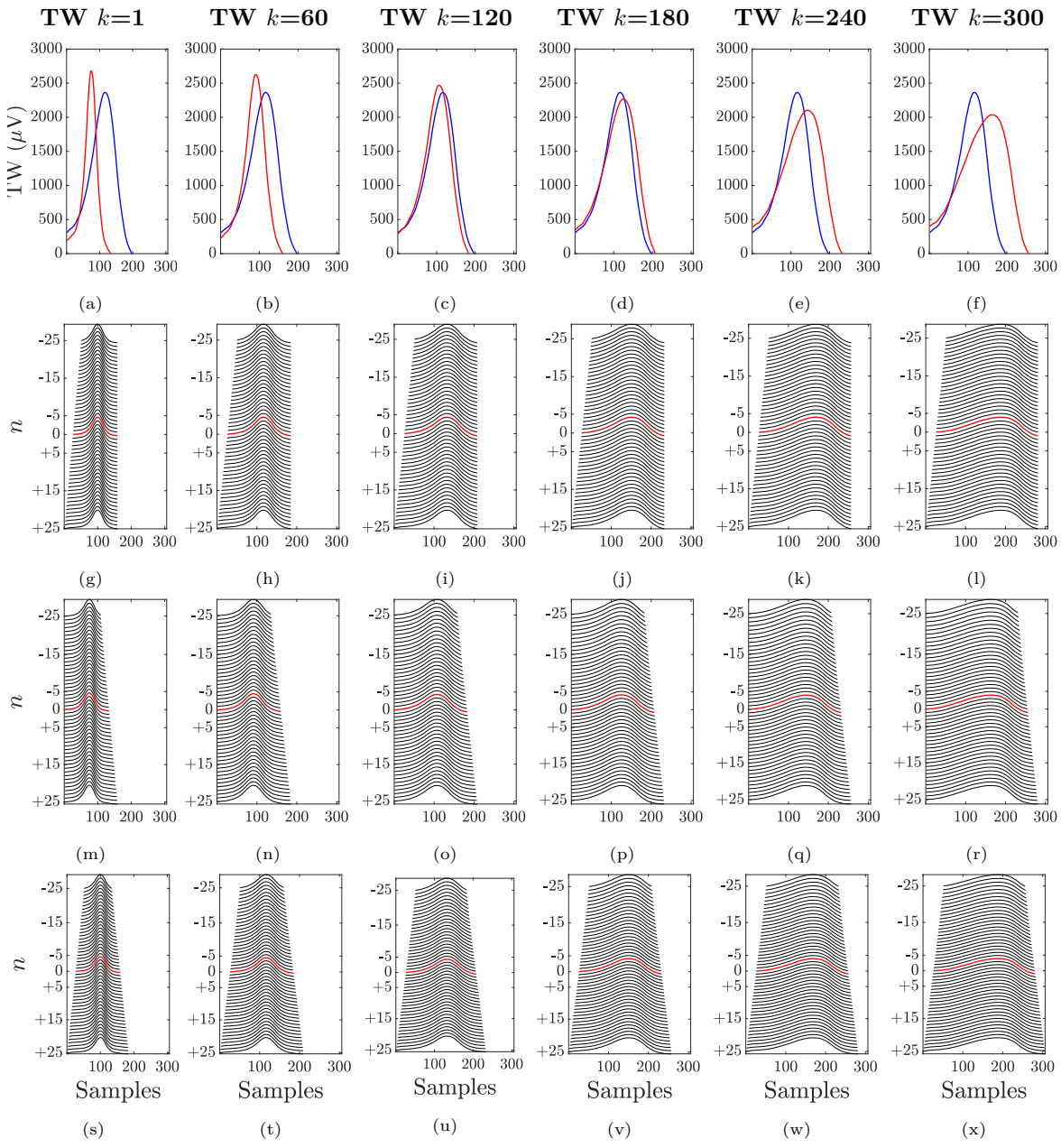

Figure 5.2: Example of evolution of linear and nonlinear time and amplitude simulated variations and corresponding TW boundaries shift. The reference TW, $\boldsymbol{f}^r(\boldsymbol{t}^r)$, is displayed in solid blue, and the simulated TW, $\boldsymbol{f}^s(\boldsymbol{t}^s)$ computed as in eq. (5.7), is plotted in solid red for $k \in \{1, 60, 120, 180, 240, 300\}$ in panels (a) to(e) respectively. In panels (g) to (l) are shown the resulting TWs after simulating T_o shifts; in panels (m) to (r) are those after simulating T_e shifts while panels (s) to (x) are the resulting TWs after simulating both T_o and T_e shifts. In each panel (g) to (x), the kth modulated TWs without shift (i.e. n=0) is depicted in in red.

1. Varying the repolarization time dispersion, σ:

$$\sigma(j) = \sqrt{\frac{1}{M-1}\sum_{m-1}^{M}(\Delta\rho_m(j))^2}, \quad j = 1,\cdots,5, \tag{5.9}$$

with $\Delta\rho_m(j) = \Delta\rho_m(1+0.2(j-1))$, expressed in ms.

2. Varying σ as in eq. (5.9), simultaneously with the lengthening of the mean repolarization time $\bar{\rho}$, according to:

$$\bar{\rho}(j) = \bar{\rho} + 25\cdot(j-1), \quad j = 1,\cdots,5. \tag{5.10}$$

The resulting $d^u_{w,\Gamma}(j)$ and $d_{w,\Gamma}(j)$ were computed by warping each jth TW with the reference TW, which for both scenarios corresponds to the TW when j=1, and plotted with respect to σ to infer the influence of the proposed WFs.

5.3.6 DEKOALE Dataset

To evaluate the effects of the proposed WFs on the reported ability of d_w and d^u_w to track $[K^+]$ variations as assessed in chapter 2, correlation between serum $\Delta[K^+]$ and $d^u_{w,\Gamma}$ and $d_{w,\Gamma}$ was reestimated. For this purpose, the same method described in section 2.3.4 was employed to compute $d^u_{w,\Gamma}$ and $d_{w,\Gamma}$.

Finally, the correlation between $\Delta[K^+]$, defined as in eq. (2.26), and $d^u_{w,\Gamma}$ and $d_{w,\Gamma}$ was evaluated by Pearson correlation (r) and compared for each of the different WF strategies.

5.3.7 MUSIC dataset

To determine if the proposed WFs can improve the SCD risk stratification value of TMR [222], this latter was recalculated using $d^u_{w,\Gamma}$ and $d_{w,\Gamma}$ following these main steps [222]:

1. **RR histogram construction:** The histogram of the RR intervals for all beats in the 24-h Holter ECG was obtained, considering bins with a width of 10 ms (Figure 5.3a). RR bins with fewer than 50 occurrences (dot orange line in Figure 5.3a) were not considered in the following analysis.

2. **Intrasubject RR range definition:** The median RR was identified (Figure 5.3a, green bin). Then, the two most distant RR bins from the median, distributed symmetrically around it, were chosen as those defining the maximum intrasubject RR range, ΔRR. Then, naming $\mathrm{RR_{max}}$ (Figure 5.3a, red bin) and $\mathrm{RR_{min}}$ (Figure 5.3a, blue bin) respectively the maximum and the minimum RR:

$$\Delta\mathrm{RR} = \mathrm{RR_{max}} - \mathrm{RR_{min}} \tag{5.11}$$

3. **MWTW computation:** The MWTWs of the TWs in the $\mathrm{RR_{min}}$ and $\mathrm{RR_{max}}$ bins were computed (Figure 5.3b and Figure 5.3c respectively) as described in section 2.3.4. Then, time warping markers $d^u_{w,\Gamma}$ and $d_{w,\Gamma}$ were computed (Figure 5.3d and Figure 5.3f).

4. **Computation of the TMR index:** TMR index was calculated dividing $d^u_{w,\Gamma}$ or $d_{w,\Gamma}$ by ΔRR (Figure 5.3f), giving information on the TW morphological change per RR increment:

$$\mathrm{TMR}^u_\Gamma = \frac{d^u_{w,\Gamma}}{\Delta\mathrm{RR}}, \quad \mathrm{TMR}_\Gamma = \frac{d_{w,\Gamma}}{\Delta\mathrm{RR}} \tag{5.12}$$

The Mann-Whitney test was used to evaluate the association of both TMR^u_Γ and TMR_Γ with SCD. Receiver operating characteristic (ROC) curves were used to test the ability to predict the endpoint and to set cutoff points for risk stratification. The population was divided into 5 equally sized groups with similar SCD and non-SCD ratio, and in each group, the criterion of minimal Euclidean distance from each ROC curve to the upper-left corner was applied to select the optimal threshold within each group [222, 230]. This was repeated 10 times, and the mean and standard deviation (std) of the AUCs, the median and IQR of the optimal thresholds and the accuracy were calculated.

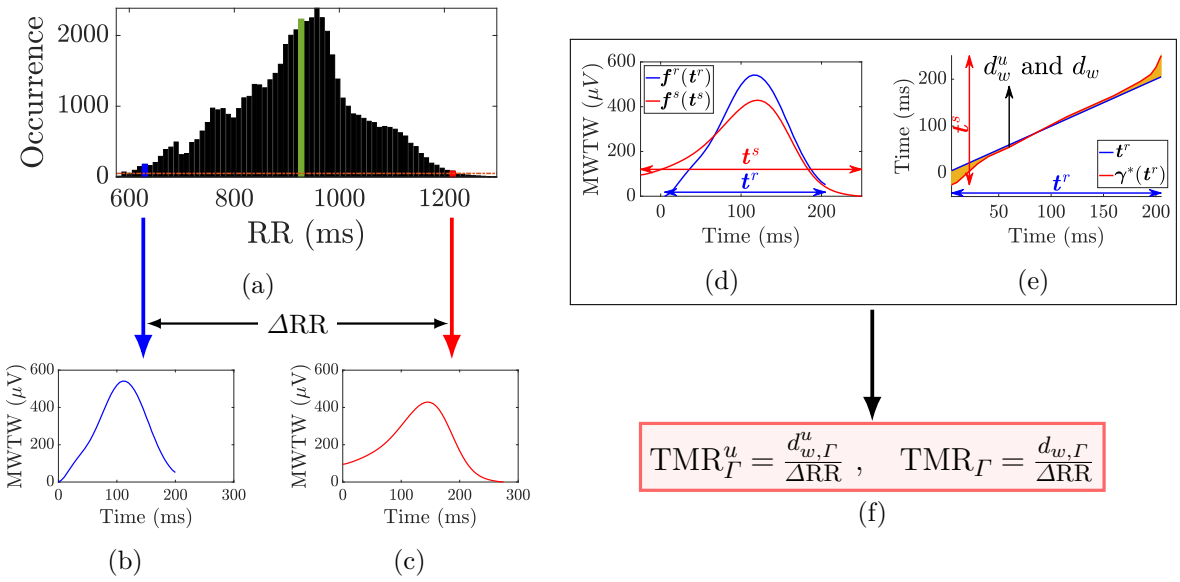

Figure 5.3: Quantification of TMR index in MUSIC dataset. Panel (a) shows the RR histogram with bins of RR=10 ms. The green bin is the median RR interval value, while the blue and red bins indicate the RR intervals defining the maximum intrasubject range, ΔRR. The orange line denotes the 50-occurrence limit. In panels (b) and (c) are the MWTWs from those RR bins selected in (a), respectively. The two MWTWs from (b) and (c) before time warping analysis are depicted in panel (d). The computation of both markers d_w^u and d_w is shown in panel (e). The TMR index of, panel (f), is calculated as $d \in \{d_w^u, d_w\}$, with and without applying the WFs $\Gamma \in \{\mathcal{C}, \mathcal{T}, \mathcal{D}\}$, normalized by the difference between the RR values of both bins, ΔRR. a.u. indicates dimensionless unit.

Survival probability, performed by using the median optimal threshold, was estimated by Kaplan-Meier methods [231, 232], comparison of cumulative events was performed by using log-rank (Mantel-Cox) tests and risk evaluation was quantified by Cox proportion hazard test [233, 234]. Patients who died from causes other than SCD were censored at the time of death. A p-val<0.05 was considered statistically significant.

5.4 Results

5.4.1 Simulation of TW boundaries shift

Distributions of $\mathcal{R}_{\Gamma,k}$ obtained when $d = d_w^u$ and $d = d_w$ are depicted in Figure 5.4a and Figure 5.4b, respectively. In each panel, the three tests (i.e. shift of T_o only, T_e only and symmetrical T_o-T_e shift) are shown, being the green, purple and orange boxplots the distributions resulting when $\mathcal{W}_\mathcal{C}(\boldsymbol{t}^r)$, $\mathcal{W}_\mathcal{T}(\boldsymbol{t}^r)$ and $\mathcal{W}_\mathcal{D}(\boldsymbol{t}^r)$ are applied respectively.

5.4.2 Simulated variability in electrophysiological model

Simulated TWs and their corresponding $d_{w,\Gamma}^u$ and $d_{w,\Gamma}$ values were obtained as described in section 5.3.5. For the first considered scenario (i.e. only varying σ) results are presented in Figure 5.5 panels (a) to (c); while those for the second scenario (i.e. combined variations in σ and $\bar{\rho}$) are in Figure 5.5 panels (d) to (f).

5.4.3 DEKOALE dataset

Distributions of $\Delta[K^+]$, $d_{w,\Gamma}^u$ and $d_{w,\Gamma}$ across patients for every hour h_i during HD therapy are depicted in Figure 5.6a and Figure 5.6b, respectively. In each panel, the blue boxplots represent $\Delta[K^+]$ and referred to the left y-axis, while the corresponding makers are referred to the right y-axis and depicted in green ($\Gamma = \mathcal{C}$), purple ($\Gamma = \mathcal{T}$) and orange ($\Gamma = \mathcal{D}$). Median (IQR) values for Pearson's correlation between $\Delta[K^+]$ and every $d_{w,\Gamma}^u$ and $d_{w,\Gamma}$ are presented in Table 5.2.

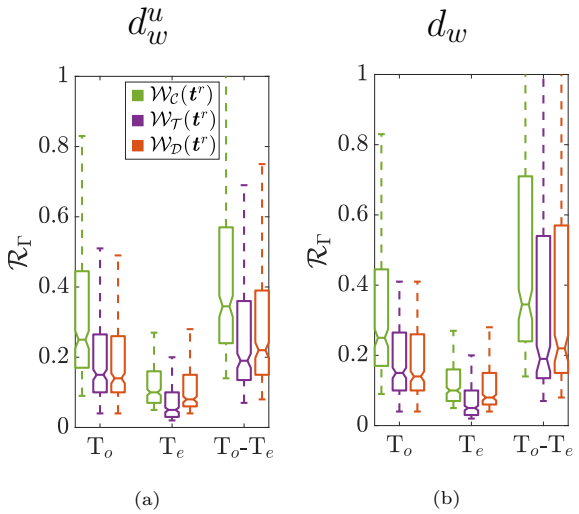

Figure 5.4: Distribution of $\mathcal{R}_{\Gamma,k}$ for each shift test (T_o only, T_e only and symmetrical T_o-T_e shift), marker and WF. In each panel, the green, purple and orange boxplots represent distributions for $\mathcal{W}_\mathcal{C}(\boldsymbol{t}^r)$, $\mathcal{W}_\mathcal{T}(\boldsymbol{t}^r)$ and $\mathcal{W}_\mathcal{D}(\boldsymbol{t}^r)$, respectively.

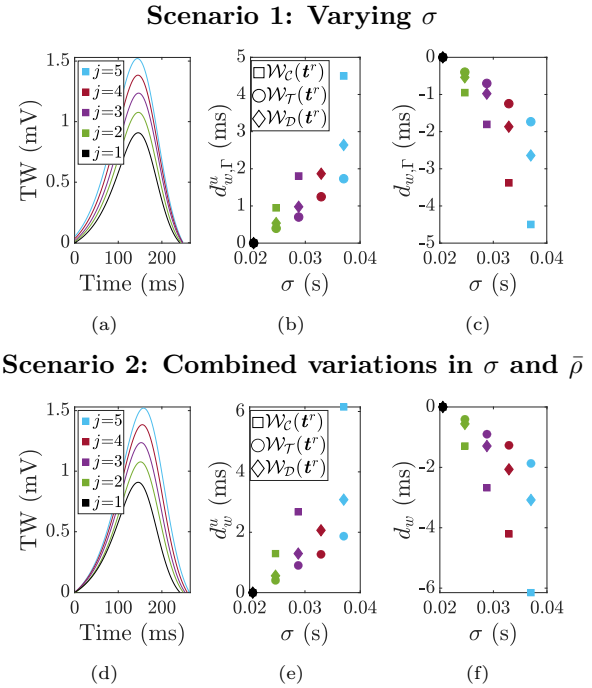

Figure 5.5: Evaluation of WF performance by electrophysiological cardiac model. (section 5.3.5). Panels (a) to (c) show the results when only σ is varied in the model; while panels (d) to (f) show the combined variation of σ and $\bar{\rho}$. Panels (a) and (d) plot the TWs; while $d_{w,\Gamma}^u$ and $d_{w,\Gamma}$ values for both scenarios are shown in panels (b), (e), (c) and (f). Square, circle and diamond-shaped markers denote results for $\mathcal{W}_\mathcal{C}(\boldsymbol{t}^r)$, $\mathcal{W}_\mathcal{T}(\boldsymbol{t}^r)$ and $\mathcal{W}_\mathcal{D}(\boldsymbol{t}^r)$, respectively. Each colour denotes results for the jth TW, corresponding to a particular σ, computed as in eq. (5.9) and eq. (5.10) (scenarios 1 and 2, respectively).

5.4.4 MUSIC dataset

Distributions of TMR_Γ^u and TMR_Γ are presented in Figure 5.7a and Figure 5.7b, respectively. Boxplots are shown in purple for $\mathcal{W}_\mathcal{T}(\boldsymbol{t}^r)$, in orange for $\mathcal{W}_\mathcal{D}(\boldsymbol{t}^r)$ and in green for the $\mathcal{W}_\mathcal{C}(\boldsymbol{t}^r)$ case. Patients are grouped according to their outcomes (i.e. SCD, PFD and non-CE). Significant Mann-Whitney test p-val (see Figure 5.7) was found for each TMR_Γ^u and TMR_Γ when comparing SCD victims and non-SCD patients regardless of the employed WF, while difference between PFD and non-CE were no significant. Finally, a statistical difference between SCD and PFD was only found for the TMR_Γ index.

Table 5.3 shows the mean (std) of the AUCs from the ROC curve analysis and median (IQR) for the optimal thresholds for SCD risk stratification evaluated for TMR_Γ^u and TMR_Γ indexes.

Figure 5.8 plots the Kaplan-Meier survival probability curves obtained after dichotomizing the study population based on the optimal thresholds for TMR_Γ^u and TMR_Γ.

5.5 Discussion

In this chapter, two WFs were proposed and introduced to attenuate the effects of TW location errors. Using these WFs, the redefined TW morphology indices, $d_{w,\Gamma}$ and $d_{w,\Gamma}^u$, were calculated and their robustness against simulated TW boundaries location errors, their physiological relevance in an electrophysiological model and in an HD dataset, and their SCD risk stratification value were thoroughly evaluated. Our main findings were that the WFs reduce the effects of TW boundaries location errors, with no impact in the ability of d_w^u and d_w to reflect repolarization dispersion, but significantly boosting their SCD risk stratification value. However, no meaningful changes in monitoring $[K^+]$ were found.

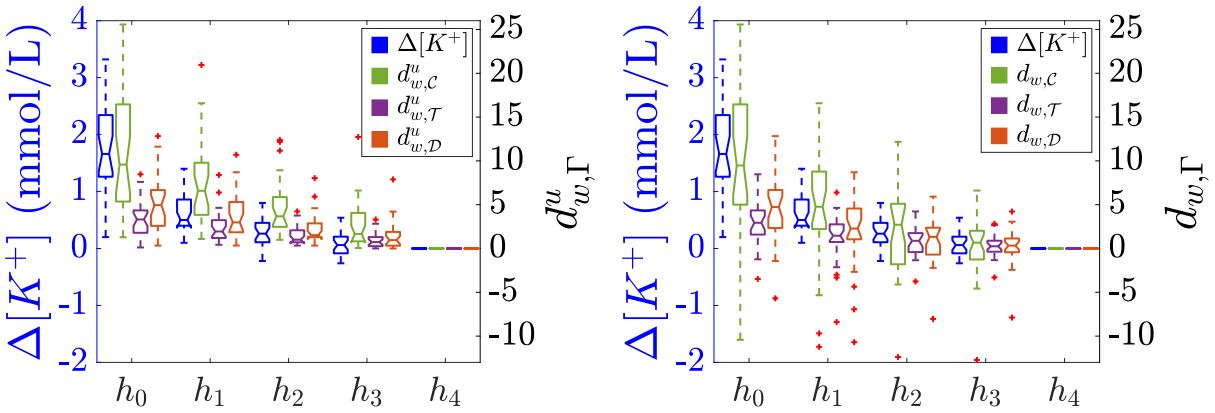

(a) (b)

Figure 5.6: Distribution of $\Delta[K^+]$ (blue, left y-axis), and $d^u_{w,\Gamma}$ (panel (a)) and $d_{w,\Gamma}$ (panel (b)) for each WF ($\Gamma \in \{\mathcal{C},\mathcal{T},\mathcal{D}\}$ green, purple and orange boxplot, respectively, right y-axis), during the HD session from h_0 to h_4 in Figure 2.1.

Table 5.2: Median and (IQR) values of Pearson's correlation coefficient (r) across patients in the DEKOALE dataset between $\Delta[K^+]$ and every combination of markers $d \in \{d^u_w, d_w\}$, WF $\Gamma \in \{\mathcal{C},\mathcal{T},\mathcal{D}\}$.

	Γ	r
$d^u_{w,\Gamma}$	$\mathcal{C}$	0.92 (0.36)
	$\mathcal{T}$	0.88 (0.36)
	$\mathcal{D}$	0.92 (0.40)
$d_{w,\Gamma}$	$\mathcal{C}$	0.89 (0.35)
	$\mathcal{T}$	0.86 (0.36)
	$\mathcal{D}$	0.90 (0.39)

Table 5.3: Values of AUC, mean (std), optimal thresholds (THR), median (IQR), and accuracy for each TMR^u_Γ and TMR_Γ. The accuracy is included for a THR derived from the complete date set.

	Γ	AUC mean (std)	Optimal THR median (IQR)	Accuracy
TMR^u_Γ	$\mathcal{C}$	0.62 (0.10)	0.045 (0.012)	0.59
	$\mathcal{T}$	0.58 (0.10)	0.012 (0.005)	0.65
	$\mathcal{D}$	0.60 (0.10)	0.021 (0.004)	0.68
TMR_Γ	$\mathcal{C}$	0.64 (0.08)	-0.045 (0.010)	0.63
	$\mathcal{T}$	0.62 (0.10)	-0.012 (0.002)	0.69
	$\mathcal{D}$	0.63 (0.09)	-0.021 (0.004)	0.70

5.5.1 Simulation of TW boundaries shift

The purpose of this analysis was to evaluate the ability of the WFs in reducing the undesired effects of TW boundaries misplacement under controlled conditions in three possible scenarios: misplacement of just one extreme, either T_o or T_e, and both of them symmetrically.

As shown in Figure 5.4, the $\mathcal{R}$ values (representing the relative error caused by those misplacements) were considerably lower for $d^u_{w,\mathcal{T}}$ and $d^u_{w,\mathcal{D}}$ with respect to $d^u_{w,\mathcal{C}}$ and similarly in case of $d_{w,\mathcal{T}}$ and $d_{w,\mathcal{D}}$ with respect to $d_{w,\mathcal{C}}$. This can be appreciate in the three tests (i.e. T_o only, T_e only and T_o-T_e symmetrically) by comparing the distributions of $\mathcal{R}_\mathcal{C}$ (in green) when no weighting was applied, with respect to $\mathcal{R}_\mathcal{T}$ (in purple) and $\mathcal{R}_\mathcal{D}$ (in orange) obtained after weighting with $\mathcal{W}_\mathcal{T}(\boldsymbol{t}^r)$ and $\mathcal{W}_\mathcal{D}(\boldsymbol{t}^r)$, respectively.

Moreover, across the three tests, smaller median and dispersion values were found for $\mathcal{R}_\mathcal{T}$ than for $\mathcal{R}_\mathcal{D}$, suggesting a slightly better performance of $\mathcal{W}_\mathcal{T}(\boldsymbol{t}^r)$ with respect to $\mathcal{W}_\mathcal{D}(\boldsymbol{t}^r)$ in terms of robustness against T_o and T_e mislabeling.

5.5.2 Simulated variability in an electrophysiological model

This test aimed to evaluate the impact of the proposed WFs have on the physiological relevance of $d^u_{w,\Gamma}$ and $d_{w,\Gamma}$. The results obtained proved the preservation of the linear relationship between $d^u_{w,\Gamma}$ and $d_{w,\Gamma}$ and the changes in dispersion of repolarization at cellular level, which only varied by a proportional factor, as shown in Figure 5.5 panels (b), (c) and panels (e), (f). These findings are in agreement with previous study [166] where only $d^u_{w,\mathcal{C}}$ was tested and found to linearly change with dispersion of repolarization as observed in this work.

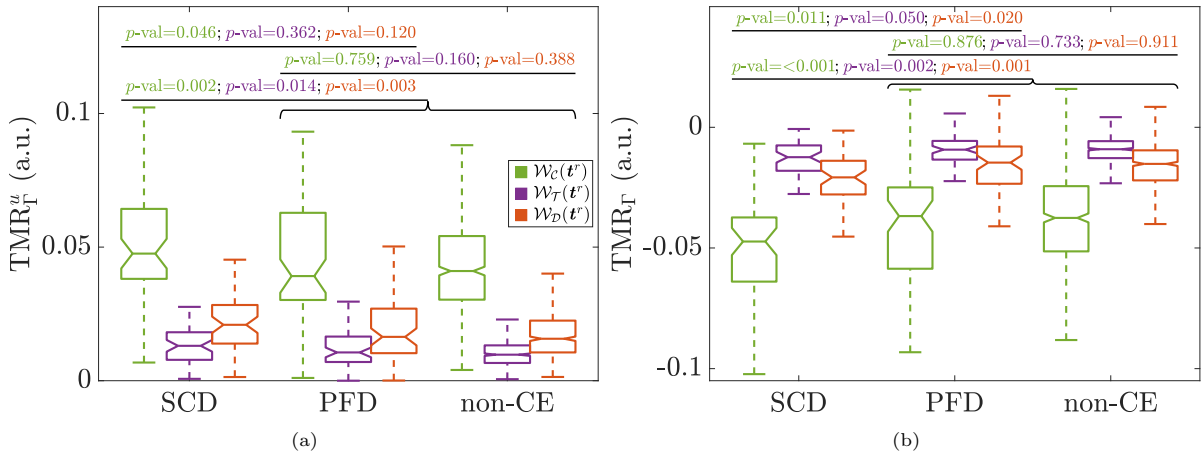

Figure 5.7: Distributions of TMR^u_Γ and TMR_Γ (panels (a) and (b) respectively), for SCD, PFD and non-CE groups for $\Gamma \in \{\mathcal{C}, \mathcal{T}, \mathcal{D}\}$ (green, purple and orange, respectively). In each panel are Mann-Whitney test p-values, colour coded for each WF, between SCD and PFD (uppermost row of p-val), PFD and non-CE (middle row of p-val) and SCD and the combination of PFD and non-CE groups (i.e. the non-SCD group) this latter highlighted with a curly bracket (lower row of p-val).

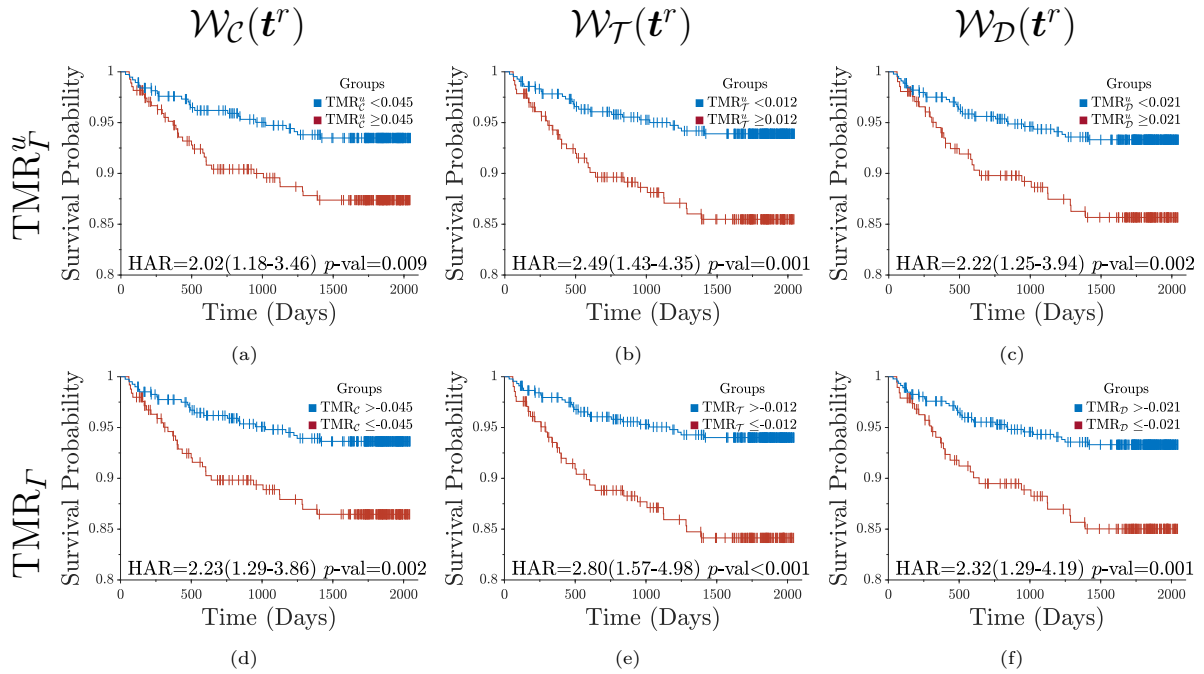

Figure 5.8: Kaplan-Meier survival curves for the two groups defined after dichotomising patients in the MUSIC dataset according to the optimal threshold computed as described in section 5.3.7. Curves for TMR^u_Γ and TMR_Γ (eq. (5.12)) are depicted in panels (a) to (c) and panels (d) to (f) respectively. In each panel, HAR value with corresponding 95% confidence intervals (CI) and p-value from the long-rank test are shown. Significant p-values were found for HAR in all the Cox analysis.

A reduction in the sensitivity to changes in dispersion of repolarization can also be observed in $d^u_{w,\mathcal{T}}$ ($d_{w,\mathcal{T}}$) and $d^u_{w,\mathcal{D}}$ ($d_{w,\mathcal{D}}$) with respect to $d^u_{w,\mathcal{C}}$ ($d_{w,\mathcal{C}}$), in both scenarios 1 and 2. Moreover, values for $d^u_{w,\Gamma}$ and $d_{w,\Gamma}$ were found to be similar in absolute value but opposite in sign, since the increments in σ led to TWs having larger magnitude and width than the reference one (black TW in Figure 5.5a and Figure 5.5d). Then, all simulated TWs had to be shrunk, i.e., negatively warped, to fit the reference.

5.5.3 DEKOALE dataset

As previously reported in chapter 2, both $d^u_{w,\mathcal{C}}$ and $d_{w,\mathcal{C}}$ were able to follow $\Delta[K^+]$ time-trend in patients undergoing HD. This capacity remained unaltered in this study regardless of the applied WF,

being the differences in Pearson correlation negligible (Table 5.2). However, the dynamic ranges of both $d^u_{w,\Gamma}$ and $d_{w,\Gamma}$ were reduced when a WFs was applied, as also observed in the first simulation scenario.

In other words, no particular improvement in monitoring $[K^+]$ during the HD resulted from the addition of a weighting stage before time warping markers computation. This might be a consequence of the substantial TW morphological changes caused by $\Delta[K^+]$ in ESRD patients: TW narrowing and remarkable magnitude increment [88, 91, 235, 236]. Then, changes of the TW morphology attributable to boundary location errors, which may or may not have occurred, seem to be negligible when compared to those driven by $\Delta[K^+]$, thus producing highly similar Pearson correlation values between markers and $\Delta[K^+]$.

5.5.4 MUSIC dataset

To evaluate the potential improvement in the SCD risk stratification value of TMR when using the proposed WFs, CHF patients in sinus rhythm from the MUSIC dataset were analysed.

Results from Mann-Whitney test (Figure 5.7) demonstrated that both TMR^u_Γ and TMR_Γ are specific markers of SCD with no relation to PFD risk, regardless of the applied WF. Whereas the AUC (Table 5.3) showed no clear advantages in using one of the proposed WF, we observed an improvement in accuracy (Table 5.3) and in SCD risk prediction power of both $\text{TMR}^u_\mathcal{T}$ ($\text{TMR}_\mathcal{T}$) and $\text{TMR}^u_\mathcal{D}$ ($\text{TMR}_\mathcal{D}$) with respect to $\text{TMR}^u_\mathcal{C}$ ($\text{TMR}_\mathcal{C}$), thus demonstrating a better ability in distinguish between SCD and non-SCD, as visible from the Kaplan-Meier survival curves (Figure 5.8).

We observed TMR_Γ provided the highest performance (Figure 5.7b). This could be due to the avoidance of opposite-sign artifacts of similar absolute value, which may have been wrongly considered as regular values when using TMR^u_Γ (Figure 5.7a). Moreover, the WF that led to the highest HAR values when using TMR_Γ was $\mathcal{W}_\mathcal{T}(\boldsymbol{t}^r)$, supporting its choice as WF when deriving TMR for future SCD risk stratification studies.

Lastly, it is worth to mention the similarity of $\text{TMR}^u_\mathcal{C}$ distribution for non-CE patients in the MUSIC study and those obtained from the UKBiobank published in [224].

5.5.5 Considerations on the use of the WFs

The two studied WFs were designed to reduce the contribution of the boundary regions, and to explore different attenuation profiles. The main difference is that $\mathcal{W}_\mathcal{T}(\boldsymbol{t}^r)$ emphasises the peak region of the TW where the warping function typically gets close to zero values, an attenuating the extremes (Figure 5.1d), while $\mathcal{W}_\mathcal{D}(\boldsymbol{t}^r)$ emphasises the slopes of the TW (Figure 5.1c) resulting in a warping function, Figure 5.1f, where the central point of the two halves was emphasised, with the extremes also attenuated. This effect is particularly clear when comparing Figure 5.1d, with respect to both Figure 5.1e and Figure 5.1f, and focusing on the extreme sections (light orange area).

In the four studied scenarios, weighting with $\mathcal{W}_\mathcal{T}(\boldsymbol{t}^r)$ results in warping markers more robust to TW boundary location errors (see section 5.5.1), leading to increased ability for SCD risk stratification than its counterpart $\mathcal{W}_\mathcal{D}(\boldsymbol{t}^r)$. This would indicate that useful physiological information may be overlooked when $\mathcal{W}_\mathcal{D}(\boldsymbol{t}^r)$ is applied. One possible explanation might be that the shape of this WF reduces, perhaps too sharply, the regions near the TW peak. Another reason might be that the regions around the TW boundaries are less attenuated than when using $\mathcal{W}_\mathcal{T}(\boldsymbol{t}^r)$, resulting in a reduced boundary misdetection attenuation effect.

Therefore, while $\mathcal{W}_\mathcal{T}(\boldsymbol{t}^r)$ is to be preferred to $\mathcal{W}_\mathcal{D}(\boldsymbol{t}^r)$ as WF in time warping analysis and subsequent TMR computation for SCD risk stratification, it seems that $\mathcal{W}_\mathcal{D}(\boldsymbol{t}^r)$ would result in $d^u_{w,\Gamma}$ and $d_{w,\Gamma}$ slightly better correlated with $\Delta[K^+]$. However, correlation coefficients are still very similar to draw strong conclusions about which is the most suitable WF for $[K^+]$ monitoring.

5.5.6 Clinical significance

Findings from the present study prove the usefulness of the WFs in reducing the effects of TW location error when deriving markers based on TW time warping analysis. Even though there were no significant

changes in $[K^+]$ monitoring in ESRD patients, a considerable improvement in SCD risk predicting values of the TMR index was observed, thus increasing its robustness and reliability for clinical applications.

5.5.7 Limitations

Several limitations deserve to be mentioned.

In this work, as in Ramírez *et al* [166], the van Oosterom equivalent double layer model was used to study the correlation between $d^u_{w,\Gamma}$ ($d_{w,\Gamma}$, respectively) and repolarization dispersion, but other biophysically detailed models of human ventricular electrophysiology [237–239] could be used to further investigate the mechanisms underlying changes in repolarization dispersion reflected in variations in the analyzed warping-based indices.

The reduced number of patients in the HD dataset and available blood samples for each patient included in the study was a limitation to better frame the conclusion of the work. However, although there was no noticeable improvement in $\Delta[K^+]$ sensing by the application of the proposed WF, they do not make results worse either, so applying WF by default in the signal processing pipeline would not decrease the usefulness of the d^u_w and d_w dispersion markers in the HD setting for monitoring $[K^+]$.

Prospective studies are needed to corroborate the observations in [222], and reinforced here with the weighting marker versions, relative to the role of TMR in SCD risk prediction in CHF patients. Indeed this study considered consecutive patients, so the number of SCD victims was low, limiting the possibilities for further statistical analysis. The clinical validity and meaningfulness of the proposed WFs over extreme TW morphological variations, such as biphasic TWs, remains to be tested.

5.6 Conclusions

T-wave morphology based markers, derived from weighted time warping, show improved robustness against the undesired effects of TW boundaries location errors without losing their physiological significance. In clinical settings, this improvement in robustness resulted in an enhancement of the SCD risk stratification value of the TMR index in CHF patients, but did not lead to a better ability to monitor $[K^+]$ in HD patients.

CHAPTER

6

Conclusions and Future Work

6.1 Summary and discussion of the main achievements

The main objective of this thesis was to develop a new approach to estimate $[K^+]$ variations in CKD patients undergoing HD, based on the analysis of the overall TW morphology. This objective has been addressed by using morphological indices extracted through TW time warping analysis, a methodology that allows the comparison of two different TW shapes and the quantification of their differences. This method has been applied and evaluated in both experimental and clinical conditions.

6.1.1 Time dynamics of time warping based markers are able to follow blood potassium concentration variations

This thesis started by evaluating whether the proposed time warping based markers, computed either in PCA-based spatial transformed lead or SL approach, could improve routine $[K^+]$ monitoring in ESRD patients undergoing HD. Not only it was found that PCA-based markers outperform those computed in SL setting, but it was proved that two (i.e. d_w and $\hat{d}_{w,c}$) out of six achieved better results than two well-known TW-based markers: the width of the TW [134], the TW slope-to-amplitude ratio [141].

This confirmed our hypothesis that quantification of the overall TW morphology, rather than just local features, provides additional information reflecting the effects of $[K^+]$ variations on the TW thus allowing a more reliable monitoring of ESRD patients undergoing HD. Moreover, these findings validated the use of $\hat{d}_{w,c}$, which assumes no correlation between HR and $[K^+]$-related TW morphology changes.

6.1.2 Periodic component analysis increases the robustness of time warping based markers in tracking blood potassium concentration variations

With the aim of overcoming PCA sensitivity to noise, a method to quantify one-beat periodicity in ventricular repolarization on ECG recordings, πCA, was investigated either learned on the whole QRST complex (πC^{B}) or on the TW (πC^{T}).

Both πC^{B} and πC^{T} outperform PCA in terms of monitoring $[K^+]$ in ESRD patients undergoing HD, as well as of robustness against BPC and low SNR, with πC^{T} showing the highest stability for continuous post-HD monitoring. These results confirmed the initial hypothesis that πCA is less sensitive to non-periodic disturbances (like BPC) than PCA, thus leading to more a reliable $\Delta[K^+]$ monitoring.

6.1.3 Quadratic regression models for noninvasive quantification of blood potassium concentration variation from ECG in hemodialysis patients

After showing that πCA-derived d_w and its HR corrected version $\hat{d}_{w,c}$, can reliably track $\Delta[K^+]$ from the ECG, a regression analysis was applied to assess the correlation between the actual $\Delta[K^+]$, computed from blood samples, and polynomial models relating d_w and $\hat{d}_{w,c}$ and $\Delta[K^+]$.

Polynomial models, and in particular the quadratic one, were found to be the most suitable for $\Delta[K^+]$ estimation, rendering higher Pearson's correlation and smaller estimation error than the linear model. Notably, these results are in agreement with those already proposed in the literature [141]. Therefore, these outcomes support the use of patient-specific polynomial models based on TW time warping-derived markers can provide better quantitative assessment of $\Delta[K^+]$.

6.1.4 Weighting stage improves the robustness to TW delineation errors

Apart from studying the prognostic value of time warping derived indexes as surrogate for $\Delta[K^+]$ monitoring, a specific study has been carried out aiming to reduce the influence of TW boundaries delineation errors as they may jeopardise TW-based markers diagnostic power.

Interestingly, the proposed weighting stage has been found to decrease the undesired effects of TW boundaries delineation errors in simulation tests, but did not improve $\Delta[K^+]$ monitoring power. Nonetheless, the proposed WFs did enhance the clinical reliability of TMR as SCD risk stratification index in the MUSIC study. As mentioned before, these differences could be a consequence of the $[K^+]$-induced TW morphology variations that may have masked those due to mislabelling of TW onset and end points. Therefore, further investigations are needed to fully understand the advantages prognostic value of the proposed weighting stage before time warping analysis.

6.2 Clinical significance

Potassium levels outside the normal range are concerning because they are usually clinically silent and occur without warning to the patient in the absence of blood tests [240]. Any efforts aimed at developing tools that can help clinicians in their decision process, especially in the proper identification of life-saving treatment to restore physiological blood potassium concentrations, are, therefore, more than justified. The research presented in this thesis sheds some light in this context.

The ECG signal represents a non-invasive, easy and, most important, cheap solution for cardiac evaluation and continuous monitoring of ESRD patients. In particular, the study of the TW morphology hold the potential to quantify abnormalities in ventricular repolarization due to $[K^+]$ impairment. With this information, in this thesis it was shown that it is possible to reliable estimate $\Delta[K^+]$ without invasive procedure, such as blood tests. This can provide real-time information of $[K^+]$ instability and help in properly delivering HD therapy as well as in evaluating its safety for the patient.
Moreover, the use of the proposed time warping indexes in ambulatory recordings, may enhance the actual cost-effectiveness of therapeutic strategies and so improve the quality of life of ESRD patients.

6.3 Conclusion

This thesis proposes new ECG-derived markers that are to some extent related to blood potassium concentration variations in ESRD patients undergoing to HD therapy: d_w and its HR corrected version $\hat{d}_{w,c}$. These markers, quantifying TW morphological variability, are extracted by a recent developed signal processing technique based on time warping. The performance of those markers were assessed in several clinical and non-clinical scenarios, and the employed methodology has been contextualized and adapted to the particularities of each of them. In this way, a general framework for dealing with several physical, such as changes in body posture, and signal, e.g. low SNR or TW boundary delineation errors, conditions has been provided.

Based on the predictive value of the proposed markers, improved diagnosis of $[K^+]$ variations could be achieved, leading to a better means for clinical decision on the specific treatment required by ESRD patients.

6.4 Future works

Some future research lines derived from this work are presented below. Some of them were already proposed in the previous chapters as a possible solution to the acknowledged limitations (e.g. the application of πCA instead of PCA as LSR technique before time warping analysis); others arise from the obtained results.

- The DEKOALE dataset was investigated along this thesis, which comprises a small population of only 29 ESRD patients and the majority of them were in hyperkalemia. Future studies should replicate the same analysis over a larger population including both hypo- and hyperkalemia cases. Moreover, new analysis should assess the correlation between the proposed time warping markers and alterations in other electrolytes beyond potassium, like calcium, magnesium, or related to the rate and amount of $[K^+]$ removal.
- Further studies should be performed in order to assess the how meals, medications and circadian rhythm could affect the relationship between the proposed markers and $\Delta[K^+]$.
- The proposed estimation models, presented in chapter 4, should be validated in a follow-up study where the models are learned at the initial HD session and used in later HD sessions to measure $\Delta[K^+]$. In such studies, the complete learning with all the available $\Delta[K^+]$ values ("$m = a$") at the initial HD session could be evaluated by its prediction value at subsequent sessions, without any overfitting risk. At this future analysis, it is expected that this approach will show better performance, in terms of correlation and estimation error, than the one reported here for the leave-one-out ("$m = o$") case, since the models' coefficients will be estimated over the six $\Delta[K^+]$ values (and not just over five as in $m = o$), thus covering the full range of marker values for each patient.
- The $[K^+]$ monitoring power of the proposed markers, should be evaluated also in subjects at risk of $[K^+]$ imbalance, such as those with DM [241] or severe CV events like myocardial infarction [242,243]. Analogous considerations can be made regarding the accuracy of the proposed regression models.
- The MUSIC dataset was investigated in chapter 5, which comprises a population of CHF patients. Future studies should validate the predictive value of the indices proposed in this thesis, with particular reference to TMR, in different populations to assess the reproducibility of the results.
- Because the MUSIC dataset is a retrospective study, further investigations on the applicability of the proposed WFs (presented in chapter 5) and the defined cut-off points on the extension of the analysis to other CHF and non-CHF populations are needed to confirm the prognostic value of the TMR with weighting procedure.
- The clinical validity and meaningfulness of the proposed WFs over extreme TW morphological variations, such as biphasic TWs, remains to be tested.

Bibliography

[1] C. P. Kovesdy, "Management of hyperkalemia: An update for the internist," *American Journal of Medicine*, vol. 128, pp. 1281–1287, dec 2015.

[2] C. P. Kovesdy, "Updates in hyperkalemia: Outcomes and therapeutic strategies," *Reviews in Endocrine and Metabolic Disorders*, vol. 18, pp. 41–47, mar 2017.

[3] I. Lazich and G. L. Bakris, "Prediction and management of hyperkalemia across the spectrum of chronic kidney disease," *Seminars in Nephrology*, vol. 34, pp. 333–339, may 2014.

[4] C. Ben Salem, A. Badreddine, N. Fathallah, R. Slim, and H. Hmouda, "Drug-Induced Hyperkalemia," in *Drug Safety*, vol. 37, pp. 677–692, Springer International Publishing, sep 2014.

[5] G. M. Fleming, "Renal replacement therapy review: Past, present and future," *Organogenesis*, vol. 7, p. 2, jan 2011.

[6] H. N. Murdeshwar and F. Anjum, "Hemodialysis," *Medicine (United Kingdom)*, vol. 47, pp. 596–602, jun 2021.

[7] M. C. Wong, J. M. Kalman, E. Pedagogos, N. Toussaint, J. K. Vohra, P. B. Sparks, P. Sanders, P. M. Kistler, K. Halloran, G. Lee, S. A. Joseph, and J. B. Morton, "Temporal distribution of arrhythmic events in chronic kidney disease: Highest incidence in the long interdialytic period," *Heart Rhythm*, vol. 12, pp. 2047–2055, oct 2015.

[8] B. Pitt and P. Rossignol, "The association between serum potassium and mortality in patients with hypertension: 'a wake-up call'," *European Heart Journal*, vol. 38, p. 113–115, 2016.

[9] F. Sacher, L. Jesel, C. Borni-Duval, V. De Precigout, F. Lavainne, J. P. Bourdenx, A. Haddj-Elmrabet, B. Seigneuric, A. Keller, J. Ott, H. Savel, Y. Delmas, D. Bazin-kara, N. Klotz, S. Ploux, S. Buffler, P. Ritter, V. Rondeau, P. Bordachar, C. Martin, A. Deplagne, S. Reuter, M. Haissaguerre, J. B. Gourraud, C. Vigneau, P. Mabo, P. Maury, T. Hannedouche, A. Benard, and C. Combe, "Cardiac Rhythm Disturbances in Hemodialysis Patients: Early Detection Using an Implantable Loop Recorder and Correlation With Biological and Dialysis Parameters," *JACC: Clinical Electrophysiology*, vol. 4, pp. 397–408, mar 2018.

[10] D. Poulikakos, K. Hnatkova, S. Skampardoni, D. Green, P. Kalra, and M. Malik, "Sudden cardiac death in dialysis: Arrhythmic Mechanisms and the Value of Non-invasive Electrophysiology," *Frontiers in Physiology*, vol. 10, p. 144, feb 2019.

[11] A. Loewe, Y. Lutz, D. Nairn, A. Fabbri, N. Nagy, N. Toth, X. Ye, D. H. Fuertinger, S. Genovesi, P. Kotanko, J. G. Raimann, and S. Severi, "Hypocalcemia-Induced Slowing of Human Sinus Node Pacemaking," *Biophysical Journal*, vol. 117, pp. 2244–2254, dec 2019.

[12] J. Hickner, D. G. Graham, N. C. Elder, E. Brandt, C. B. Emsermann, S. Dovey, and R. Phillips, "Testing process errors and their harms and consequences reported from family medicine practices: A study of the American Academy of Family Physicians National Research Network," *Quality and Safety in Health Care*, vol. 17, pp. 194–200, jun 2008.

[13] G. A. Lanza, "The Electrocardiogram as a Prognostic Tool for Predicting Major Cardiac Events," *Progress in Cardiovascular Diseases*, vol. 50, pp. 87–111, sep 2007.

[14] J. Malmivuo and R. Plonsey, "Bioelectromagnetism: Principles and Applications of Bioelectric and Biomagnetic Fields," *Bioelectromagnetism: Principles and Applications of Bioelectric and Biomagnetic Fields*, pp. 1–506, mar 2012.

[15] B. J. Maron, "The electrocardiogram as a diagnostic tool for hypertrophic cardiomyopathy: Revisited," *Annals of Noninvasive Electrocardiology*, vol. 6, no. 4, pp. 277–279, 2001.

[16] R. Oweis and L. Hijazi, "A computer-aided ECG diagnostic tool," *Computer Methods and Programs in Biomedicine*, vol. 81, pp. 279–284, mar 2006.

[17] N. G. Boyle and J. K. Vohra, "The Enduring Role of the Electrocardiogram as a Diagnostic Tool in Cardiology," *Journal of the American College of Cardiology*, vol. 69, pp. 1704–1706, apr 2017.

[18] C. Van Mieghem, M. Sabbe, and D. Knockaert, "The clinical value of the ECG in noncardiac conditions," *Chest*, vol. 125, pp. 1561–1576, apr 2004.

[19] U. Ravens and E. Cerbai, "Role of potassium currents in cardiac arrhythmias," *EP Europace*, vol. 10, p. 1133–1137, 2008.

[20] KDIGO, "Definition and classification of CKD," *Kidney Int. Suppl.*, vol. 3, pp. 16–92, 2013.

[21] L. Di Lullo, R. Rivera, V. Barbera, A. Bellasi, M. Cozzolino, D. Russo, A. De Pascalis, D. Banerjee, F. Floccari, and C. Ronco, "Sudden cardiac death and chronic kidney disease: From pathophysiology to treatment strategies," *International Journal of Cardiology*, vol. 217, pp. 16–27, aug 2016.

[22] A. Covic, M. Diaconita, P. Gusbeth-Tatomir, M. Covic, A. Botezan, G. Ungureanu, and D. J. Goldsmith, "Haemodialysis increases QTc interval but not QTc dispersion in ESRD patients without manifest cardiac disease," *Nephrology Dialysis Transplantation*, vol. 17, pp. 2170–2177, dec 2002.

[23] E. A. Secemsky, R. L. Verrier, G. Cooke, C. Ghossein, H. Subacius, A. Manuchehry, C. A. Herzog, and R. Passman, "High prevalence of cardiac autonomic dysfunction and T-wave alternans in dialysis patients," *Heart Rhythm*, vol. 8, pp. 592–598, apr 2011.

[24] I. Ogobuiro and F. Tuma, *Physiology, Renal*. StatPearls Publishing, aug 2019.

[25] B. Glodny, V. Unterholzner, B. Taferner, K. J. Hofmann, P. Rehder, A. Strasak, and J. Petersen, "Normal kidney size and its influencing factors - A 64-slice MDCT study of 1.040 asymptomatic patients," *BMC Urology*, vol. 9, 2009.

[26] W. F. Boron, *Medical Physiology: A Cellular And Molecular Approach*. Elsevier/Saunders, 2004.

[27] J. Danziger and M. L. Zeidel, "Osmotic homeostasis," *Clinical Journal of the American Society of Nephrology*, vol. 10, pp. 852–862, jan 2015.

[28] L. Lee Hamm, N. Nakhoul, and K. S. Hering-Smith, "Acid-base homeostasis," *Clinical Journal of the American Society of Nephrology*, vol. 10, pp. 2232–2242, dec 2015.

[29] M. J. Weiss, S. V. Bhoopalan, and L. J. shen Huang, "Erythropoietin regulation of red blood cell production: From bench to bedside and back," *F1000Research*, vol. 9, 2020.

[30] H. M. Wadei and S. C. Textor, "The role of the kidney in regulating arterial blood pressure," *Nature Reviews Nephrology*, vol. 8, pp. 602–609, oct 2012.

[31] M. C. Van Haaster, A. A. McDonough, and S. B. Gurley, "Blood pressure regulation by the angiotensin type 1 receptor in the proximal tubule," *Current Opinion in Nephrology and Hypertension*, vol. 27, pp. 1–7, jan 2018.

[32] S. Vahdat, "Vitamin D and Kidney Diseases: A Narrative Review.," *International journal of preventive medicine*, vol. 11, p. 195, 2020.

[33] P. Nagaraja and F. Ghalli, "Renal failure," in *Blandy's Urology*, pp. 117–126, Wiley, jan 2019.

[34] S. M. Bagshaw, C. George, and R. Bellomo, "Early acute kidney injury and sepsis: A multicentre evaluation," *Critical Care*, vol. 12, apr 2008.

[35] P. Susantitaphong, D. N. Cruz, J. Cerda, M. Abulfaraj, F. Alqahtani, I. Koulouridis, and B. L. Jaber, "World incidence of AKI: A meta-analysis," *Clinical Journal of the American Society of Nephrology*, vol. 8, no. 9, pp. 1482–1493, 2013.

[36] E. A. Hoste, J. A. Kellum, N. M. Selby, A. Zarbock, P. M. Palevsky, S. M. Bagshaw, S. L. Goldstein, J. Cerdá, and L. S. Chawla, "Global epidemiology and outcomes of acute kidney injury," *Nature Reviews Nephrology*, vol. 14, pp. 607–625, oct 2018.

[37] G. M. Chertow, E. Burdick, M. Honour, J. V. Bonventre, and D. W. Bates, "Acute kidney injury, mortality, length of stay, and costs in hospitalized patients," *Journal of the American Society of Nephrology*, vol. 16, no. 11, pp. 3365–3370, 2005.

[38] C. Y. Hsu, E. Vittinghoff, F. Li, and M. G. Shlipak, "The incidence of end-stage renal disease is increasing faster than the prevalence of chronic renal insufficiency," *Annals of Internal Medicine*, vol. 141, jul 2004.

[39] J. Coresh, E. Selvin, L. A. Stevens, J. Manzi, J. W. Kusek, P. Eggers, F. Van Lente, and A. S. Levey, "Prevalence of chronic kidney disease in the United States," *Journal of the American Medical Association*, vol. 298, pp. 2038–2047, nov 2007.

[40] L. C. Plantinga, L. E. Boulware, J. Coresh, L. A. Stevens, E. R. Miller, R. Saran, K. L. Messer, A. S. Levey, and N. R. Powe, "Patient awareness of chronic kidney disease: Trends and predictors," *Archives of Internal Medicine*, vol. 168, pp. 2268–2275, nov 2008.

[41] V. Jha, G. Garcia-Garcia, K. Iseki, Z. Li, S. Naicker, B. Plattner, R. Saran, A. Y. M. Wang, and C. W. Yang, "Chronic kidney disease: Global dimension and perspectives," *The Lancet*, vol. 382, no. 9888, pp. 260–272, 2013.

[42] A. Levin, P. E. Stevens, R. W. Bilous, J. Coresh, A. L. De Francisco, P. E. De Jong, K. E. Griffith, B. R. Hemmelgarn, K. Iseki, E. J. Lamb, A. S. Levey, M. C. Riella, M. G. Shlipak, H. Wang, C. T. White, and C. G. Winearls, "Kidney disease: Improving global outcomes (KDIGO) CKD work group. KDIGO 2012 clinical practice guideline for the evaluation and management of chronic kidney disease," *Kidney International Supplements*, vol. 3, pp. 1–150, jan 2013.

[43] A. C. Webster, E. V. Nagler, R. L. Morton, and P. Masson, "Chronic Kidney Disease," *The Lancet*, vol. 389, pp. 1238–1252, mar 2017.

[44] F. E. Murtagh, J. Addington-Hall, and I. J. Higginson, "The Prevalence of Symptoms in End-Stage Renal Disease: A Systematic Review," *Advances in Chronic Kidney Disease*, vol. 14, pp. 82–99, jan 2007.

[45] M. A. Abbasi, G. M. Chertow, and Y. N. Hall, "End-stage renal disease," *BMJ clinical evidence*, vol. 2010, 2010.

[46] M. Al-Natour and D. Thompson, "Peritoneal Dialysis," *Seminars in Interventional Radiology*, vol. 33, pp. 3–5, mar 2016.

[47] R. Mehrotra, O. Devuyst, S. J. Davies, and D. W. Johnson, "The current state of peritoneal dialysis," *Journal of the American Society of Nephrology*, vol. 27, no. 11, pp. 3238–3252, 2016.

[48] S. Vadakedath and V. Kandi, "Dialysis: A Review of the Mechanisms Underlying Complications in the Management of Chronic Renal Failure," *Cureus*, vol. 9, aug 2017.

[49] L. M. Biga, S. Dawson, A. Harwell, R. Hopkins, J. Kaufmann, M. LeMaster, P. Matern, K. Morrison-Graham, D. Quick, and J. Runyeon, *Anatomy & Physiology*, vol. 1, ch. 25, pp. 1653–1717. OpenStax/Oregon State University Ecampus, sep 2019.

[50] "Simplified hemodialysis circuit." `https://en.wikipedia.org/wiki/Hemodialysis#/media/File:Hemodialysis-en.svg`. Accessed: 2021-06-22.

[51] R. H. Anderson, R. Razavi, and A. M. Taylor, "Cardiac anatomy revisited," *Journal of Anatomy*, vol. 205, pp. 159–177, sep 2004.

[52] G. Buckberg, N. Nanda, C. Nguyen, and M. Kocica, "What Is the Heart? Anatomy, Function, Pathophysiology, and Misconceptions," *Journal of Cardiovascular Development and Disease*, vol. 5, p. 33, jun 2018.

[53] L. Sörnmo and P. Laguna, *Bioelectrical Signal Processing in Cardiac and Neurological Applications*. Elsevier Inc., 2005.

[54] F. Kusumoto, *Cardiac Anatomy and Electrophysiology*. Springer International Publishing, 2020.

[55] O. Monfredi, H. Dobrzynski, T. Mondal, M. R. Boyett, and G. M. Morris, "The anatomy and physiology of the sinoatrial node-A contemporary review," *PACE - Pacing and Clinical Electrophysiology*, vol. 33, pp. 1392–1406, nov 2010.

[56] M. L. Bakker, A. F. Moorman, and V. M. Christoffels, "The Atrioventricular Node: Origin, Development, and Genetic Program," *Trends in Cardiovascular Medicine*, vol. 20, pp. 164–171, jul 2010.

[57] R. E. Klabunde, *Cardiovascular Physiology Concepts*. Lippincott Williams & Wilkins, 2012.

[58] Durrer, D., "Electrical aspects of human cardiac activity: a clinical-physiological approach to excitation and stimulation," *Cardiovasc Res*, vol. 2, no. 1, pp. 1–18, 1968.

[59] L. F. Santana, E. P. Cheng, and W. J. Lederer, "How does the shape of the cardiac action potential control calcium signaling and contraction in the heart?," *Journal of Molecular and Cellular Cardiology*, vol. 49, pp. 901–903, dec 2010.

[60] B. M. Koeppen, R. M. Berne, M. N. Levy, and B. A. Stanton, *Physiology: 5th Edition*. Elsevier Health Sciences, 2004.

[61] D. C. Bartos, E. Grandi, and C. M. Ripplinger, "Ion channels in the heart," *Comprehensive Physiology*, vol. 5, pp. 1423–1464, jul 2015.

[62] J. M. Di Diego and Z. Q. Sun and C. Antzelevitch, "Ito and action potential notch are smaller in left vs. right canine ventricular epicardium.," *Am J Physiol*, vol. 271, pp. H548–H561, 1996.

[63] P. G. Volders, K. R. Sipido, E. Carmeliet, R. L. Spätjens, H. J. Wellens, and M. A. Vos, "Repolarizing K+ currents I(TO1) and I(Ks) are larger in right than left canine ventricular midmyocardium," *Circulation*, vol. 99, pp. 206–210, jan 1999.

[64] D. W. Liu and C. Antzelevitch, "Characteristics of the delayed rectifier current (Ikr and Iks) in canine ventricular epicardial, midmyocardial, and endocardial myocytes: A weaker Iks contributes to the longer action potential of the M cell," *Circ Res*, vol. 76, pp. 351–365, 1995.

[65] T. Furukawa, R. J. Myerburg, N. Furukawa, A. L. Bassett, and S. Kimura, "Differences in transient outward currents of feline endocardial and epicardial myocytes," *Circulation Research*, vol. 67, no. 5, pp. 1287–1291, 1990.

[66] D. Fedida and W. R. Giles, "Regional variations in action potentials and transient outward curent in myocytes isolated from rabbit left ventricle.," *J Physiol*, vol. 442, pp. 191–209, 1991.

[67] R. B. Clark, R. A. Bouchard, E. Salinas-Stefanon, J. Sanchez-Chapula, and W. R. Giles, "Heterogeneity of action potential waveforms and potassium currents in rat ventricle," *Cardiovascular Research*, vol. 27, pp. 1795–1799, oct 1993.

[68] D. L. Campbell, R. L. Rasmusson, Y. Qu, and H. C. Strauss, "The calcium-independent transient outward potassium current in isolated ferret right ventricular myocytes: I. Basic characterization and kinetic analysis," *Journal of General Physiology*, vol. 101, pp. 571–601, apr 1993.

[69] M. Näbauer, D. J. Beuckelmann, P. Überfuhr, and G. Steinbeck, "Regional differences in current density and rate-dependent properties of the transient outward current in subepicardial and subendocardial myocytes of human left ventricle," *Circulation*, vol. 93, pp. 168–177, jan 1996.

[70] E. Wettwer, G. J. Amos, H. Posival, and U. Ravens, "Transient outward current in human ventricular myocytes of subepicardial and subendocardial origin," *Circulation Research*, vol. 75, no. 3, pp. 473–482, 1994.

[71] T. Watanabe, L. M. Delbridge, J. O. Bustamante, and T. F. McDonald, "Heterogeneity of the action potential in isolated rat ventricular myocytes and tissue," *Circulation Research*, vol. 52, no. 3, pp. 280–290, 1983.

[72] C. Antzelevitch, S. Sicouri, S. H. Litovsky, A. Lukas, S. C. Krishnan, J. M. Di Diego, G. A. Gintant, and D. W. Liu, "Heterogeneity within the ventricular wall. Electrophysiology and pharmacology of epicardial, endocardial, and M cells," *Circulation Research*, vol. 69, no. 6, pp. 1427–1449, 1991.

[73] S. M. Bryant, X. Wan, S. J. Shipsey, and G. Hart, "Regional differences in the delayed rectifier current (I(Kr) and I(Ks)) contribute to the differences in action potential duration in basal left ventricular myocytes in guinea-pig," *Cardiovascular Research*, vol. 40, pp. 322–331, nov 1998.

[74] J. Cheng, K. Kamiya, W. Liu, Y. Tsuji, J. Toyama, and I. Kodama, "Heterogeneous distribution of the two components of delayed rectifier K+ current: A potential mechanism of the proarrhythmic effects of methanesulfonanilideclass III agents," *Cardiovascular Research*, vol. 43, pp. 135–147, jul 1999.

[75] J. Feng, "Transmural heterogeneity of action potentials and I(to1) in myocytes isolated from the human right ventricle," *American Journal of Physiology - Heart and Circulatory Physiology*, vol. 275, no. 2 44-2, 1998.

[76] N. Ueda, D. P. Zipes, and J. Wu, "Functional and transmural modulation of M cell behavior in canine ventricular wall," *American Journal of Physiology - Heart and Circulatory Physiology*, vol. 287, dec 2004.

[77] T. Volk, T. H. D. Nguyen, J. H. Schultz, and H. Ehmke, "Relationship between transient outward K+ current and Ca2+ influx in rat cardiac myocytes of endo- and epicardial origin," *Journal of Physiology*, vol. 519, pp. 841–850, sep 1999.

[78] T. Volk, T. H. D. Nguyen, J. H. Schultz, J. Faulhaber, and H. Ehmke, "Regional alterations of repolarizing K + currents among the left ventricular free wall of rats with ascending aortic stenosis," *Journal of Physiology*, vol. 530, pp. 443–455, feb 2001.

[79] F. G. Akar, K. R. Laurita, and D. S. Rosenbaum, "Cellular basis for dispersion of repolarization underlying reentrant arrhythmias," *Journal of Electrocardiology*, vol. 33, pp. 23–31, jan 2000.

[80] A. Dupre, S. Vincent, and P. A. Iaizzo, "Basic ECG theory, recordings, and interpretation," in *Handbook of Cardiac Anatomy, Physiology, and Devices*, pp. 191–201, Humana Press, 2005.

[81] J. Malmivuo and R. Plonsey, "Bioelectromagnetism: Principles and Applications of Bioelectric and Biomagnetic Fields," *Bioelectromagnetism: Principles and Applications of Bioelectric and Biomagnetic Fields*, pp. 185–226, mar 2012.

[82] J. Malmivuo and R. Plonsey, "Bioelectromagnetism: Principles and Applications of Bioelectric and Biomagnetic Fields," *Bioelectromagnetism: Principles and Applications of Bioelectric and Biomagnetic Fields*, pp. 290–306, mar 2012.

[83] E. Frank, "An Accurate, Clinically Practical System For Spatial Vectorcardiography," *Circulation*, vol. 13, no. 5, pp. 737–749, 1956.

[84] D. E. Becker, "Fundamentals of electrocardiography interpretation," *Anesthesia progress*, vol. 53, p. 53, jun 2006.

[85] E. Kardalas, S. A. Paschou, P. Anagnostis, G. Muscogiuri, G. Siasos, and A. Vryonidou, "Hypokalemia: A clinical update," *Endocrine Connections*, vol. 7, pp. R135–R146, apr 2018.

[86] A. Lehnhardt and M. J. Kemper, "Pathogenesis, diagnosis and management of hyperkalemia," *Pediatric Nephrology*, vol. 26, pp. 377–384, mar 2011.

[87] D. B. Diercks, G. M. Shumaik, R. A. Harrigan, W. J. Brady, and T. C. Chan, "Electrocardiographic manifestations: Electrolyte abnormalities," *Journal of Emergency Medicine*, vol. 27, no. 2, pp. 153–160, 2004.

[88] N. El-Sherif and G. Turitto, "Electrolyte disorders and arrhythmogenesis," *Cardiol J.*, vol. 3, no. 18, pp. 233–45, 2011.

[89] J. T. Levis, "ECG diagnosis: hypokalemia," *The Permanente journal*, vol. 16, no. 2, p. 57, 2012.

[90] A. Webster, W. Brady, and F. P. Morris, "Recognising signs of danger: ECG changes resulting from an abnormal serum potassium concentration," *Emergency Medicine Journal*, vol. 19, no. 1, pp. 74–77, 2002.

[91] J. T. Levis, "ECG diagnosis: hyperkalemia.," *The Permanente journal*, vol. 17, no. 1, p. 69, 2013.

[92] B. Surawicz, "Relationship between electrocardiogram and electrolytes," *American Heart Journal*, vol. 73, no. 6, pp. 814–834, 1967.

[93] K. L. Dittrich and R. M. Walls, "Hyperkalemia: ECG manifestations and clinical considerations," *Journal of Emergency Medicine*, vol. 4, no. 6, pp. 449–455, 1986.

[94] F. J. Gennari, "Disorders of potassium homeostasis: Hypokalemia and hyperkalemia," *Critical Care Clinics*, vol. 18, no. 2, pp. 273–288, 2002.

[95] T. J. Schaefer and R. W. Wolford, "Disorders of potassium," *Emergency Medicine Clinics of North America*, vol. 23, no. 3 SPEC. ISS., pp. 723–747, 2005.

[96] D. A. Wald, "ECG manifestations of selected metabolic and endocrine disorders," *Emergency Medicine Clinics of North America*, vol. 24, no. 1, pp. 145–157, 2006.

[97] W. A. Parham, A. A. Mehdirad, K. M. Biermann, and C. S. Fredman, "Hyperkalemia revisited," *Texas Heart Institute Journal*, vol. 33, no. 1, pp. 40–47, 2006.

[98] J. Rizer, J. D. King, and N. P. Charlton, "The ECG and Electrolyte Abnormalities," in *Electrocardiogram in Clinical Medicine*, pp. 297–306, Wiley, aug 2020.

[99] R. Noordam, W. J. Young, R. Salman, J. K. Kanters, M. E. van den Berg, D. van Heemst, H. J. Lin, S. M. Barreto, M. L. Biggs, G. Biino, E. Catamo, M. P. Concas, J. Ding, D. S. Evans, L. Foco, N. Grarup, L. P. Lyytikäinen, M. Mangino, H. Mei, P. J. van der Most, M. Müller-Nurasyid, C. P. Nelson, Y. Qian, L. Repetto, M. A. Said, N. Shah, K. Schramm, P. G. Vidigal, S. Weiss, J. Yao, N. R. Zilhao, J. A. Brody, P. S. Braund, M. Brumat, E. Campana, P. Christofidou, M. J. Caulfield, A. De Grandi, A. F. Dominiczak, A. S. Doney, G. Eiriksdottir, C. Ellervik, L. Giatti, M. Gögele, C. Graff, X. Guo, P. van der Harst, P. K. Joshi, M. Kähönen, B. Kestenbaum, M. F. Lima-Costa, A. Linneberg, A. C. Maan, T. Meitinger, S. Padmanabhan, C. Pattaro, A. Peters, A. Petersmann, P. Sever, M. F. Sinner, X. Shen, A. Stanton, K. Strauch, E. Z. Soliman, K. V. Tarasov, K. D. Taylor, C. H. Thio, A. G. Uitterlinden, S. Vaccargiu, M. Waldenberger, A. Robino, A. Correa, F. Cucca, S. R. Cummings, M. Dörr, G. Girotto, V. Gudnason, T. Hansen, S. R. Heckbert, C. R. Juhl, S. Kääb, T. Lehtimäki, Y. Liu, P. A. Lotufo, C. N. Palmer, M. Pirastu, P. P. Pramstaller, A. L. P. Ribeiro, J. I. Rotter, N. J. Samani, H. Snieder, T. D. Spector, B. H. Stricker, N. Verweij, J. F. Wilson, J. G. Wilson, J. W. Jukema, A. Tinker, C. H. Newton-Cheh, N. Sotoodehnia, D. O. Mook-Kanamori, P. B. Munroe, and H. R. Warren, "Effects of Calcium, Magnesium, and Potassium Concentrations on Ventricular Repolarization in Unselected Individuals," *Journal of the American College of Cardiology*, vol. 73, pp. 3118–3131, jun 2019.

[100] H. Fukuta, J. Hayano, S. Ishihara, S. Sakata, S. Mukai, N. Ohte, K. Ojika, K. Yagi, H. Matsumoto, S. Sohmiya, and G. Kimura, "Prognostic value of heart rate variability in patients with end-stage renal disease on chronic haemodialysis," *Nephrology Dialysis Transplantation*, vol. 18, pp. 318–325, feb 2003.

[101] K. Oikawa, R. Ishihara, T. Maeda, K. Yamaguchi, A. Koike, H. Kawaguchi, Y. Tabata, N. Murotani, and H. Itoh, "Prognostic value of heart rate variability in patients with renal failure on hemodialysis," *International Journal of Cardiology*, vol. 131, pp. 370–377, jan 2009.

[102] S. Genovesi, O. Bracchi, P. Fabbrini, E. Luisetto, M. R. Viganó, D. Lucini, M. Malacarne, A. Stella, and M. Pagani, "Differences in heart rate variability during haemodialysis and haemofiltration," *Nephrology Dialysis Transplantation*, vol. 22, pp. 2256–2262, aug 2007.

[103] M. Mylonopoulou, N. Tentolouris, S. Antonopoulos, S. Mikros, K. Katsaros, A. Melidonis, N. Sevastos, and N. Katsilambros, "Heart rate variability in advanced chronic kidney disease with or without diabetes: Midterm effects of the initiation of chronic haemodialysis therapy," *Nephrology Dialysis Transplantation*, vol. 25, pp. 3749–3754, nov 2010.

[104] S. C. Chen, J. C. Huang, Y. C. Tsai, R. N. Hsiu-Chin Mai, R. N. Jui-Hsin Chen, P. L. Kuo, J. M. Chang, S. J. Hwang, and H. C. Chen, "Heart Rate Variability Change before and after Hemodialysis is Associated with Overall and Cardiovascular Mortality in Hemodialysis," *Scientific Reports*, vol. 6, feb 2016.

[105] H. Fukuta, J. Hayano, S. Ishihara, S. Sakata, N. Ohte, H. Takahashi, M. Yokoya, T. Toriyama, H. Kawahara, K. Yajima, K. Kobayashi, and G. Kimura, "Prognostic value of nonlinear heart rate dynamics in hemodialysis patients with coronary artery disease," *Kidney International*, vol. 64, pp. 641–648, aug 2003.

[106] H. González, O. Infante, H. Pérez-Grovas, M. V. Jose, and C. Lerma, "Nonlinear dynamics of heart rate variability in response to orthostatism and hemodialysis in chronic renal failure patients: Recurrence analysis approach," *Medical Engineering and Physics*, vol. 35, pp. 178–187, feb 2013.

[107] C. Lerma, O. Infante, H. Pérez-Grovas, and M. V. José, "Poincaré plot indexes of heart rate variability capture dynamic adaptations after haemodialysis in chronic renal failure patients," *Clinical Physiology and Functional Imaging*, vol. 23, no. 2, pp. 72–80, 2003.

[108] N. Pilia, S. Severi, J. G. Raimann, S. Genovesi, O. Dössel, P. Kotanko, C. Corsi, and A. Loewe, "Quantification and classification of potassium and calcium disorders with the electrocardiogram: What do clinical studies, modeling, and reconstruction tell us?," *APL Bioengineering*, vol. 4, dec 2020.

[109] S. M. Straus, J. A. Kors, M. L. De Bruin, C. S. Van Der Hooft, A. Hofman, J. Heeringa, J. W. Deckers, J. H. Kingma, M. C. Sturkenboom, B. H. Stricker, and J. C. Witteman, "Prolonged QTc interval and risk of sudden cardiac death in a population of older adults," *Journal of the American College of Cardiology*, vol. 47, pp. 362–367, jan 2006.

[110] D. Nanchen, M. J. Leening, I. Locatelli, J. Cornuz, J. A. Kors, J. Heeringa, J. W. Deckers, A. Hofman, O. H. Franco, B. H. Stricker, J. C. Witteman, and A. Dehghan, "Resting heart rate and the risk of heart failure in healthy adults the rotterdam study," *Circulation: Heart Failure*, vol. 6, pp. 403–410, may 2013.

[111] A. Saxena, D. Minton, D. C. Lee, X. Sui, R. Fayad, C. J. Lavie, and S. N. Blair, "Protective role of resting heart rate on all-cause and cardiovascular disease mortality," *Mayo Clinic Proceedings*, vol. 88, pp. 1420–1426, dec 2013.

[112] S. E. Näppi, V. K. Virtanen, H. H. Saha, J. T. Mustonen, and A. I. Pasternack, "QT(c) dispersion increases during hemodialysis with low-calcium dialysate," *Kidney International*, vol. 57, no. 5, pp. 2117–2122, 2000.

[113] Y. Matsumoto, Y. Mori, S. Kageyama, K. Arihara, H. Sato, K. Nagata, Y. Shimada, Y. Nojima, K. Iguchi, and T. Sugiyama, "Changes in QTc interval in long-term hemodialysis patients," *PLOS ONE*, vol. 14, p. e0209297, jan 2019.

[114] S. Genovesi, C. Dossi, M. R. Viganò, E. Galbiati, F. Prolo, A. Stella, and M. Stramba-Badiale, "Electrolyte concentration during haemodialysis and QT interval prolongation in uraemic patients," *Europace*, vol. 10, pp. 771–777, jun 2008.

[115] S. Severi, E. Grandi, C. Pes, F. Badiali, F. Grandi, and A. Santoro, "Calcium and potassium changes during haemodialysis alter ventricular repolarization duration: In vivo and in silico analysis," *Nephrology Dialysis Transplantation*, vol. 23, pp. 1378–1386, apr 2008.

[116] E. D. Kim, J. Watt, L. G. Tereshchenko, B. G. Jaar, S. M. Sozio, W. H. Kao, M. M. Estrella, and R. S. Parekh, "Associations of serum and dialysate electrolytes with QT interval and prolongation in incident hemodialysis: The Predictors of Arrhythmic and Cardiovascular Risk in End-Stage Renal Disease (PACE) study," *BMC Nephrology*, vol. 20, apr 2019.

[117] A. Cupisti, F. Galetta, R. Caprioli, E. Morelli, G. C. Tintori, F. Franzoni, A. Lippi, M. Meola, P. Rindi, and G. Barsotti, "Potassium Removal Increases the QTc Interval Dispersion during Hemodialysis," *Nephron*, vol. 82, no. 2, pp. 122–126, 1999.

[118] S. Abe, M. Yoshizawa, N. Nakanishi, T. Yazawa, K. Yokota, M. Honda, and G. Sloman, "Electrocardiographic abnormalities in patients receiving hemodialysis," *American Heart Journal*, vol. 131, no. 6, pp. 1137–1144, 1996.

[119] P. Meier, P. Vogt, and E. Blanc, "Ventricular arrhythmias and sudden cardiac death in end-stage renal disease patients on chronic hemodialysis," *Nephron*, vol. 87, no. 3, pp. 199–214, 2001.

[120] P. A. McCullough, S. Steigerwalt, K. Tolia, S. C. Chen, S. Li, K. C. Norris, and A. Whaley-Connell, "Cardiovascular disease in chronic kidney disease: Data from the kidney early evaluation program (KEEP)," *Current Diabetes Reports*, vol. 11, pp. 47–55, feb 2011.

[121] H. C. Dittrich, L. A. Pearce, R. W. Asinger, R. McBride, R. Webel, M. Zabalgoitia, G. D. Pennock, R. E. Safford, R. M. Rothbart, J. L. Halperin, and R. G. Hart, "Left atrial diameter in nonvalvular atrial fibrillation: An echocardiographic study," *American Heart Journal*, vol. 137, no. 3, pp. 494–499, 1999.

[122] A. Páll, Á. Czifra, V. Sebestyén, G. Becs, C. Kun, J. Balla, G. Paragh, I. Lőrincz, D. Páll, T. J. Padra, A. Agarwal, A. Zarjou, and Z. Szabó, "Hemodiafiltration and hemodialysis differently affect P wave duration and dispersion on the surface electrocardiogram," *International Urology and Nephrology*, vol. 48, pp. 271–277, feb 2016.

[123] P. E. Dilaveris, E. J. Gialafos, S. K. Sideris, A. M. Theopistou, G. K. Andrikopoulos, M. Kyriakidis, J. E. Gialafos, and P. K. Toutouzas, "Simple electrocardiographic markers for the prediction of paroxysmal idiopathic atrial fibrillation," *American Heart Journal*, vol. 135, no. 5 I, pp. 733–738, 1998.

[124] G. K. Andrikopoulos, P. E. Dilaveris, D. J. Richter, E. J. Gialafos, A. G. Synetos, and J. E. Gialafos, "Increased variance of P wave duration on the electrocardiogram distinguishes patients with idiopathic paroxysmal atrial fibrillation," *PACE - Pacing and Clinical Electrophysiology*, vol. 23, no. 7, pp. 1127–1132, 2000.

[125] K. Aytemir, N. Özer, E. Atalar, E. Sade, S. Aksöyek, K. Övünç, A. Oto, F. Özmen, and S. Kes, "P wave dispersion on 12-lead electrocardiography in patients with paroxysmal atrial fibrillation," *PACE - Pacing and Clinical Electrophysiology*, vol. 23, no. 7, pp. 1109–1112, 2000.

[126] R. Vanholder, N. Meert, E. Schepers, and G. Glorieux, "From uremic toxin retention to removal by convection: Do we know enough?," in *Contributions to Nephrology*, vol. 161, pp. 125–131, Contrib Nephrol, 2008.

[127] K. Shimada, T. Tomita, Y. Kamijo, M. Higuchi, K. Ito, Y. Koizumi, K. Yamamoto, K. Aizawa, M. Koshikawa, H. Kasai, A. Izawa, Y. Miyashita, S. Kumazaki, J. Koyama, and U. Ikeda, "Hemodialysis-induced P-wave signal-averaged electrocardiogram alterations are indicative of vulnerability to atrial arrhythmias," *Circulation Journal*, vol. 76, no. 3, pp. 612–617, 2012.

[128] Z. Szabó, G. Kakuk, T. Fülöp, J. Mátyus, J. Balla, I. Kárpáti, A. Juhász, C. Kun, Z. Karányi, and I. Lorincz, "Effects of haemodialysis on maximum P wave duration and P wave dispersion," *Nephrology Dialysis Transplantation*, vol. 17, no. 9, pp. 1634–1638, 2002.

[129] S.-C. Chen, H.-M. Su, J.-C. Huang, K. Chang, Y.-C. Tsai, L.-I. Chen, J.-M. Chang, S.-J. Hwang, and H.-C. Chen, "Association of P-Wave Dispersion with Overall and Cardiovascular Mortality in Hemodialysis Patients," *American Journal of Nephrology*, vol. 42, pp. 198–205, nov 2015.

[130] B. T. Montague, J. R. Ouellette, and G. K. Buller, "Retrospective review of the frequency of ECG changes in hyperkalemia," *Clinical Journal of the American Society of Nephrology*, vol. 3, pp. 324–330, mar 2008.

[131] J. N. An, J. P. Lee, H. J. Jeon, D. H. Kim, Y. K. Oh, Y. S. Kim, and C. S. Lim, "Severe hyperkalemia requiring hospitalization: Predictors of mortality," *Critical Care*, vol. 16, nov 2012.

[132] B. J. Kenny and K. N. Brown, *ECG T Wave*. StatPearls Publishing, aug 2019.

[133] M. Greenlee, C. S. Wingo, A. A. McDonough, J. H. Youn, and B. C. Kone, "Narrative review: Evolving concepts in potassium homeostasis and hypokalemia," *Annals of Internal Medicine*, vol. 150, pp. 619–625, may 2009.

[134] P. P. Frohnert, E. R. Gluliani, M. Friedberg, W. J. Johnson, and W. N. Tauxe, "Statistical investigation of correlations between serum potassium levels and electrocardiographic findings in patients on intermittent hemodialysis therapy," *Circulation*, vol. 41, p. 667–676, 1970.

[135] J. J. Dillon, C. V. Desimone, Y. Sapir, V. K. Somers, J. L. Dugan, C. J. Bruce, M. J. Ackerman, S. J. Asirvatham, B. L. Striemer, J. Bukartyk, C. G. Scott, K. E. Bennet, S. B. Mikell, D. J. Ladewig, E. J. Gilles, A. Geva, D. Sadot, and P. A. Friedman, "Noninvasive potassium determination using a mathematically processed ECG: Proof of concept for a novel "blood-less, blood test"," *Journal of Electrocardiology*, vol. 48, pp. 12–18, jan 2015.

[136] V. Velagapudi, J. C. O'Horo, A. Vellanki, S. P. Baker, R. Pidikiti, J. S. Stoff, and D. A. Tighe, "Computer-assisted image processing 12 lead ECG model to diagnose hyperkalemia," *Journal of Electrocardiology*, vol. 50, pp. 131–138, jan 2017.

[137] G. Regolisti, U. Maggiore, P. Greco, C. Maccari, E. Parenti, F. Di Mario, V. Pistolesi, S. Morabito, and E. Fiaccadori, "Electrocardiographic T wave alterations and prediction of hyperkalemia in patients with acute kidney injury," *Internal and Emergency Medicine*, vol. 15, pp. 463–472, 2020.

[138] D. A. Ferenbach and J. V. Bonventre, "Acute kidney injury and chronic kidney disease: From the laboratory to the clinic," *Nephrologie et Therapeutique*, vol. 12, pp. S41–S48, apr 2016.

[139] K. D. Wrenn, C. M. Slovis, and B. S. Slovis, "The ability of physicians to predict hyperkalemia from the ECG," *Annals of Emergency Medicine*, vol. 20, pp. 1229–1232, nov 1991.

[140] B. W. Johansson and C. Larsson, "A Hypokalemic Index ECG as a Predictor of Hypokalemia," *Acta Medica Scandinavica*, vol. 212, pp. 29–32, apr 2009.

[141] C. Corsi, M. Cortesi, G. Callisesi, J. De Bie, C. Napolitano, A. Santoro, D. Mortara, and S. Severi, "Noninvasive quantification of blood potassium concentration from ECG in hemodialysis patients," *Scientific Reports*, vol. 7, pp. 1–10, feb 2017.

[142] S. Severi, C. Corsi, M. Haigney, J. DeBie, and D. Mortara, "Noninvasive potassium measurements from ecg analysis during hemodialysis sessions," in *2009 36th Annual Computers in Cardiology Conference (CinC)*, pp. 821–824, 2009.

[143] C. Corsi, J. DeBie, C. Napolitano, S. Priori, D. Mortara, and S. Severi, "Validation of a novel method for non-invasive blood potassium quantification from the ecg," in *2012 Computing in Cardiology*, pp. 105–108, 2012.

[144] C. Corsi, J. De Bie, D. Mortara, and S. Severi, "Innovative solutions in health monitoring at home: The real-time assessment of serum potassium concentration from ECG," in *Lecture Notes in Computer Science (including subseries Lecture Notes in Artificial Intelligence and Lecture Notes in Bioinformatics)*, vol. 7251 LNCS, pp. 116–123, Springer, Berlin, Heidelberg, 2012.

[145] Z. I. Attia, C. V. DeSimone, J. J. Dillon, Y. Sapir, V. K. Somers, J. L. Dugan, C. J. Bruce, M. J. Ackerman, S. J. Asirvatham, B. L. Striemer, J. Bukartyk, C. G. Scott, K. E. Bennet, D. J. Ladewig, E. J. Gilles, D. Sadot, A. B. Geva, and P. A. Friedman, "Novel bloodless potassium determination using a signal-processed single-lead ECG," *Journal of the American Heart Association*, vol. 5, jan 2016.

[146] O. Z. Yasin, Z. Attia, J. J. Dillon, C. V. DeSimone, Y. Sapir, J. Dugan, V. K. Somers, M. J. Ackerman, S. J. Asirvatham, C. G. Scott, K. E. Bennet, D. J. Ladewig, D. Sadot, A. B. Geva, and P. A. Friedman, "Noninvasive blood potassium measurement using signal-processed, single-lead ecg acquired from a handheld smartphone," *Journal of Electrocardiology*, vol. 50, pp. 620–625, sep 2017.

[147] M. L. Krogager, K. Kragholm, R. K. Skals, R. N. Mortensen, C. Polcwiartek, C. Graff, J. B. Nielsen, J. K. Kanters, A. G. Holst, P. Søgaard, A. Pietersen, C. Torp-Pedersen, and S. M. Hansen, "The relationship between serum potassium concentrations and electrocardiographic characteristics in 163,547 individuals from primary care," *Journal of Electrocardiology*, vol. 57, pp. 104–111, nov 2019.

[148] M. Andersen, J. Xue, C. Graff, T. Hardahl, E. Toft, J. Kanters, M. Christiansen, H. Jensen, and J. Struijk, "A robust method for quantification of ikr-related t-wave morphology abnormalities," in *2007 Computers in Cardiology*, pp. 341–344, 2007.

[149] L. Hong, L. J. Andersen, C. Graff, E. Vedel-Larsen, F. Wang, J. J. Struijk, P. Sogaard, P. R. Hansen, Y. Z. Yang, M. Christiansen, E. Toft, and J. K. Kanters, "T-wave morphology analysis of competitive athletes," *Journal of Electrocardiology*, vol. 48, pp. 35–42, jan 2015.

[150] S. G. Tischer, C. Graff, C. Ellervik, E. Prescott, J. K. Kanters, and H. K. Rasmusen, "Influence of type of sport on cardiac repolarization assessed by electrocardiographic T-wave morphology combination score," *Journal of Electrocardiology*, vol. 51, pp. 296–302, mar 2018.

[151] C. Graff, J. Matz, E. B. Christensen, M. P. Andersen, J. K. Kanters, E. Toft, S. Pehrson, T. B. Hardahl, J. Nielsen, and J. J. Struijk, "Quantitative Analysis of T-wave Morphology Increases Confidence in Drug-Induced Cardiac Repolarization Abnormalities: Evidence From the Investigational IKr Inhibitor Lu 35-138," *The Journal of Clinical Pharmacology*, vol. 49, pp. 1331–1342, nov 2009.

[152] A. Rodrigues, A. Petrėnas, V. Marozas, N. Kušleikaite-Pere, and P. Laguna, "Ecg-based monitoring of electrolyte fluctuations during the long interdialytic interval," in *2018 Computing in Cardiology Conference (CinC)*, vol. 45, pp. 1–4, 2018.

[153] A. Rodrigues, A. Petrėnas, B. Paliakaitė, N. Kušleikaitė-Pere, G. Jaruševičius, I. A. Bumblytė, P. Laguna, and V. Marozas, "Noninvasive monitoring of potassium fluctuations during the long interdialytic interval," *IEEE Access*, vol. 8, pp. 188488–188502, 2020.

[154] H. A. Bukhari, F. Palmieri, J. Ramírez, P. Laguna, J. E. Ruiz, D. Ferreira, M. Potse, C. Sanchez, and E. Pueyo, "Characterization of T Wave Amplitude, Duration and Morphology Changes During Hemodialysis: Relationship with Serum Electrolyte Levels and Heart Rate," *IEEE Transactions on Biomedical Engineering*, vol. 68, no. 8, pp. 2467–6478, 2020.

[155] M. F. Wu, J. J. Chiang, Y. C. Yang, I. H. Chao, S. M. Shieh, W. C. Tzeng, and J. C. Hsieh, "Predicting hyperkalemia by a two-staged artificial neural network," *Computers in Cardiology*, vol. 30, pp. 433–435, 2003.

[156] W. Tzeng, Y. Chan, and J. Hsieh, "Predicting hyperkalemia by the use of a 12-lead temporal-spatial electrocardiograph: clinical evaluations and model simulations," in *Computers in Cardiology, 2005*, pp. 215–218, 2005.

[157] Y. LeCun, K. Kavukcuoglu, and C. Farabet, "Convolutional networks and applications in vision," in *Proceedings of 2010 IEEE International Symposium on Circuits and Systems*, pp. 253–256, 2010.

[158] L. A. Salazar-Licea, J. C. Pedraza-Ortega, A. Pastrana-Palma, and M. A. Aceves-Fernandez, "Location of mammograms ROI's and reduction of false-positive," *Computer Methods and Programs in Biomedicine*, vol. 143, pp. 97–111, may 2017.

[159] D. S. W. Ting, C. Y. L. Cheung, G. Lim, G. S. W. Tan, N. D. Quang, A. Gan, H. Hamzah, R. Garcia-Franco, I. Y. S. Yeo, S. Y. Lee, E. Y. M. Wong, C. Sabanayagam, M. Baskaran, F. Ibrahim, N. C. Tan, E. A. Finkelstein, E. L. Lamoureux, I. Y. Wong, N. M. Bressler, S. Sivaprasad, R. Varma, J. B. Jonas, M. G. He, C. Y. Cheng, G. C. M. Cheung, T. Aung, W. Hsu, M. L. Lee, and T. Y. Wong, "Development and validation of a deep learning system for diabetic retinopathy and related eye diseases using retinal images from multiethnic populations with diabetes," *JAMA - Journal of the American Medical Association*, vol. 318, pp. 2211–2223, dec 2017.

[160] C. D. Galloway, A. V. Valys, J. B. Shreibati, D. L. Treiman, F. L. Petterson, V. P. Gundotra, D. E. Albert, Z. I. Attia, R. E. Carter, S. J. Asirvatham, M. J. Ackerman, P. A. Noseworthy, J. J. Dillon, and P. A. Friedman, "Development and Validation of a Deep-Learning Model to Screen for Hyperkalemia from the Electrocardiogram," *JAMA Cardiology*, vol. 4, pp. 428–436, may 2019.

[161] C. S. Lin, C. Lin, W. H. Fang, C. J. Hsu, S. J. Chen, K. H. Huang, W. S. Lin, C. S. Tsai, C. C. Kuo, T. Chau, S. J. Yang, and S. H. Lin, "A deep-learning algorithm (ECG12Net) for detecting hypokalemia and hyperkalemia by electrocardiography: Algorithm development," *JMIR Medical Informatics*, vol. 8, p. e15931, mar 2020.

[162] A. Holzinger, "From machine learning to explainable AI," in *DISA 2018 - IEEE World Symposium on Digital Intelligence for Systems and Machines, Proceedings*, pp. 55–66, Institute of Electrical and Electronics Engineers Inc., oct 2018.

[163] V. Monasterio, G. D. Clifford, P. Laguna, and J. P. Martínez, "A multilead scheme based on periodic component analysis for T-Wave alternans analysis in the ECG," *Annals of Biomedical Engineering*, vol. 38, pp. 2532–2541, apr 2010.

[164] B. F. Palmer, "Regulation of potassium homeostasis," *Clin J Am Soc Nephrol*, vol. 10, pp. 1050–1060, 2015.

[165] M. S. Makar and P. H. Pun., "Sudden cardiac death among hemodialysis patients," *Am J Kidney Dis*, vol. 69, p. 684–695, 2017.

[166] J. Ramírez, M. Orini, J. D. Tucker, E. Pueyo, and P. Laguna, "Variability of Ventricular Repolarization Dispersion Quantified by Time-Warping the Morphology of the T-Waves," *IEEE Transactions on Biomedical Engineering*, vol. 64, pp. 1619–1630, jul 2017.

[167] F. Palmieri, P. Gomis, D. Ferreira, J. E. Ruiz, B. Bergasa, A. Martín-Yebra, H. A. Bukhari, E. Pueyo, J. P. Martínez, J. Ramírez, and P. Laguna, "Monitoring blood potassium concentration in hemodialysis patients by quantifying T-wave morphology dynamics," *Scientific Reports*, vol. 11, no. 1, p. 3883, 2021.

[168] L. Sörnmo and P. Laguna, "Electrocardiogram (ECG) Signal Processing," in *Wiley Encyclopedia of Biomedical Engineering*, Hoboken, NJ, USA: John Wiley & Sons, Inc., apr 2006.

[169] J. P. Martínez, R. Almeida, S. Olmos, A. P. Rocha, and P. Laguna, "A Wavelet-Based ECG Delineator Evaluation on Standard Databases," *IEEE Transactions on Biomedical Engineering*, vol. 51, pp. 570–581, apr 2004.

[170] D. Yoon, H. S. Lim, J. C. Jeong, T. Y. Kim, J. G. Choi, J. H. Jang, E. Jeong, and C. M. Park, "Quantitative evaluation of the relationship between t-wave-based features and serum potassium level in real-world clinical practice," *BioMed Research International*, vol. 2018, 2018.

[171] P. Laguna, R. Jané, and P. Caminal, "Automatic detection of wave boundaries in multilead ECG signals: Validation with the CSE database," *Computers and Biomedical Research*, vol. 27, no. 1, pp. 45–60, 1994.

[172] F. Castells, P. Laguna, L. Sörnmo, A. Bollmann, and J. M. Roig, "Principal Component Analysis in ECG Signal Processing," *EURASIP Journal on Advances in Signal Processing*, vol. 2007, p. 074580, dec 2007.

[173] R. Sassi and L. T. Mainardi, "An estimate of the dispersion of repolarization times based on a biophysical model of the ECG," *IEEE Transactions on Biomedical Engineering*, vol. 58, pp. 3396–3405, dec 2011.

[174] C. S. Kuo, K. Munakata, C. P. Reddy, and B. Surawicz, "Characteristics and possible mechanism of ventricular arrhythmia dependent on the dispersion of action potential durations," *Circulation*, vol. 67, no. 6 I, pp. 1356–1367, 1983.

[175] J. A. Vassallo, D. M. Cassidy, K. E. Kindwall, F. E. Marchlinski, and M. E. Josephson, "Nonuniform recovery of excitability in the left ventricle," *Circulation*, vol. 78, no. 6, pp. 1365–1372, 1988.

[176] M. N. Niemeijer, M. E. Van Den Berg, M. Eijgelsheim, G. Van Herpen, B. H. Stricker, J. A. Kors, and P. R. Rijnbeek, "Short-term QT variability markers for the prediction of ventricular arrhythmias and sudden cardiac death: A systematic review," *Heart*, vol. 100, pp. 1831–1836, dec 2014.

[177] R. M. John, U. B. Tedrow, B. A. Koplan, C. M. Albert, L. M. Epstein, M. O. Sweeney, A. L. Miller, G. F. Michaud, and W. G. Stevenson, "Ventricular arrhythmias and sudden cardiac death," *The Lancet*, vol. 380, pp. 1520–1529, oct 2012.

[178] P. Laguna, J. P. Martínez, and E. Pueyo, "Techniques for Ventricular Repolarization Instability Assessment from the ECG," *Proceedings of the IEEE*, vol. 104, pp. 392–415, feb 2016.

[179] P. D. Arini, G. C. Bertrán, E. R. Valverde, and P. Laguna, "T-wave width as an index for quantification of ventricular repolarization dispersion: Evaluation in an isolated rabbit heart model," *Biomedical Signal Processing and Control*, vol. 3, pp. 67–77, jan 2008.

[180] M. Kesek, O. Gustavsson, and U. Wiklund, "Nondipolar content of t wave derived from a myocardial source simulation with increased repolarization inhomogeneity," *Annals of Noninvasive Electrocardiology*, vol. 14, pp. 185–192, apr 2009.

[181] M. J. Burgess, "Relation of ventricular repolarization to electrocardiographic T wave-form and arrhythmia vulnerability," *American Journal of Physiology - Heart and Circulatory Physiology*, vol. 5, no. 3, 1979.

[182] W. Shimizu and C. Antzelevitch, "Cellular basis for long QT, transmural dispersion of repolarization, and torsade de pointes in the long QT syndrome," *Journal of Electrocardiology*, vol. 32, no. SUPPL., pp. 177–184, 1999.

[183] K. Gima and Y. Rudy, "Ionic current basis of electrocardiographic waveforms: A model study," *Circulation Research*, vol. 90, pp. 889–896, may 2002.

[184] C. P. Day, J. M. McComb, and R. W. Campbell, "QT dispersion: An indication of arrhythmia risk in patients with long QT intervals," *Heart*, vol. 63, no. 6, pp. 342–344, 1990.

[185] G. X. Yan and C. Antzelevitch, "Cellular basis for the normal T wave and the electrocardiographic manifestations of the long-QT syndrome," *Circulation*, vol. 98, pp. 1928–1936, nov 1998.

[186] A. Mincholé, E. Pueyo, J. F. Rodrguez, E. Zacur, M. Doblaré, and P. Laguna, "Quantification of restitution dispersion from the dynamic changes of the T-wave peak to end, measured at the surface ECG," *IEEE Transactions on Biomedical Engineering*, vol. 58, pp. 1172–1182, may 2011.

[187] J. O. Ramsay and X. Li, "Curve registration," *Journal of the Royal Statistical Society: Series B (Statistical Methodology)*, vol. 60, pp. 351–363, jan 1998.

[188] A. Srivastava, W. Wu, S. Kurtek, E. Klassen, and J. S. Marron, "Registration of Functional Data Using Fisher-Rao Metric," *arXiv preprint*, mar 2011.

[189] J. D. Tucker, W. Wu, and A. Srivastava, "Generative models for functional data using phase and amplitude separation," *Computational Statistics and Data Analysis*, vol. 61, pp. 50–66, may 2013.

[190] D. P. Bertsekas, *Dynamic programming and optimal control*. Belmont, MA, 1995.

[191] R. E. Welsch, "Robust regression using iteratively reweighted least-squares," *Communications in Statistics - Theory and Methods*, vol. 6, pp. 813–827, jan 1977.

[192] D. di Bernardo and A. Murray, "T wave shape changes with heart rate: a computer model analysis," *2000 Computing in Cardiology*, vol. 27 (Cat. 00CH37163), pp. 151–154, 2000.

[193] K. Hnatkova and M. Malik, ""Optimum" formulae for heart rate correction of the QT interval," *Pacing Clin. Electrophysiol.*, vol. 22, p. 1683–1687, 1999.

[194] E. Pueyo, P. Smetana, P. Caminal, A. B. De Luna, M. Malik, and P. Laguna, "Characterization of QT interval adaptation to RR interval changes and its use as a a risk-stratifier of arrhythmic mortality in amiodarone-treated survivors of acute myocardial infarction," *IEEE Transactions on Biomedical Engineering*, vol. 51, pp. 1511–1520, sep 2004.

[195] S. Luo, K. Michler, P. Johnston, and P. W. MacFarlane, "A comparison of commonly used QT correction formulae: The effect of heart rate on the QTc of normal ECGs," *Journal of Electrocardiology*, vol. 37, pp. 81–90, oct 2004.

[196] B. Vandenberk, E. Vandael, T. Robyns, J. Vandenberghe, C. Garweg, V. Foulon, J. Ector, and R. Willems, "Which QT correction formulae to use for QT monitoring?," *Journal of the American Heart Association*, vol. 5, jun 2016.

[197] J. R. Montford and S. Linas, "How dangerous is hyperkalemia?," *JASN*, vol. 28, pp. 3155–3165, 2017.

[198] S. Severi, S. Vecchietti, S. Cavalcanti, E. Mancini, and A. Santoro, "Electrocardiographic changes during hemodiafiltration with different potassium removal rates," *Blood Purification*, vol. 21, no. 6, pp. 381–388, 2003.

[199] A. Blumberg, H. W. Roser, C. Zehnder, and J. Müller-Brand, "Plasma potassium in patients with terminal renal failure during and after haemodialysis; relationship with dialytic potassium removal and total body potassium," *Nephrol Dial Transplant*, vol. 12, pp. 1629–1634, 1997.

[200] P. H. Pun and J. P. Middleton, "Dialysate potassium, dialysate magnesium, and hemodialysis risk," *J Am Soc Nephrol*, vol. 28, pp. 3441–3451, 2017.

[201] S. Severi and S. Cavalcanti, "Electrolyte and pH dependence of heart rate during hemodialysis: A computer model analysis," *Artificial Organs*, vol. 24, pp. 245–260, 2000.

[202] M. G. Crespo-Leiro, E. Barge-Caballero, J. Segovia-Cubero, J. González-Costello, S. López-Fernández, J. M. García-Pinilla, L. Almenar-Bonet, J. de Juan-Bagudá, E. Roig-Minguell, A. Bayés-Genís, M. Sanz-Julve, J. L. Lambert-Rodríguez, A. Lara-Padrón, J. M. Pérez-Ruiz, C. Fernández-Vivancos Marquina, L. de la Fuente-Galán, A. Varela-Román, F. Torres-Calvo, J. Andrés-Novales, A. Escudero-González, D. A. Pascual-Figal, F. Ridocci-Soriano, A. Sahuquillo-Martínez, D. Bierge-Valero, F. Epelde-Gonzalo, J. C. Gallego-Page, R. Dalmau González-Gallarza, R. Bover-Freire, J. Quiles-Granado, A. P. Maggioni, L. H. Lund, J. Muñiz, and J. Delgado-Jiménez, "Hyperkalemia in heart failure patients in Spain and its impact on guidelines and recommendations: ESC-EORP-HFA Heart Failure Long-Term Registry," *Revista Española de Cardiología (English Edition)*, vol. 73, pp. 313–323, apr 2020.

[203] A. S. Narula, V. Jha, H. K. Bali, V. Sakhuja, and R. P. Sapru, "Cardiac arrhythmias and silent myocardial ischemia during hemodialysis," *Renal Failure*, vol. 22, no. 3, pp. 355–368, 2000.

[204] J. E. Flythe, S. E. Kimmel, and S. M. Brunelli, "Rapid fluid removal during dialysis is associated with cardiovascular morbidity and mortality," *Kidney International*, vol. 79, no. 2, pp. 250–257, 2011.

[205] J. García, M. Åström, J. Mendive, P. Laguna, and L. Sörnmo, "ECG-based detection of body position changes in ischemia monitoring," *IEEE Transactions on Biomedical Engineering*, vol. 50, pp. 677–685, jun 2003.

[206] G. D. Clifford, F. Azuaje, and P. McSharry, *Advanced Methods and Tools for ECG Data Analysis.* Norwood, MA:Artech House, Inc., 2006.

[207] L. K. Saul and J. B. Allen, "Periodic component analysis: an eigenvalue method for representing periodic structure in speech.," *NIPS*, pp. 807—-813, 2010.

[208] R. Sameni, C. Jutten, and M. B. Shamsollahi, "Multichannel electrocardiogram decomposition using periodic component analysis," *IEEE Transactions on Biomedical Engineering*, vol. 55, pp. 1935–1940, aug 2008.

[209] M. G. Adams and B. J. Drew, "Body position effects on the ECG: Implication for ischemia monitoring," *Journal of Electrocardiology*, vol. 30, pp. 285–291, oct 1997.

[210] U. Satija, B. Ramkumar, and M. Sabarimalai Manikandan, "A Review of Signal Processing Techniques for Electrocardiogram Signal Quality Assessment," *IEEE Reviews in Biomedical Engineering*, vol. 11, pp. 36–52, feb 2018.

[211] M. Åström, J. García, P. Laguna, O. Pahlm, and L. Sörnmo, "Detection of body position changes using the surface electrocardiogram," *Medical and Biological Engineering and Computing*, vol. 41, pp. 164–171, mar 2003.

[212] F. Palmieri, P. Gomis, J. E. Ruiz, D. Ferreira, A. Martín-Yebra, E. Pueyo, J. P. Martínez, J. Ramírez, and P. Laguna, "ECG-based monitoring of blood potassium concentration: Periodic versus principal component as lead transformation for biomarker robustness," *Biomedical Signal Processing and Control*, vol. 68, p. 102719, jul 2021.

[213] G. B. Moody, W. Muldrow, and R. G. Mark, "A noise stress test for arrhythmia detectors.," *Computers in Cardiology 1984*, vol. 11, pp. 381–384, 1984.

[214] I. Silva and G. B. Moody, "An Open-source Toolbox for Analysing and Processing PhysioNet Databases in MATLAB and Octave," *Journal of Open Research Software*, vol. 2, sep 2014.

[215] G. H. Golub and C. F. Van Loan, *Matrix Computations*. The Johns Hopkins University Press, 1989.

[216] F. Palmieri, P. Gomis, J. E. Ruiz, D. Ferreira, A. Martín-Yebra, E. Pueyo, P. Laguna, J. P. Martínez, and J. Ramírez, "Potassium Monitoring from Multilead T-wave Morphology Changes during Hemodyalisis: Periodic Versus Principal Component Analysis," in *Computing in Cardiology*, vol. 2020-September, IEEE Computer Society, sep 2020.

[217] V. Monasterio, P. Laguna, and J. P. Martínez, "Multilead analysis of T-wave alternans in the ecg using principal component analysis," *IEEE Transactions on Biomedical Engineering*, vol. 56, pp. 1880–1890, jul 2009.

[218] S. T. Schmidt, T. Ditting, B. Deutsch, R. Schutte, S. Friedrich, I. Kistner, C. Ott, U. Raff, R. Veelken, and R. E. Schmieder, "Circadian rhythm and day to day variability of serum potassium concentration: A pilot study," *J. Nephrol.*, vol. 28, p. 165–172, 2015.

[219] N. M. Selby and C. W. McIntyre, "The Acute Cardiac Effects of Dialysis," *Seminars in Dialysis*, vol. 20, pp. 220–228, jun 2007.

[220] C. W. McIntyre, J. O. Burton, N. M. Selby, L. Leccisotti, S. Korsheed, C. S. Baker, and P. G. Camici, "Hemodialysis-induced cardiac dysfunction is associated with an acute reduction in global and segmental myocardial blood flow," *Clinical Journal of the American Society of Nephrology*, vol. 3, pp. 19–26, jan 2008.

[221] F. Palmieri, P. Gomis, J. E. Ruiz, D. Ferreira, A. Martín-Yebra, E. Pueyo, J. P. Martínez, J. Ramírez, and P. Laguna, "Nonlinear T-Wave Time Warping-Based Sensing Model for Non-Invasive Personalised Blood Potassium Monitoring in Hemodialysis Patients: A Pilot Study," *Sensors*, vol. 21, p. 2710, apr 2021.

[222] J. Ramírez, M. Orini, A. Mincholé, V. Monasterio, I. Cygankiewicz, A. B. de Luna, J. P. Martínez, E. Pueyo, and P. Laguna, "T-wave morphology restitution predicts sudden cardiac death in patients with chronic heart failure," *Journal of the American Heart Association*, vol. 6, may 2017.

[223] R. Vazquez, A. Bayes-Genis, I. Cygankiewicz, D. Pascual-Figal, L. Grigorian-Shamagian, R. Pavon, J. R. Gonzalez-Juanatey, J. M. Cubero, L. Pastor, J. Ordonez-Llanos, J. Cinca, and A. B. de Luna, "The MUSIC Risk score: a simple method for predicting mortality in ambulatory patients with chronic heart failure," *European heart journal*, vol. 30, pp. 1088–1096, may 2009.

[224] J. Ramírez, S. van Duijvenboden, N. Aung, P. Laguna, E. Pueyo, A. Tinker, P. D. Lambiase, M. Orini, and P. B. Munroe, "Cardiovascular Predictive Value and Genetic Basis of Ventricular Repolarization Dynamics," *Circulation: Arrhythmia and Electrophysiology*, vol. 12, oct 2019.

[225] J. Ramírez, M. Orini, A. Mincholé, V. Monasterio, I. Cygankiewicz, A. Bayés De Luna, P. J. Martínez, P. Laguna, and E. Pueyo, "Sudden cardiac death and pump failure death prediction in chronic heart failure by combining ECG and clinical markers in an integrated risk model," *PLOS ONE*, vol. 12, no. 10, pp. 1–15, 2017.

[226] L. Xie, Z. Li, Y. Zhou, Y. He, and J. Zhu, "Computational Diagnostic Techniques for Electrocardiogram Signal Analysis," *Sensors (Basel, Switzerland)*, vol. 20, pp. 1–32, nov 2020.

[227] J. P. Madeiro, W. B. Nicolson, P. C. Cortez, J. A. Marques, C. R. Vázquez-Seisdedos, N. Elangovan, G. A. Ng, and F. S. Schlindwein, "New approach for T-wave peak detection and T-wave end location in 12-lead paced ECG signals based on a mathematical model," *Medical engineering & physics*, vol. 35, pp. 1105–1115, aug 2013.

[228] "Recommendations for measurement standards in quantitative electrocardiography," *European Heart Journal*, vol. 6, no. 10, p. 815–25, 1985.

[229] A. Van Oosterom, "Genesis of the T wave as based on an equivalent surface source model," *Journal of Electrocardiology*, vol. 34, no. 4, pp. 217–227, 2001.

[230] N. J. Perkins and E. F. Schisterman, "The Inconsistency of "Optimal" Cut-points Using Two ROC Based Criteria.," *American journal of epidemiology*, vol. 163, p. 670, apr 2006.

[231] J. M. Bland and D. G. Altman, "Statistics Notes: Survival probabilities (the Kaplan-Meier method)," *BMJ : British Medical Journal*, vol. 317, no. 7172, p. 1572, 1998.

[232] J. T. Rich, J. G. Neely, R. C. Paniello, C. C. J. Voelker, B. Nussenbaum, and E. W. Wang, "A practical guide to understanding Kaplan-Meier curves," *Otolaryngology–head and neck surgery : official journal of American Academy of Otolaryngology-Head and Neck Surgery*, vol. 143, no. 3, p. 331, 2010.

[233] E. Marubini and M. G. Valsecchi, *Analysing survival data from clinical trials and observational studies*. Chichester (UK): J. Wiley and Sons, 2004.

[234] D. Y. Lin, L. Dai, G. Cheng, and M. O. Sailer, "On Confidence Intervals for the Hazard Ratio in Randomized Clinical Trials," *Biometrics*, vol. 72, p. 1098, dec 2016.

[235] A. Lanari, L. O. Chait, and C. Capurro, "Electrocardiographic effects of potassium. I. Perfusion through the coronary bed," *American heart journal*, vol. 67, no. 3, pp. 357–363, 1964.

[236] M. M. Laks and S. R. Elek, "The effect of potassium on the electrocardiogram: clinical and transmembrane correlations," *Diseases of the chest*, vol. 51, no. 6, pp. 573–586, 1967.

[237] R. H. Clayton, O. Bernus, E. M. Cherry, H. Dierckx, F. H. Fenton, L. Mirabella, A. V. Panfilov, F. B. Sachse, G. Seemann, and H. Zhang, "Models of cardiac tissue electrophysiology: Progress, challenges and open questions," *Progress in Biophysics and Molecular Biology*, vol. 104, no. 1-3, pp. 22–48, 2011.

[238] B. N. Roberts, P. C. Yang, S. B. Behrens, J. D. Moreno, and C. E. Clancy, "Computational approaches to understand cardiac electrophysiology and arrhythmias," *American Journal of Physiology - Heart and Circulatory Physiology*, vol. 303, no. 7, p. H766–H783, 2012.

[239] S. A. Niederer, J. Lumens, and N. A. Trayanova, "Computational models in cardiology," *Nature Reviews Cardiology*, vol. 16, no. 2, pp. 100 – 111, 2019.

[240] M. L. Gumz, L. Rabinowitz, and C. S. Wingo, "An integrated view of potassium homeostasis," *N Engl J Med*, vol. 1, pp. 60–72, jul 2015.

[241] G. Liamis, E. Liberopoulos, F. Barkas, and M. Elisaf, "Diabetes mellitus and electrolyte disorders ," *World J Clin Cases.*, vol. 2, pp. 488–496, oct 2014.

[242] A. Goyal, J. A. Spertus, K. Gosch, L. Venkitachalam, P. G. Jones, G. V. D. Berghe, and M. Kosiborod, "Serum potassium levels and mortality in acute myocardial infarction," *JAMA - Journal of the American Medical Association*, vol. 307, pp. 157–164, 2012.

[243] M. R. Jacobsen, R. Reza Jabbari, C. Glinge, N. K. Stampe, J. H. Butt, P. Blanche, J. Lønborg, O. W. Nielsen, L. Køber, C. Torp-Pedersen, F. Pedersen, J. Tfelt-Hansen, and T. Engstrøm, "Potassium Disturbances and Risk of Ventricular Fibrillation Among Patients With ST-Segment–Elevation Myocardial Infarction," *Journal of the American Heart Association*, vol. 9, p. e014160, dec 2019.

Scientific contributions and awards

List of publications

Peer-reviewed journal publications

- **F. Palmieri**, P. Gomis, D. Ferreira, E. Pueyo, J. P. Martínez, P. Laguna, and J. Ramírez. "Weighted Time Warping Improves T-wave Morphology Markers Clinical Significance". *IEEE Transactions on Biomedical Engineering*, doi: 10.1109/TBME.2022.3153791, 2022.

- **F. Palmieri**, P. Gomis, J. E. Ruiz, D. Ferreira, A. Martín-Yebra, E. Pueyo, J. P. Martínez, J. Ramírez and P. Laguna. "Nonlinear T-Wave Time Warping-Based Sensing Model for Non-Invasive Personalised Blood Potassium Monitoring in Hemodialysis Patients: A Pilot Study" *Sensors*, vol. 21, no. 8, Art. no. 2710, 2021, doi: 10.3390/s21082710.

- **F. Palmieri**, P. Gomis, J. E. Ruiz, D. Ferreira, A. Martín-Yebra, E. Pueyo, J. P. Martínez, J. Ramírez and P. Laguna. "ECG-based monitoring of blood potassium concentration: Periodic versus principal component as lead transformation for biomarker robustness" *Biomedical Signal Processing and Control*, vol. 68, Art. no. 102719, 2021, doi: 10.1016/j.bspc.2021.102719.

- **F. Palmieri**, P. Gomis, J. E. Ruiz, B. Bergasa, D. Ferreira, A. Martín-Yebra, H. A. Bukhari, J. P. Martínez, E. Pueyo, J. Ramírez and P. Laguna. "Monitoring Blood Potassium Concentration in Hemodyalisis Patients by T-wave Morphology Dynamics Quantification" *Scientific Reports*, 2021; vol. 11, Art. no. 3883, doi: 10.1038/s41598-021-82935-5.

- H. A. Bukhari, **F. Palmieri**, J. Ramírez, P. Laguna, J. E. Ruiz, D. Ferreira, M. Potse, C. Sánchez, and E. Pueyo. "Characterization of T Wave Amplitude, Duration and Morphology Changes During Hemodialysis: Relationship With Serum Electrolyte Levels and Heart Rate" *IEEE Transactions on Biomedical Engineering*, vol. 68, no. 8, pp. 2467-2478, 2021, doi: 10.1109/TBME.2020.3043844.

- H. A. Bukhari, C. Sánchez, S. Srinivasan, **F. Palmieri**, M. Potse, P. Laguna, and E. Pueyo. "Estimation of Potassium Levels in Hemodialysis Patients by T wave Nonlinear Dynamics and Morphology Markers" *Computers in Biology and Medicine*, vol. 143, Art. no. 105304, 2022, doi: /10.1016/j.compbiomed.2022.105304.

Peer-reviewed international conference publications

- **F. Palmieri**, P. Gomis, J. E. Ruiz, D. Ferreira, E. Pueyo, J. P. Martínez, P. Laguna, and J. Ramírez. "Weighted Time Warping T-wave Analysis Robust to Delineation Errors: Clinical Implications". *2021 Computing in Cardiology (CinC)*, Brno, Czech Republic vol. 48, pp. 1-4, 2021, doi: 10.23919/CinC53138.2021.9662738.

- **F. Palmieri**, P. Gomis, J. E. Ruiz, D. Ferreira, A. Martín-Yebra, E. Pueyo, P. Laguna, J. P. Martínez and J. Ramírez. "Potassium Monitoring From Multilead T-wave Morphology Changes During Hemodyalisis: Periodic Versus Principal Component Analysis." *2020 Computing in Cardiology*, Rimini, Italy, 2020, pp. 1-4, 2020, doi: 10.22489/CinC.2020.199.

- **F. Palmieri**, P. Gomis, D. Ferreira, J. E. Ruiz, B. Bergasa, A. Martín-Yebra, H. A. Bukhari, E. Pueyo, J. P. Martínez, J. Ramírez and P. Laguna. "T-Wave Morphology Changes as Surrogate for Blood Potassium Concentration in Hemodialysis Patients." *2019 Computing in Cardiology (CinC)*, Singapore, 2019, pp. 1-4, doi: 10.23919/CinC49843.2019.9005904.
- H. A. Bukhari, **F. Palmieri**, D. Ferreira, M. Potse, J. Ramírez, P. Laguna, C. Sánchez, and E. Pueyo. "Transmural Ventricular Heterogeneities Play a Major Role in Determining T-Wave Morphology at Different Extracellular Potassium Levels" *2019 Computing in Cardiology (CinC)*, Singapore, 2019, pp. 1-4, doi: 10.23919/CinC49843.2019.9005944.

Peer-reviewed national (Spanish) conference publications

- **F. Palmieri**, P. Gomis, J. E. Ruiz, D. Ferreira, E. Pueyo, J. P. Martínez, P. Laguna, and J. Ramírez. " "Time-Warping" ponderado sobre la onda T para Reducir el Impacto de Errores de Delineación: Implicaciones Clínicas". *Actas del XXXIX Congreso Anual de la Sociedad Española de Ingeniería Biomédica*, Spain, 2021, pp.94-98 ISBN 978-84-09-36054-3.
- **F. Palmieri**, P. Gomis, J. E. Ruiz, D. Ferreira, A. Martín-Yebra, E. Pueyo, P. Laguna, J. P. Martínez and J. Ramírez. "Monitorización en diálisis de la concentración de potasio en sangre mediante los cambios en la morfología multi-lead de la onda T: comparación entre usar la transformación en componentes periódicas y principales". *Actas del XXXVIII Congreso Anual de la Sociedad Española de Ingeniería Biomédica*, Valladolid, Spain, 2020, pp. 434-437, ISBN 978-84-09-25491-0.
- **F. Palmieri**, P. Gomis, D. Ferreira, J. E. Ruiz, B. Bergasa, A. Martín-Yebra, H. A. Bukhari, E. Pueyo, J. P. Martínez, J. Ramírez and P. Laguna. "Estudio de los Cambios en la Morfología de las Ondas T como Sustituto de la Concentración de Potasio en Sangre en Pacientes de Hemodiálisis". *Actas del XXXVII Congreso Anual de la Sociedad Española de Ingeniería Biomédica*, Santander, Spain, 2019, pp. 291-294, ISBN 978-84-09-16707-4.

Supervision of master theses related to this thesis

- J. A. Quiroga Forero, "Evaluación de biomarcadores derivados del electrocardiograma de pacientes sometidos a hemodiálisis relacionados con cambios de potasio en sangre ", Date of defense: 26/10/2020 (second call), Universidad Internacional de Valencia.

Supervision of master theses not related to this thesis

- H. J. Vela González, "Evaluation of Cardiac Arrhythmia and Equipment", Date of defense: 09/12/2021 (second call), Universidad Internacional de Valencia.

Awards and fellowships

- *ERASMUS+ 2020 fellowship for Ph.D. students* - Winner.
- *Rosanna Degani Young Investigator Award for the best written and oral presentation* "T-Wave Morphology Changes as Surrogate for Blood Potassium Concentration in Hemodialysis Patients." *2019 Computing in Cardiology (CinC)*, Singapore, 2019 - Semifinalist.
- *Mortara mobility fellowship* "T-Wave Morphology Changes as Surrogate for Blood Potassium Concentration in Hemodialysis Patients." *2019 Computing in Cardiology (CinC)*, Singapore, 2019 - Winner.
- *ESC-CinC Clinical Needs Translational Award* "T-Wave Morphology Changes as Surrogate for Blood Potassium Concentration in Hemodialysis Patients." *2019 Computing in Cardiology (CinC)*, Singapore, 2019 - Winner.
- *José Maria Ferrero Award for Ph.D. students* "Estudio de los Cambios en la Morfología de las Ondas T como Sustituto de la Concentración de Potasio en Sangre en Pacientes de Hemodiálisis". *Actas del XXXVII Congreso Anual de la Sociedad Española de Ingeniería Biomédica*, Santander, Spain, 2019 - Finalist.

Acknowledgements

Last but not least, I would like to end this thesis by dedicating these last lines and thoughts to all of those people whose help have made this thesis possible and to whom I would very pleasantly like to thank.

I would like to express my deepest appreciation to my directors Professor Pablo Laguna and Professor Pedro Gomis, who have relied on me for the development of this study and for their support and counselling during the course of this thesis. Your persistence and leadership led me through this fantastic adventure and looking at what I achieved, I am really proud of it. Pablo, your insightful suggestions and constructive advice as well as your continuous and tireless spirit of adventure in regard to research have been very motivational for me. Pedro, I am grateful for the opportunity to join this amazing project and for providing me with all the useful materials and tools to carry on my research.

I would also like to extend my deepest gratitude to Dr Julia Ramírez whose personal and scientific skills gave me the great opportunity to grow scientifically and personally. It has been a privilege to have you as my guide in the *Time Warping* world, an incredible journey that began in a hot summer in Zaragoza six years ago and (I hope) is still far from being over. This Ph.D. would not have been so positive without your fast answers, your endless patience, practical suggestions, unwavering guidance, fast answers and special care to each detail.

I must also thank all the people and institutions I have collaborated with at Laboratorios Rubió and Hospital Clínico Universitario Lozano Blesa, for all the useful data and information provided that helped me to improve the work performed in this thesis.

I also wish to thank all the members of the *Biomedical Signal Interpretation & Computational Simulation (BSICoS) Group*. Professor Juan Pablo Martínez and Professor Esther Pueyo, whose helpful advice has been a cornerstone for this thesis; talking with you is always a pleasure. I would like to thank also Dr Alba, Dr Spyridon, Dr David, Dr Javier, Hassaan, Jennifer, Chiara and Saúl. I have had very productive discussions in the professional part and shared great times in the lab, conferences and travels.

Special thanks to Professor Patricia B. Munroe for the abroad experience at the William Harvey Research Institute, Queen Mary University of London, which allowed me to broaden my horizons and discover new points of view. I also wish to thank the research staff, they always treated me as one of them. It was an exciting experience of personal growth that have deeply enriched me.

I would like to mention the HERMES high computational cluster at the Aragón Institute for Engineering Research (I3A). It has been a privilege for me to have HERMES available that allowed parallel computing reducing significantly the computational cost of the analysis performed in during this thesis.

To my friends in Italy and in Spain for the relaxing moments and leisure time that have been very important to keep my mind clear.

Un grazie speciale alla mia famiglia, per tutto il supporto e l'aiuto che mi ha dato e per essere stata presente soprattutto nei momenti difficili.

A Maria, il mio porto sicuro dove rifugiarmi quando il mare è in tempesta. Non ho parole per descrivere l'enorme pazienza e l'immensa comprensione con cui mi sei stato accanto in questi anni. Grazie per il tuo incondizionato amore e costante sostegno per realizzare questo progetto di vita.

I am humbled by the fact that I have been lucky to be involved in this wonderful project and I am grateful for all of you. I feel I have learnt a lot from this work and I will cherish it not only in my future academic career but in my whole life.

Flavio